# ADVANCING LASER-ACTIVATED PERFLUOROCARBON NANODROPLETS AS DIAGNSOTIC AND IMAGE-GUIDED THERAPEUTIC AGENTS

A Dissertation
Presented to
The Academic Faculty

by

Daniela Yvonne Santiesteban

In Partial Fulfillment
of the Requirements for the Degree
Doctor of Philosophy in the
Department of Biomedical Engineering

Georgia Institute of Technology
Emory University

May, 2018

Copyright © 2018 by Daniela Yvonne Santiesteban

# ADVANCING LASER-ACTIVATED PERFLUOROCARBON NANODROPLETS AS DIAGNSOTIC AND IMAGE-GUIDED THERAPEUTICS

Approved by:

Dr. Stanislav Emelianov, Advisor
Department of Biomedical Engineering and School of Electrical and Computer Engineering
*Georgia Institute of Technology and Emory University*

Dr. Andres Garcia
Department of Mechanical Engineering
*Georgia Institute of Technology*

Dr. Laura Suggs
Department of Biomedical Engineering
*University of Texas at Austin*

Dr. Susan Thomas
Department of Mechanical Engineering
*Georgia Institute of Technology*

Dr. Krishnendu Roy
Department of Biomedical Engineering
*Georgia Institute of Technology and Emory University*

Date Approved: 02/08/18

*To my family for their unconditional love and support*

# ACKNOWLEDGEMENTS

I would like to start off by thanking my family. First, my mother and father who have always supported my dreams and ambitions, and in the process have been excellent role models. My decision to pursue a career in engineering stemmed largely from their passion for the field. Without them I would not be the person I am today, and I am forever indebted to them. I would like to thank my brother who I could always count on to help on various matters, and who has always pushed me to be the best version of myself. I would also like to thank my extended family in Mexico who have always believed in me from afar.

I would like to acknowledge the tremendous support and opportunities my advisor, Dr. Stanislav Emelianov, gave me throughout my graduate school career. Upon entering graduate school, I never imagined I would end up in an imaging-oriented lab, but in retrospect I could not imagine a better lab to be a part of. The independence I've had in pursuing various research areas, combined with the guidance and support provided helped shape my graduate school experience and has given me the confidence to enter into the next phase in my career. I would also like to thank my co-advisor, Dr. Laura Suggs. Despite moving from UT Austin, I could always count on her to provide advice on any situations I was facing. I thoroughly enjoyed my time as part of her lab and appreciate her mentorship. I would like to thank my committee members, Dr. Krishnendu Roy, Dr. Andres Garcia and Dr. Susan Thomas. As a 4$^{th}$ year transfer student, you all were very accommodating and helpful during a crucial time in my PhD.

I would like to thank all the core and animal staff who helped during my graduate career. The staff in the PRL was always incredibly helpful and friendly. Andrew Shaw in the microscopy core was of great help as I navigated learning how capture the best images.

Next, I would like to thank all my lab members throughout the years, both in the Ultrasound Imaging and Therapeutics lab and the Biomaterials and Therapeutics. It was such a pleasure to come into work each day and to be surrounded by such smart and kind people. Going through the PhD process is challenging, but you all made it a bit easier and memorable, and I greatly appreciate that. I would especially like to thank lab mates that I closely collaborated with, which includes Kristina Hallam, Steve Yarmoska, Chelsea Kraynak, Alex Hannah, Laura Ricles, and Eunna Chung. Kristina, Steve and I were part of the most recent PFC club and working with them was a wonderful and enjoyable experience. In addition, I'd like to thank the many former lab members who provided a lot of guidance during the early stages of my PhD, this includes: Jason Cook, Robin Hartman, Seung Yun Nam, Ryan Stowers, Kevin Eckes, Doug Yeager, Viktoriya Rybalko, Carloyn Bayer, Yun-Sheng Chen, Soon Joon Yoon, Geoff Luke, Kim Homan, Tera Sherrard and Juili Kelvekar. And to my current lab members: Eleanor Barber, Jisha VS, Andrei Karpoiuk, Don VanderLaan, Kelsey Kubelick, In-Cheol Sun, Heechul Yoon, Tim Sowers, Andrew Zhang, Yiying Zhu, Ashley Alva, Jingfei Liu, Brandyn Orr, Alicia Allen, Kabir Dhada, Shane Allen. I'd like to especially thank Diego Dumani, who was not too bad of an office mate and friend, and who was always willing to lend a helping hand with both lab and other issues. Thanks also to my undergrads Brantley Henson and Daniel Profili who gave me a chance to mentor them and were willing to spend hours in the lab helping out. Many thanks to all these people and others that I might have forgotten for their helpful

comments, assistance with experimental design and overall support during our time working together.

I would like to thank the cities of Atlanta and Austin who selflessly gave me countless beautifully memories and the ability to meet many different people. I formed numerous friendships that will stay with me forever, and I will always cherish these cities as the start of where those relationships began and grew. I'm especially grateful to have met Jason Canaras during my PhD career, who has been an amazing source of love, support and fun times. Also thanks to the many old friends who came to visit and would give me a break from the hectic PhD lab life.

Lastly, but most importantly, I'd like to thank God who made all of this even possible. Thank you.

# TABLE OF CONTENTS

# LIST OF FIGURES

## Chapter 2:



## Chapter 3



## Chapter 4

## Chapter 5



## Appendix A

# LIST OF SYMBOLS AND ABBREVIATIONS

| | |
|---|---|
| AuNRs | Gold nanorods |
| ADV | Acoustic droplet vaporization |
| APC | Antigen presenting cell |
| BSA | Bovine serum albumin |
| CT | Computed tomography |
| CuS | Copper sulfide |
| CVD | Cardiovascular disease |
| hASC | Human adipose stem cell |
| HIF | Hypoxia inducible factor |
| IVIS | In Vivo Imaging System |
| MBs | Microbubbles |
| MRI | Magnetic resonance imaging |
| NIR | Near infrared |
| NPs | Nanoparticles |

| | |
|---|---|
| PA | Photoacoustic |
| PAD | Peripheral arterial disease |
| PET | Positron emission tomography |
| PFC | Perfluorocarbon |
| PFCnDs | Perfluorocarbon nanodroplets |
| PFCps | Perfluorocarbon particles |
| PFH | Perfluorohexane |
| PFP | Perfluoropentane |
| $ppO_2$ | Oxygen partial pressure |
| RES | Reticuloendothelial system |
| RPMs | Red pulp macrophages |
| SPECT | Single-photon emission computed tomography |
| TDLN | Tumor draining lymph node |
| US | Ultrasound |
| USPA | Ultrasound/photoacoustic |
| UV-Vis | Ultraviolet-visible |

# SUMMARY

To date, perfluorocarbon particles have been most commonly studied in conjunction with ultrasound imaging, and as liquid ventilators due to their ability to solubilize large amounts of gases. A subset of perfluorocarbon particles, perfluorocarbon nanodroplets (PFCnDs), are becoming increasingly investigated because their versatile characteristics make them attractive diagnostic and therapeutic agents. PFCnDs are the sub-micrometer, liquid version of microbubbles (MBs) which are commonly used as ultrasound contrast agents in clinic. PFCnDs are superior to MBs in terms of increased circulation lifetimes and the ability to extravasate hyperpermeable vasculature. Additionally, PFCnDs can be phase-changed into MBs through user-controlled energy input, thereby simultaneously possessing the advantages associated with their nanoparticle size and the associated contrast enhancement of MBs. Given these characteristics, the work presented herein concentrated on developing "next generation" PFCnDs exhibiting enhanced diagnostic and image-guided therapeutic characteristics.

Acoustic activation has been the most well studied of the mechanisms to phase-change PFCnDs. However, laser-initiated activation has several advantages compared to acoustically-triggered PFCnDs. Laser-triggered PFCnDs are safe, the activation event is well-controlled, and they are more comprehensive imaging agents since they act as multimodal contrast agents, supplementing ultrasound contrast with photoacoustic (PA) contrast.

In the first two aims, innovative image-processing and engineering techniques that improve laser-activated PFCnDs's diagnostic abilities in cancer applications are described.

In Chapter 3, I describe the development of laser-activated PFCnDs which exhibit increased imaging depth, photoabsorber stability and overall biocompatibility. In conjunction, I developed an image-processing algorithm capable of creating background-free images from the unique temporal contrast provided by PFCnDs (explained in detail in **Appendix A**). Chapter 4 describes a platform consisting of multicolored PFCnDs capable of selectively initiating ultrasound/photoacoustic contrast from unique PFCnD subpopulations. To highlight the platform's usefulness, different lymphatic transport mechanisms were studied in a murine tumor-draining lymph node model. In addition to elucidating different trafficking mechanisms, the multicolored PFCnDs helped uncover important *in vivo* PFCnD characteristics not identified by previous acoustic-or laser-activated PFCnDs research. Future work will include targeting multicolored PFCnDs to various cancer receptors for improved diagnosis.

The third aim studies the ability of laser-activated PFCnDs to improve stem cell angiogenic therapy. Stem cell angiogenic therapies have struggled to achieve their clinical potential due to high amounts of cell death shortly after implantation. Given that the implantation site is severely ischemic, I hypothesized that oxygen-loaded PFCnDs could help mitigate the harsh conditions of the oxygen-deprived tissue and result in increased cell survival for more efficacious therapies. Additionally, I sought to bring more control over oxygen levels by studying whether laser-activation of PFCnDs induced increased release of oxygen. Findings demonstrated that laser-activated PFCnDs can influence oxygen levels in image-guided and passive mechanisms, impacting cell viability and hypoxic pathway regulation. Future work will focus on studying PFCnD impact in *in vivo* models, and engineering PFCnDs that exhibit enhanced control over activated oxygen release.

The last chapter highlights the accomplished PFCnD advances, and describes future work that would further establish laser-activated PFCnDs as effective diagnostic and therapeutic agents.

# CHAPTER 1. INTRODUCTION

Two of the leading causes of death, cancer and ischemic cardiovascular disease (CVD), have continued to affect millions of Americans over the past several decades. Despite the large amount of labor and resources devoted to combating these diseases, diagnosis is difficult and treatments often ineffective. Nanoparticles (NPs) have been touted as the key to revolutionizing medical diagnoses and therapy, thereby improving patient outcomes. However, in clinic, NPs have struggled to fulfill their potential, particularly in the diagnostic area. The goal of the following work was to develop NPs that show clinical potential as diagnostic agents and as image-guided therapeutics.

Specifically, I sought to improve perfluorocarbon nanodroplet (PFCnD) technology so that they can become more clinically relevant diagnostic and image-guided therapeutic agents. PFCnDs are the sub-micrometer, liquid version of the ubiquitously used ultrasound contrast agent, perfluorocarbon microbubbles (MBs). Recently, PFCnDs have gained interest due to their ability to expand upon favorable MB characteristics of enhanced ultrasound contrast and therapeutic delivery. Compared to MBs, PFCnDs have longer circulation lifetimes and can access tissue spaces that larger MBs cannot. In addition, PFCnDs can be phase-changed into MBs, via an external trigger, allowing for enhanced image contrast, and on-demand therapeutic release.

Of the various PFCnD subtypes, laser-activated PFCnDs present unique advantages, such as a well-controlled phase-change behavior and multimodal (photoacoustic and ultrasound) imaging contrast. Thus, the following work focused on advancing laser-activated PFCnDs technology to determine their clinical utility. Specifically, the presented

work demonstrates PFCnD developments that allow for background-free imaging, increased image penetration depth, the ability to simultaneously provide multiple signals via one imaging modality (i.e. multiplexed imaging), and image-guided therapeutic release.

To accomplish these achievements, the following specific aims were established and met:

## 1.1 Aim 1: Engineer clinically relevant, translatable PFCnDs

Light-triggered PFCnDs rely on a photoabsorber to initiate the phase-change. Therefore, the chosen photoabsorber is of critical importance in regards to attaining clinical relevance and future translation. I investigated the use of copper sulfide (CuS) nanoparticles as photoabsorbers, and studied their ability to produce efficient laser-activated PFCnDs. The constructed CuS-PFCnDs were examined in tissue models and compared to traditionally used photoabsorber-PFCnD constructs. CuS-PFCnDs's ability to provide *in vivo* image contrast was studied in an inflammatory murine model. In conjunction, background-free image processing was developed that can be used with other laser-activated PFCnDs for enhanced image quality.

## 1.2 Aim 2: Design a multicolored PFCnDs platform for multiplexed ultrasound and photoacoustic imaging

Multiplexing, i.e. the ability to send multiple signals over a shared medium, is a valuable tool for increasing efficiency and breadth of relayed information. In relation to medical imaging, optical imaging modalities have most thoroughly exploited this phenomenon given the vast array of available probes, e.g. fluorophores. In recent years,

the capability of clinically relevant imaging modalities to multiplex has become increasingly studied in order to improve diagnosis efficacy, particularly for heterogeneous diseases, such as cancer. In this aim, I engineer a multiplexed imaging platform based on laser-activated PFCnDs and ultrasound/photoacoustic imaging. The system's multiplexed sensitivity is shown in tissue mimicking phantoms, and then used to study different PFCnD lymphatic trafficking mechanisms in a tumor draining lymph node murine model. Interesting *in vivo* characteristics are uncovered that help establish PFCnDs's role as future diagnostic and therapeutic agents.

## 1.3 Aim 3: Investigate PFCnDs in improving current ischemic cardiovascular therapies.

Current stem cell angiogenic treatments suffer from high amounts of implanted cell death, rendering them ineffective. The high amount of cell death, is partly attributed to the extreme hypoxia, i.e. low oxygen, of the implanted site. The ability of oxygenated, laser-activated PFCnDs to ameliorate hypoxia-related cell effects is shown. Additionally, I demonstrated that PFCnDs provide image-guided oxygen release in a localized manner, and cause biomaterial changes that can enhance *in vivo* vascularization.

The accomplished work is significant because it builds upon foundational laser-activated PFCnD research and elevates their clinical utility as diagnostics and image-guided therapeutics. Looking forward, as photoacoustic imaging becomes more commonplace in the clinic, the advancements established in the subsequently described thesis work will become increasingly utilized.

# CHAPTER 2. BACKGROUND

## 2.1 Perfluorocarbon nanodroplets (PFCnDs)

Perfluorocarbon particles (PFCps) have a long standing history in medical applications.[1-2] A subset of these particles, PFCnDs, have become increasingly studied as diagnostic and therapeutic agents because of the versatility associated with their controllable phase-change characteristic.[3-8] PFCnDs are the sub-micrometer, liquid version of the clinically used ultrasound contrast agent, PFC MBs. They are composed of a stabilizing shell and perfluorocarbon core. Compared to MBs, PFCnDs offer several advantages including increased circulation lifetimes and the ability to extravasate hyperpermeable vasculature for directly diagnosing and treating diseased tissue.[9] Furthermore, PFCnDs can be phase-changed into MBs, most commonly via acoustic or laser irradiation, thus retaining the ability to act as enhanced ultrasound contrast agents. In addition to their favorable diagnostic properties, PFCnDs can be loaded with therapeutic drugs or gases and deliver their cargo in an image-guided manner.

### *2.1.1 Acoustically-activated PFCnDs in relation to laser-activated PFCnDs*

Of the PFCnD subtypes, acoustically activated PFCnDs have been around the longest and as a result, are the most thoroughly studied. Almost two decades ago, *Apfel et al.* designed PFC droplets and demonstrated the particles could be converted into microbubbles with ultrasound irradiation, a technique called acoustic droplet vaporization (ADV).[10] Since then, parameters influencing ADV such as particle size, composition, and ultrasound parameters have been studied by various groups.[5-6, 11-13] ADV occurs when

PFCnDs are irradiated with ultrasound at a sufficient peak negative pressure to cause a phase-change of their perfluorocarbon liquid core.[13] Traditionally, this has been accomplished using perfluorocarbon cores with boiling points lower than physiological temperatures. As ADV can also occur with PFCnD of high boiling point cores, alternative mechanisms of vaporization, such as nucleation based ADV, have recently been suggested.[9]

Despite laser-activated PFCnDs only being developed in 2012,[4] their close relationship to acoustically activated PFCnDs has allowed for their rapid progression as diagnostic and therapeutic agents. The essential difference between acoustic- and laser-activated PFCnDs is that the latter require an encapsulated photoabsorber and laser irradiation to initiate the phase-change.[4] This discrepancy allows for certain advantages over acoustically activated PFCnDs, including a highly-controlled vaporization event, and the ability to supplement ultrasound enhancement with photoacoustic imaging. Given these benefits, the purpose of the following work is to expand upon laser-activated PFCnDs's desirable properties and increase their clinical utility as diagnostic and image-guided therapeutic agents.

In order to gain a thorough appreciation of laser-activated PFCnDs's multimodal imaging capabilities, it is important to understand the fundamentals of ultrasound and photoacoustic imaging, and their relation to laser-activated PFCnD image contrast.

### *2.1.2 Ultrasound imaging*

Ultrasound imaging is one of the most widely used imaging modalities. It is routinely used in a range of applications because of its low-cost, portability, and ability to

safely provide anatomical information at sub-millimeter spatial resolutions.[14-16] Ultrasound imaging works by using a transducer to irradiate a tissue with high-frequency ( > 20 kHz) sound waves. The tissue's inherent properties cause a portion of the sound waves to be reflected back to the transducer, which will collect the information, amplify the signal electronically, and create a gray-scale image. Reflections, waves that carry the same frequency as the original waves emitted by the transducer, occur when the sound waves pass from one tissue type to another with different acoustic impedances.

Acoustic impedance ($Z$) is defined as:

$$Z = \rho * c$$

where ρ is the density of the tissue and $c$ is the speed of sound within the tissue. The portion of the sound wave reflected back, versus the remaining portion that is either scattered or continues traveling through the interrogated tissue, is proportional to the difference in acoustic impedance between the two materials. Tissues with a larger acoustic impedance mismatch will reflect a larger percentage of the sound wave, appearing brighter on gray-scale images. For this reason, gas microbubbles are routinely used as ultrasound contrast agents because of the large impedance difference between endogenous tissue and the gas-filled microbubbles.[14] Additionally, gas microbubbles can exhibit oscillations in size that allow for nonlinear harmonic imaging, further facilitating differentiation from the frequency of sound waves produced by tissue-related reflections.[14]

#### 2.1.2.1 Laser-activated PFCnDs as ultrasound contrast agents

In their nanodroplet form, PFCnDs provide minimal ultrasound contrast as there is an insignificant acoustic mismatch between PFCnDs's liquid core and the surrounding tissue or bodily fluids. However, upon phase-change, PFCnDs expand five times their size into gaseous microbubbles, acting as enhanced ultrasound contrast agents.[4] Hence, PFCnDs can persist in nanodroplet form until they are externally triggered to provide ultrasound contrast. Dependent on the perfluorocarbon core, PFCnDs can exist as a stable or transient microbubble, thus affecting their ultrasound contrast (See *Section 2.2.1 Types of PFCnDs and their different image contrast* for a detailed explanation.).

### *2.1.3 Photoacoustic imaging*

Photoacoustic imaging is based off a phenomenon discovered by Alexander Graham Bell when he observed that a solid material exposed to pulsed light would produce a sound wave.[17] For decades this knowledge sat untouched, but with the advancement of laser technology the photoacoustic phenomena saw a revival in widespread applications.[18] In medical imaging, photoacoustic imaging proved useful in supplementing ultrasound anatomical information with functional and molecular data.[19]

Medical photoacoustic imaging involves interrogating a tissue of interest with tuned, nanosecond pulsed laser light. Photoabsorbers that absorb the irradiated light's specific wavelength will undergo a thermoelastic expansion that produces a pressure wave.[18, 20] A transducer detects the produced pressure waves, i.e. acoustic waves, and based on the time they are received, determines the source of wave production and constructs an image.[21]

The initial pressure wave ($p_o$) is described as:

$$p_o = \mu_o \cdot F \cdot \Gamma$$

where $\mu_o$ is the optical absorption coefficient of the photoabsorber, $F$ is the light fluence, and $\Gamma$ is the Grüneisen parameter, a variable accounting for volume expansion, specific heat, and the speed of sound.[22] The produced photoacoustic signal is a highly dependent on the material's absorption characteristics, and the light energy that reaches the material. For this reason, near-infrared (NIR)[23] or extended NIR spectral range [24], 600-1200 nm, light sources are typically used. The reduced scattering and endogenous absorption within this regime allows for increased penetration in what is referred to as the optical imaging window (Figure 1).

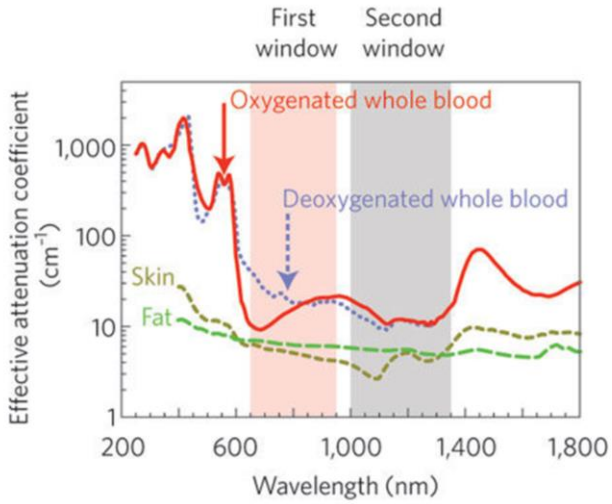


**Figure 1.** *In vivo* imaging within the optical windows allows for increased image penetration due to reduced endogenous absorption and scattering.[24]

#### 2.1.3.1 Endogenous and exogenous photoabsorbers

Photoabsorbers can be either endogenous or exogenous absorbers. Endogenous photoabsorbers are those that are found intrinsically in tissue and include deoxygenated and oxygenated hemoglobin, fat, and melanin.[25] As such, photoacoustic imaging can provide functionally relevant data without the introduction of contrast agents by tuning the irradiated light to the corresponding endogenous photoabsorber's absorption spectrum.[26-27] However, introduction of exogenous photoabsorbers allows for enhanced image contrast, increased penetration depth and ultimately more advanced diagnostic imaging.[28] Exogenous photoabsorbers most commonly include dyes or inorganic nanoparticles.[25, 28] The size and ease of functionalization of NPs facilitates molecularly specific imaging, greatly augmenting the *in vivo* diagnostic potential of photoacoustic imaging.[29-30] Additionally, NPs can be synthesized to absorb at distinct wavelengths to reduce effects of endogenous absorbers.[22]

Photoacoustic imaging's reliance on optical excitation grant it certain advantages, such as the ability to image various probes at once.[22, 31] Due to the broad absorption spectrum of most photoabsorbers, this is typically done by assessing acoustic responses to different wavelength excitations, and then applying spectral unmixing techniques to resolve the different photoabsorbers.[32] The advancement of photoabsorbers with narrow absorption spectra can allow for real-time imaging of multiple photoabsorbers, i.e. multiplexed photoacoustic imaging.[33] One limitation of relying on optical excitation is that photoacoustic imaging is limited to an imaging depth of 5 centimeters or less; however, this is still about a ten-fold increase compared to other optical based imaging modalities.[22]

#### 2.1.3.2 Laser-activated PFCnDs as photoacoustic contrast agents

Laser-activated PFCnDs consist of a perfluorocarbon core, surfactant shell and an encapsulated photoabsorber. Upon pulsed laser irradiation, tuned appropriately to the incorporated photoabsorber, the photoabsorber will absorb the light energy and undergo its typical thermoelastic expansion. The thermoelastic expansion from the many encapsulated photoabsorbers produces a slight increase in temperature, but more significantly, pressure aberrations which act as nucleation sites, causing the perfluorocarbon core to vaporize and transition into a microbubble. The vaporization event gives off an intense photoacoustic signal, several times greater than the photoacoustic signal provided by the encapsulated photoabsorber.[4, 34] Therefore, laser-activated PFCnDs exhibit both a vaporization-associated photoacoustic signal, and a photoabsorber-associated photoacoustic signal. Depending on the perfluorocarbon core utilized, the vaporization-associated photoacoustic signal can be a one-time or repeatable event (See *Section 2.2.1 Types of PFCnDs and their different image contrast* for detailed explanation).

### *2.1.4 USPA imaging*

Due to the natural synergy between ultrasound and photoacoustic imaging, researchers merged them and began exploiting their multimodal capabilities.[35-36] Ultrasound/photoacoustic (USPA) imaging combines ultrasound's anatomical information with photoacoustic imaging's functional information. Together, the two can provide comprehensive view of the interrogated tissue. Comparing USPA imaging to routinely used clinical imaging modalities, such as magnetic resonance imaging (MRI), computer tomography (CT), positron emission tomography (PET), and single-photon emission

computed tomography (SPECT), USPA imaging is safer (non-ionizing radiation), cost-effective and portable.[37-38] The biggest limitation of USPA imaging is its reduced imaging penetration compared to modalities that use ionizing radiation. However, USPA can penetrate deeper than any other optical-based modalities to date (Figure 2). With the continual advancement of contrast agents, USPA imaging can become a reliable presence in clinical settings.

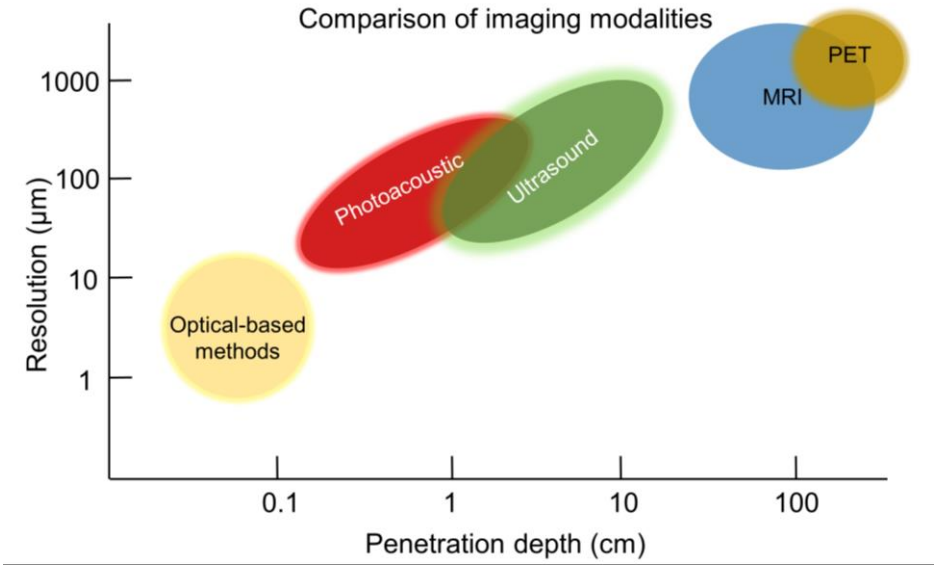


**Figure 2.** Penetration and resolution of various imaging modalities.

## 2.2 PFCnDs as diagnostic imaging agents

PFCnDs's close relationship to the widely used diagnostic agent, MBs, made for a natural transition into studying PFCnDs as diagnostic agents.[6, 39] Their small size, increased lifetimes, and ability to extravasate, expand their diagnostic potential relative to MBs.[8] PFCnDs can interact with extravascular lesions, and when functionalized, give molecularly relevant data. For cancer purposes, the ability to provide non-invasive, *in situ* information is greatly advantageous over current techniques. Biopsies, the clinical standard, are prone to sampling error, often misinforming physicians on the extent of disease heterogeneity.[40] Additionally, metastatic lesions, if present, are often of a different cellular makeup than primary tumors, making them difficult to detect and treat.[40] MRI and CT, combined with nuclear medicine (PET or SPEC), offer whole body imaging making them useful for diagnostic and staging purposes; however, these modalities are costly and use ionizing radiation, limiting their repetitive use.[41] As PFCnDs provide USPA contrast, using them for molecular imaging could help diagnose and frequently monitor therapy efficacy without burdens of safety or cost.

Most commonly, PFCnDs have been studied as diagnostic agents in cancer and cardiovascular disease applications.[5, 9, 42] To date, the majority of *in vivo* systemic injection studies have focused on cardiovascular applications,[43] likely a result of the challenges associated with getting sufficient PFCnD extravasation needed for solid tumor diagnosis.[44-45] Progress in smaller, targeted PFCnD will open more opportunities for extravascular applications. Already, PFCnDs have shown the ability to traffic to sentinel lymph nodes and provide image contrast when injected subcutaneously or intradermally, indicating their potential in metastatic applications.[46-47]

### *2.2.1 Types of PFCnDs and their different image contrast*

Depending on the perfluorocarbon core, PFCnDs will provide different types of USPA contrast. PFCnDs, even those synthesized with perfluorocarbons with boiling points lower than physiological temperatures, i.e. perfluoropentane (B.P. 27ºC), can persist as nanodroplets *in vivo*. This is explained by an increased Laplacian pressure ($\Delta P$), defined as:

$$\Delta P = P_{inside} - P_{outside} = \frac{2\sigma}{r}$$

and a function of surface tension ($\sigma$) and droplet radius ($r$). The elevated pressure inside the droplet effectively increases the boiling point, allowing low boiling PFCnDs to exist as metastable droplets. The differences in image contrast arise once PFCnDs are triggered with an energy input. Upon induced phase-change, low boiling PFCnDs will rapidly expand and become a stable microbubble.[39] PFCnDs synthesized with higher boiling point perfluorocarbons, i.e. perfluorohexane (B.P 57ºC), can also phase-change, but will only exist as a transient microbubble, rapidly recondensing back into the liquid state. This subset of PFCnDs "blink" and provide a sharp vaporization-associated photoacoustic and ultrasound signal each time a phase-change takes place, i.e. with each pulse of laser irradiation.[47-48] Choosing the type of PFCnD will depend on the intended purpose as well as the available imaging set-up. One-time PFCnDs will work with most imaging set-ups as they do not require high-frame rate capture, but they are less stable and overtime may spontaneously vaporize *in vivo*. Blinking PFCnDs have increased stability *in vivo*, but require high-frame rate USPA to capture the rapid phase-change and recondensation event.

## 2.3 **PFCnDs as image-guided therapeutic agents**

PFCnDs's favorable diagnostic characteristics make them equally desirable therapeutics. As such, PFCnDs have been investigated as therapeutic agents beginning in the 2000s.[49] The goal is that by allowing for localized release of therapeutics, via an external stimulus, PFCnDs can minimize the drug's undesirable side effects while increasing therapy efficacy.[50] Loading is often limited to PFCnD shell space as the perfluorocarbon core is both extremely hydrophobic and lipophobic.[1, 51] Loading of hydrophobic therapeutic agents is accomplished by loading within the hydrophobic portion of the shell, between the hydrophilic exterior and perfluorocarbon core.[52-53] Hydrophilic therapeutics can also be incorporated into PFC particles using double emulsion techniques, but result in micron size particles.[54-55] Interestingly, perfluorocarbons are extremely effective at solubilizing gases because of their weak van der Waals interactions, a characteristic imparted by PFC's C-F bond.[56] Depending on the PFC used, PFCnDs can solubilize oxygen at about 40-50% (v/v).[56] Hence, PFCs have been studied to deliver various therapeutics, including drugs, genes and gases.[3]

### *2.3.1 Therapeutic delivery*

#### 2.3.1.1 Drug-loaded PFCnDs

There are several mechanisms in which PFCnDs can deliver drugs to cellular targets. The most widely studied method involves conversion of PFCnDs into MBs, followed by inducing inertial or stable cavitation to increase cellular membrane permeability (reviewed in *Rapoport, 2012).*[8] This mechanism of therapeutic delivery uses extracellular PFCnDs. Alternatively, targeted and untargeted PFCnDs can be taken up by

cells and be phase-changed intracellularly.[57] However, there has not been much research regarding drug delivery using this method. Thus far, a study observing cell death after acoustically induced intracellular PFCnD phase-change, i.e. not drug-induced, is one of the few studies conducted observing cellular effects following PFCnD activation.[58] An additional manner of PFCnD drug delivery is through fusion of the lipid PFCnD shell with a cell bilayer.[59] This is typically done by incorporating a lipid disrupting membrane, e.g., melatinin, that causes PFCnD fusion into a cell's lipid bilayer, thereby bypassing endosomes and releasing cargo directly into the cytosol. [59-61]

#### 2.3.1.2 Gas-loaded PFCnDs

Compared to bulkier therapeutics, delivery of gases is more straightforward given their small size. PFCs can solubilize such large amounts of gases that they have been used as liquid ventilators.[56] Oxygen, the gas of interest for the following work, is loosely dissolved within PFCs. This is in contrast to how it is strongly bound to haemoglobin.[56] Thus, PFC-dissolved $O_2$ is readily released to tissues in need. This is beneficial in some cases, but poses challenges in controlling oxygen release, as the oxygen will rapidly diffuse out of PFCps based on the concentration gradient. However, certain measures can be taken to prevent excessive oxygen diffusion, such as altering the PFCnD shell.[62-63] Thus, PFCnDs can deliver gas passively, based on oxygen gradients, or actively, with the application of an external stimuli that will compromise shell permeability.[64-65]

## 2.4 **Research Goals**

The potential of laser-activated PFCnDs as diagnostics and therapeutics is evident; however, in order for them to successfully progress to their claimed clinical utility, more studies focused on clinically relevant advancements are needed. The goal of the following work was to bridge this gap and showcase laser-activated PFCnDs's clinical potential. To accomplish this, I developed PFCnD technology that allows for background-free imaging, increased image penetration depth, the ability to simultaneously provide multiple signals via one imaging modality (i.e. multiplexed imaging), and image-guided therapeutic release for enhancing treatments.

# CHAPTER 3. AIM 1: INCREASING CLINICAL RELEVANCE OF PERFLUOROCARBON NANODROPLETS AS DIAGNOSTIC AGENTS

## 3.1 Introduction

NPs can be readily classified into two groups: organic (*i.e.* liposomes, micelles, polymeric complexes, etc.) or inorganic (*i.e.* metallic, semiconductor, silica, etc.). Each group has its inherent strengths and weaknesses. Organic NPs are great therapeutic carriers, biodegradable and effectively cleared, but are typically incapable of providing image contrast on their own. Thus, they are poor diagnostic imaging agents. On the other hand, the majority of inorganic NPs are superior contrast agents, but struggle as efficacious therapeutics. Additionally, most inorganic NPs have limited biodegradability and clearance, which raises concerns over their clinical potential due to questionable long-term toxicity and bioeffects.[66] In the quest for ideal diagnostic and therapeutic NPs, researchers have turned to combinations of NPs.[67-68] Unfortunately, while combining NPs may augment the strengths of individual particles, they are often unable to overcome inherent barriers. For instance, combinations of particles may result in increased contrast, but at the expense of biocompatibility or limited clearance.

Laser-activated PFCnDs present a unique construct with which to synergistically combine organic (micelle) and inorganic components (copper sulfide (CuS) nanoparticles) and produce NPs with enhanced image contrast that retain high clinical translation potential. Thus, I developed CuS-PFCnDs that merge the increased photoacoustic and

ultrasound contrast enhancement of PFCnDs with the favorable biocharacteristics of CuS NPs.

Laser-activated PFCnDs have been synthesized with various photoabsorbers ranging from organic dyes to inorganic nanoparticles.[4, 69-72] The motivation for studying CuS NPs as the photoabsorber was based on considering characteristics of the ideal photoabsorber. The ideal photoabsorber would absorb at long wavelengths for increased penetration resulting in a higher signal-to-noise ratio, have good photothermal stability and efficiency, and be biodegradable with good clearance properties. Thus far, photoabsorbers used as PFCnD triggers have struggled to fulfill these requirements. For instance, gold nanorods (AuNRs) can be synthesized to absorb within desirable wavelength range, including 1064 nm; however, they are neither biodegradable nor effectively cleared, provoking concerns over long-term cytotoxicity and safety.[72] Also, upon pulsed laser irradiation, anisotropic gold nanoparticles are prone to melting and morphing shape, altering their spectrum and thus limiting long-term applications.[73] Finally, many dyes have been utilized as triggers, but the majority absorb in the NIR or at shorter wavelengths, resulting in reduced penetration depths. In addition, dyes are susceptible to photobleaching, once again limiting long-term applications.[70-71]

Copper sulfide (CuS) NPs are inorganic, semi-conductor nanoparticles primarily used as photothermal agents due to their photothermal stability.[74-75] CuS NPs are non-cytotoxic, biodegradable, and are cleared within a reasonable time frame.[76] They absorb within the second optical imaging window (1000 nm to 1350 nm), ideal for achieving clinically relevant penetration depths with increased signal-to-noise ratio.[24] One drawback of CuS NPs is their lower extinction coefficient and photothermal efficiency compared to

gold nanoparticles; thereby, requiring significant CuS NP concentrations for enhanced photoacoustic contrast.[77] Fortunately, this limitation is trivial when using CuS NPs in laser-activated PFCnDs. A modest amount of CuS NPs is enough to initiate PFCnD vaporization. The resulting phase-change gives an intense photoacoustic signal and a gaseous PFC microbubble (MB) which provides enhanced ultrasound contrast. Hence, combining CuS NPs with PFCnDs synergistically overcomes limitations associated with CuS NPs and the aforementioned laser-activated PFCnD challenges.

## 3.2 **Methods and Materials**

### *3.2.1 Synthesis of CuS NPs*

Copper sulfide nanoparticles (CuS NPs) were synthesized according to previously described methods.[74] Hydrodynamic size of CuS NPs, measured using a Zetasizer Nano ZS (Malvern), was shown to be ~11 nm, which agreed with TEM images. Citrate-coated CuS NPs were PEGylated via addition of thiolated poly(ethylene glycol) (mPEG-SH, 5 KDa Layson Bio) (1 $mg \cdot ml^{-1}$). The solution was left to react overnight under gentle stirring. The following day the solution was washed of excess PEG using 30 kDa Amicon centrifuge filters and resuspended in DI $H_2O$ at an O.D. of ~10.

### *3.2.2 Comparison of CuS NPs and 1064 nm AuNRs*

Stability of synthesized CuS NPs was compared against 1064 nm absorbing AuNRs. Solutions containing either CuS NPs or AuNR of equal O.D.'s were irradiated at various energies (1064 nm, 10-Hz pulse repetition rate) for 600 pulses (60 s). Afterwards, UV-Vis measurements were taken to study any changes in absorbance spectrum due to alteration in particle shape (i.e. stability).

### *3.2.3 Fluorination of CuS NPs*

To fluorinate CuS NPs, 3.5 ml of CuS NPs at OD ~10 were added to 20 ml of ethanol and 300 µl of 1H, 1H, 2H,2H-Perfluorodecanethiol (Sigma). The solution was stirred and left to react overnight. After 24 hours, fluorinated CuS NPs were washed in a 50 kDa Amicon centrifuge filters at 1000 rcf for 10 minutes. The remaining solution, <1 ml, was placed under reduced pressure (Buchi Rotavapor) to remove any remaining ethanol

or excess perfluorodecanethiol and leave a film of fluorinated CuS NPs. One ml of PBS was added to the dried CuS NPs and sonicated to resuspend the CuS NPs. Spectrums of PEGylated CuS NPs and fluorinated CuS NPs were taken on an Evolution 220 UV-Vis Spectrophotometer (Thermo Fisher). Zeta potential measurements to ensure successful coatings were taken with a Zetasizer Nano ZS.

### *3.2.4 Synthesis of CuS-PFCnDs*

Synthesis of CuS-PFCnDs was modified from previously developed methods.[4, 72, 78] Briefly, 50 µl of perfluoropentane (FluoroMed L.P.) and 150 µl of 1% v/v Zonyl FSO fluorosurfactant (Sigma) were added to the resuspended CuS NPs. The solution was vortexed for 10 seconds and sonicated in an ice-cold ultrasonic water bath (VWR, 180 W) for 5 minutes or until the solution became milky with minimal excess perfluoropentane solution. CuS-PFCnDs were centrifuged at 100 rcf for one minute to remove any excess CuS NPs that aggregated and remained in solution. The supernatant was taken and further washed at 1000 rcf for 5 minutes to get rid of any excess CuS NPs in solution. Hydrodynamic size of CuS-PFCnDs was characterized with a Zetasizer Nano ZS after the washing steps.

### *3.2.5 USPA Image acquisition*

All imaging experiments were conducted using a 40-MHz ultrasound and photoacoustic imaging probe (LZ-550, Visualsonics Inc.) coupled to a combined ultrasound and photoacoustic imaging system (Vevo LAZR, Visualsonics Inc). The laser was operated at 1064 nm wavelength producing 5-7 ns laser pulses at 20-Hz pulse repetition rate. The fluence was measured to be between 6-9 $mJ \cdot cm^{-2}$.

### *3.2.6 Phantom preparation*

A poly(acrylamide) tissue mimicking phantom with a pipette inclusion was constructed as previously described by our group.[70] Briefly, 40% acrylamide solution was mixed with water, ammonium persulfate and tetramethylethylenediamine. The mixture was poured into a mold and allowed to solidify around a pipette fixed in place to create a void for future pipette insertion.

### *3.2.7 Phantom imaging*

CuS-PFCnDs were diluted (2.0% v/v) in PBS. The solution was pipetted out and the pipette with solution was placed within the void of the phantom (Figure 2). The imaging probe, placed above the phantom, was acoustically coupled to the phantom using ultrasound gel. The probe was positioned such that the optical focus occurred at the center of the pipette's cross section. Ultrasound B-mode and photoacoustic (1064 nm) images were collected simultaneously for 100 frames at a rate of 5 fps.

### *3.2.8 Comparison of CuS- and AuNR-PFCnDs activation at different depths*

To demonstrate the advantages of CuS-PFCnDs, the generated PA amplitude of CuS-PFCnDs to AuNR-PFCnDs were compared at different imaging depths. The synthesized AuNRs had a peak absorbance at 800 nm. To prepare the different PFCnDs, CuS NPs and AuNR solutions of the same O.D. (10) were fluorinated. Next, PFP and a stabilizing shell (bovine serum albumin in PBS) were added and the mixture was sonicated until PFCnDs formed. To ensure a fair comparison, CuS-PFCnDs and AuNR-PFCnD sizes were characterized with a Zetasizer Nano ZS and found to both be within 5% of each other.

Additionally, a plate reader was used to ensure roughly equal concentrations of the two types of PFCnDs, based on absorbance.

To compare the vaporization ability at increasing depths of CuS-PFCnDs and AuNR-PFCnDs, a flow phantom was designed where different levels of milk could be added. The milk levels were used to mimic tissue absorbance properties, with higher levels of milk corresponding to deeper imaging depths. To detect vaporization, a 20 MHz transducer (Visualsonics MS250) was placed at a fixed distance below the sample. A gelatin layer (8% wt/vol) containing graphite particles was placed on top of the transducer in order to protect it from direct laser irradiation that could produce image/signal artifacts. Above the graphite-gelatin layer was a pure gelatin layer (8% wt/vol) with thin-wall silicone tubes running horizontally and perpendicular to the imaging plane of the ultrasound transducer.

During laser irradiation, the imaging samples, containing either CuS-PFCnDs or AuNR-PFCnDs, were stationary or flowing through the tubes at 2 $ml \cdot min^{-1}$. The flow rate was controlled by a syringe pump (Fusion 400, Chemyx Inc.). The flow phantom ensured that unvaporized PFCnDs entered the imaging plane at each photoacoustic frame, thereby allowing vaporization-associated photoacoustic signal comparison between CuS-PFCnDs and AuNR-PFCnDs. A Vibrant laser (Opotek) operating at the particle's peak absorption, either 800 nm for AuNR-PFCnDs or 1064 nm for CuS-PFCnDs, was used to irradiate the sample from above. The laser produced 5-7 ns laser pulses at a 10-Hz repetition rate. Fluences for each wavelength were chosen based on the allowed American National Standards Institute (ANSI) limits, i.e., 32 $mJ \cdot cm^{-2}$ for 800 nm and ~100 $mJ \cdot cm^{-2}$ for 1064

nm.[79] Milk was added in increments of 0.25 cm until a final height of 3.0 cm of milk between the laser air-beam and the sample was reached. At each milk height, photoacoustic signal was captured under no flow and under flow conditions. The photoacoustic signal during the no flow condition was averaged and subtracted from the average photoacoustic signal during flow to calculate the vaporization-associated photoacoustic signal. This value was then normalized to the smallest milk height (0.25 cm) for the respective groups. In some cases, when there was no vaporization occurring, fluctuations in the photoacoustic signal resulted in slightly negative PA% values.

### *3.2.9 In vivo imaging*

Studies conducted adhered to approved protocols by the Institutional Animal Care and Use Committee at Georgia Institute of Technology. Mice (nu/nu) were anesthetized using a combination of isoflurane (1.5-2.5%) and $O_2$ (0.8 $L \cdot min^{-1}$). For all *in vivo* studies, 150 µl of as-prepared CuS-PFCnDs were injected intravenously through the jugular vein.

#### 3.2.9.1 Spleen imaging

CuS-PFCnDs were first tested in a murine spleen to verify they could provide significant photoacoustic and ultrasound contrast. After particle injection, 30 minutes was allotted to allow for circulation and uptake of CuS-PFCnDs by the reticuloendothelial system (RES). The spleen was then localized, imaged at 1064 nm and USPA data was collected.

#### 3.2.9.2 Dermatitis murine model: Lymph node imaging

A murine exhibiting spontaneous dermatitis was used to study CuS-PFCnDs in a more applicable *in vivo* model. The inguinal lymph node was localized using ultrasound and Doppler imaging. Ultrasound images of the lymph node were taken after CuS-PFCnD injection but before CuS-PFCnD laser activation to ensure no spontaneous vaporization of the CuS-PFCnDs. Two minutes after injection, the lymph node was irradiated at 1064 nm and USPA images were collected for one minute. Following the irradiation, ultrasound images were taken at distinct time points to monitor the change in CuS-PFCnD-enhanced ultrasound contrast over time.

### *3.2.10 Background-free imaging algorithm*

The unique temporal photoacoustic and ultrasound signal of laser-activated CuS-PFCnDs was exploited through image processing. Following laser induced vaporization, pixels containing phase-changed PFCnDs exhibit a decay in photoacoustic signal, and an increase in ultrasound signal. Using a developed algorithm that identifies pixels which exhibit the characteristic photoacoustic and/or ultrasound trend, and discards endogenous signal and/or noise, results in a clear map of PFCnD locations. Overlaying the produced PFCnD localized image over an ultrasound image, for anatomical reference, results in an easy visualization of CuS-PFCnDs. Although initially developed for CuS-PFCnDs, the image processing can be applied to other laser-activated PFCnDs. Please refer to **Appendix A** for a more detailed explanation of the algorithm, and examples regarding photoacoustic- and ultrasound-based background-free image production.

## 3.3 Results

### *3.3.1 Synthesis and fluorination of CuS NPs*

CuS NP absorbance depends on d-d transition;[77] therefore, fluorination of CuS NPs did not significantly alter their characteristic UV-Vis spectrum, ability to absorb at 1064 nm or their structure (Figure 3a, b). However, differences in surface charge were observed after fluorination (Figure 3c). Following successful surface coating, CuS NPs became soluble in perfluorocarbon solutions for future inclusion in nanodroplets (Figure 3d).

### *3.3.2 Synthesis of CuS-PFCnDs*

Upon sonication, an emulsion of PFCnDs with incorporated CuS NPs was formed. There were unencapsulated CuS NPs that were washed away during the centrifugation steps. However, the remaining PFCnDs had a blue hue, indicative of CuS NP presence. The CuS-PFCnDs were monodisperse (polydispersity index <0.15) with a mean hydrodynamic size of 250 nm (Figure 3e). Given that Zonyl FSO has a highly hydrophilic head, the zeta potential of synthesized CuS-PFCnDs is relatively neutral, -7.04 +/-1.01 mV.

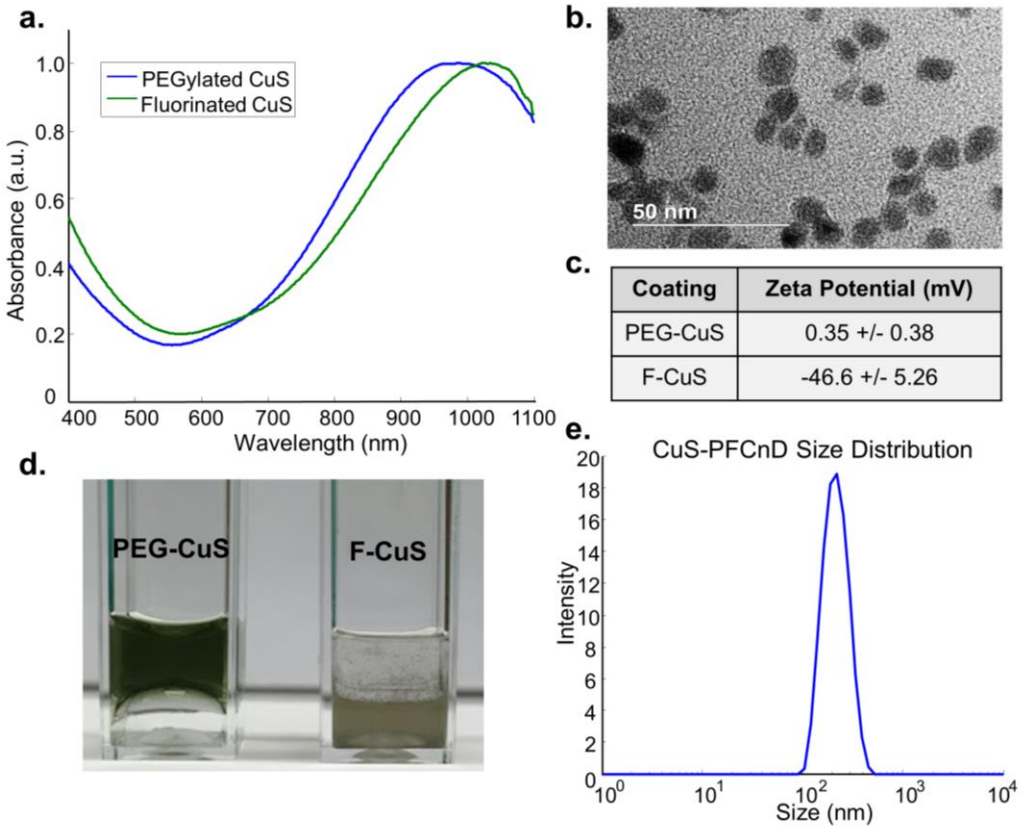


| Coating | Zeta Potential (mV) |
|---|---|
| PEG-CuS | 0.35 +/- 0.38 |
| F-CuS | -46.6 +/- 5.26 |

**Figure 3.** (a) Fluorination of CuS NPs did not significantly alter their spectrum or (b) their size and structure, shown by TEM images. (c) Successful coating was confirmed by measuring particle zeta potential at each step. (d) After fluorination, CuS NPs were soluble within PFC solution (lower layer) while PEGylated CuS NPs remained in PBS. (e) Hydrodynamic size was measured using dynamic light scattering shortly after sample preparation. Synthesized CuS-PFCnDs were monodisperse with an average size of 250 nm.

### *3.3.3 Comparison of CuS NPs to AuNRs following pulsed irradiation*

CuS NPs have increased photothermally stability compared to AuNRs, an important characteristic for PFCnD applications requiring repeated vaporization events. CuS NPs are more thermodynamically stable than AuNRs because of their spherical shape.[80] Therefore, despite repetitive pulsed-laser irradiation at high fluences, their UV-vis spectrum remains unchanged. This is in contrast to 1064 nm absorbing AuNRs' spectrum, which begins to shift left as nanorods are converted into spherical particles (Figure 4).

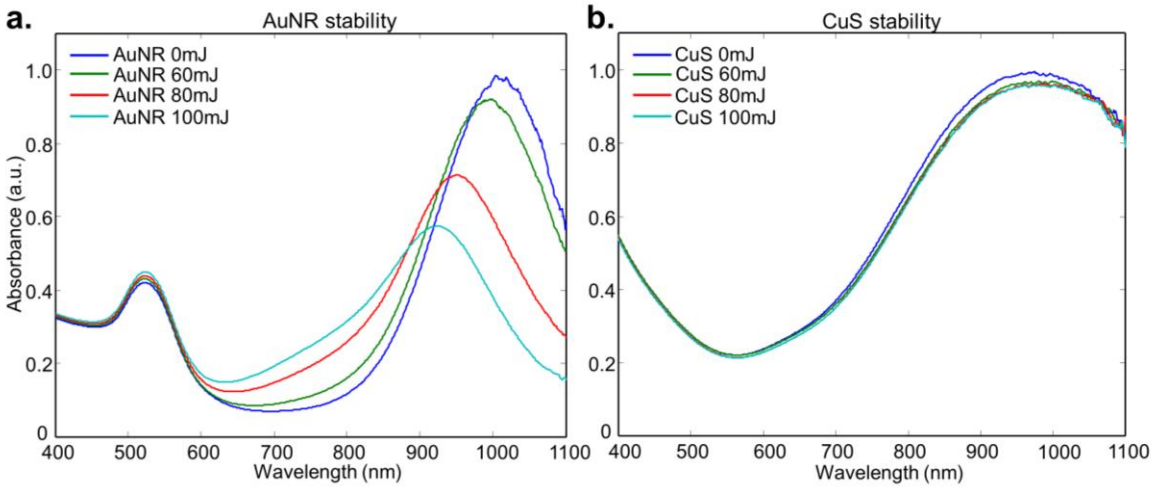


**Figure 4.** Solutions of AuNRs and CuS NPs of equivalent optical densities were irradiated (number of pulses = 600) at different energies. (a) Laser irradiation affected AuNR stability, which led to altered spectrum and reduced ability to absorb at 1064 nm. (b) CuS NP spectrum was not affected by laser irradiation, even at the highest energies, confirming CuS NP photothermal stability.

### *3.3.4 Tissue-mimicking phantom studies*

#### 3.3.4.1 CuS-PFCnDs photoacoustic and ultrasound response

Synthesized CuS-PFCnDs provided dramatic photoacoustic and ultrasound enhancement. Prior to laser irradiation, ultrasound imaging of the sample revealed no ultrasound contrast, confirming their stability. Fluences of 6-9 $mJ \cdot cm^{-2}$ proved enough to activate the CuS-PFCnDs and cause their characteristic photoacoustic signal decay and ultrasound enhancement (Figure 5). With laser-activated PFCnDs, it is easy to distinguish the PFCnD vaporization photoacoustic signal from the photoabsorber signal due to the former's significantly higher intensity. Upon irradiation, the majority of PFCnDs are vaporized, resulting in a strong, immediate photoacoustic signal (Figure 5b, top panel - PA column). Subsequent laser pulses produce a reduced photoacoustic signal mainly attributed to CuS NPs and a small portion of leftover CuS-PFCnDs (Figure 5b, middle and lower panels - PA column). The result is an exponential decay in photoacoustic signal over time (Figure 5c). As expected, the ultrasound contrast exhibits the inverse effect, rapidly increasing as the nanodroplets are converted into stable microbubbles (Figure 5b, US column). After a few laser pulses, the area becomes saturated with microbubbles and the ultrasound contrast plateaus at a maximum (Figure 5d).

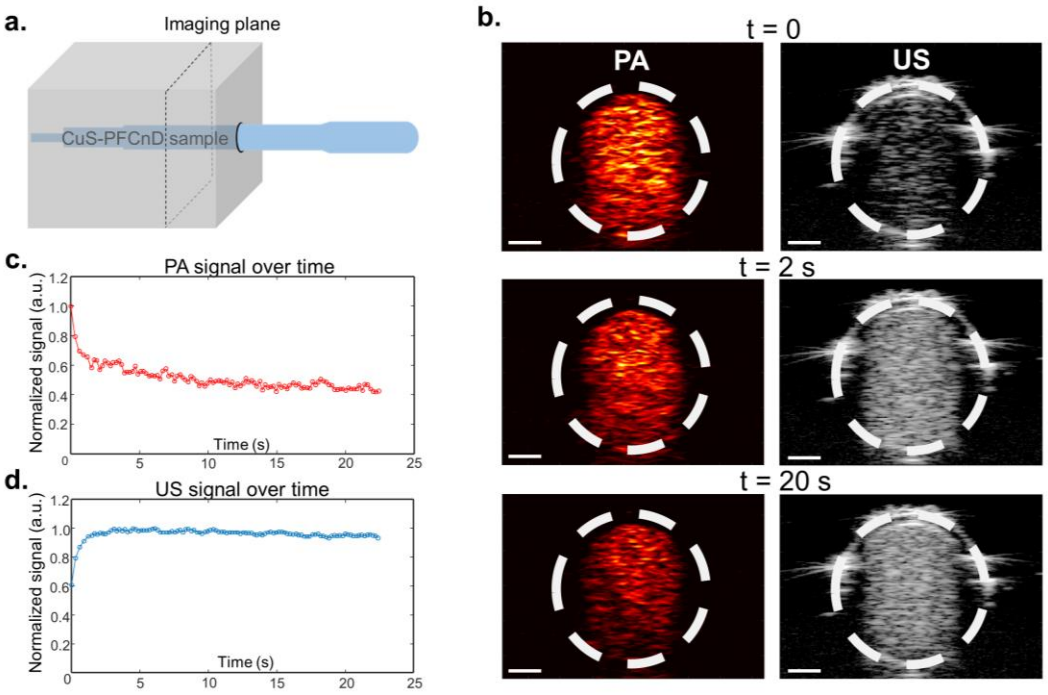


**Figure 5.** (a) Schematic of phantom and imaging setup. The 2-D imaging plane is indicated by the dashed square. The laser irradiation is applied from the top of the phantom. (b) Photoacoustic and ultrasound imaging frames show the difference in contrast at various time-points throughout laser irradiation; pulse repetition frequency of 20 Hz. (c) Typical of PFCnD vaporization, photoacoustic signal rapidly decays while (d) ultrasound contrast rapidly increases. Scale bars = 1 mm.

### 3.3.4.2 Comparison of CuS-PFCnDs to traditional laser-activated PFCnD

Different levels of milk were used to mimic optical properties of tissue and assess how penetration depth affected PFCnD activation ability (Figure 6a). At the lowest level of milk, photoacoustic signal was increased during flow conditions for both samples, indicative of successful PFCnD vaporization (Figure 6b). However, AuNRs-PFCnDs could no longer be activated at 1.75 cm of milk; whereas, CuS-PFCnDs retained 40% of their vaporization capability at a depth of 3 cm (Figure 6c).

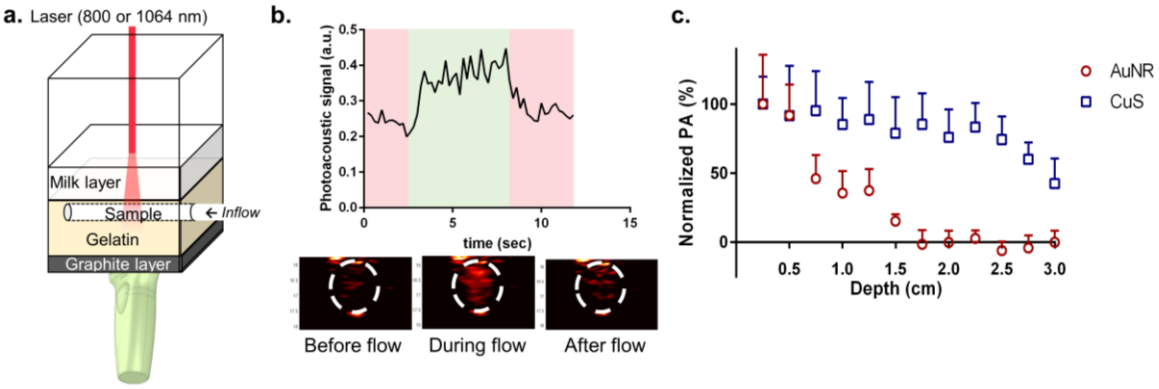


**Figure 6.** (a) Schematic of the flow-phantom design used for capturing photoacoustic signals at different depths of milk. (b) The photoacoustic signal during no flow, indicated by the pink regions, is largely attributed to the photoabsorber within the PFCnDs. During flow (green), the photoacoustic signal increases as a result of the intense vaporization event. (c) The change in PA% was calculated by subtracting the photoacoustic signal under no flow from the vaporization signal during flow, and then normalized to the smallest milk height. CuS-PFCnDs outperform Au-PFCnDs in vaporization abilities as imaging penetration is increased.

### *3.3.5 In vivo imaging*

#### 3.3.5.1 CuS-PFCnD characterization in a murine spleen

CuS-PFCnDs provide distinct ultrasound and photoacoustic signal *in vivo.* Due to their size and biocharacteristics CuS-PFCnDs primarily accumulate in the red pulp tissue of the spleen.[81-82] This was confirmed by significant photoacoustic/ultrasound signal after irradiation at 1064 nm. Both the photoacoustic and ultrasound signals were processed with the developed algorithm (see **Appendix A** for detailed description) and background-free images were formed indicating PFCnD accumulation and activation throughout the spleen (Figure 7).

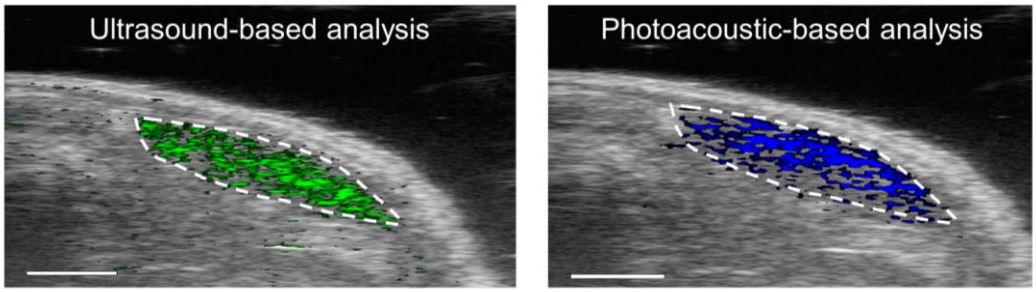


**Figure 7.** CuS-PFCnDs primarily accumulate in the spleens. Thirty minutes after injection the spleen was imaged and USPA data collected. (a) Background-free ultrasound images are obtained using the developed image processing algorithm clearly localizing CuS-PFCnDs within the spleen. (b) By applying a similar processing algorithm to the collected photoacoustic data we are also able to produce a background-free photoacoustic image. Scale bars = 2 mm.

#### 3.3.5.2 Lymph node imaging in a murine dermatitis model

Given the advantages of CuS-PFCnDs, they were tested in a model of higher clinical relevance, specifically a spontaneous dermatitis murine model. Prior to injection, the enlarged inguinal lymph node was located using grayscale and color Doppler ultrasound imaging (Figure 8). After systemic injection, the particles were allowed to circulate for a few minutes, and then 1064 nm pulsed laser irradiation was started resulting in an increase of photoacoustic and ultrasound signals (Figure 9a, middle panel). After the initial laser pulse, there was the characteristic increased in photoacoustic signal which decayed over time as more laser pulses were applied. Coupled with photoacoustic signal decrease, there was a rapid increase in ultrasound signal from the lymph node. The changes in both photoacoustic and ultrasound signal are similar to what was seen in tissue models and in the spleen, suggesting that a portion of CuS-PFCnDs remained within the 2-D imaging plane, becoming entrapped either within vessels or in lymph node tissue. Given that the vasculature of an inflamed lymph node becomes hyperpermeable, it is possible some CuS-PFCnDs were able to extravasate. This hypothesis is supported by the ultrasound enhancement seen throughout the entire volume of the lymph node and ultrasound contrast persistence for several minutes (Figure 9, Figure 10).

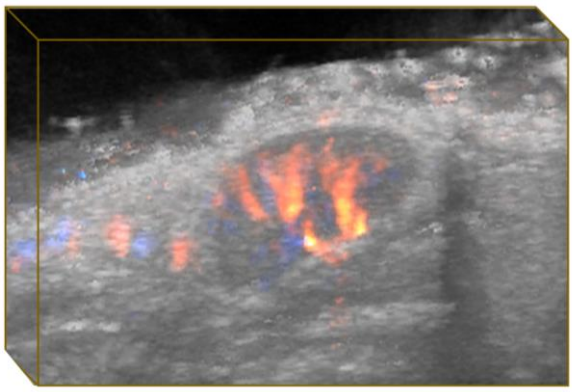

**Figure 8.** 3-D Doppler image demonstrating the enlarged inguinal lymph node and dilated vasculature.

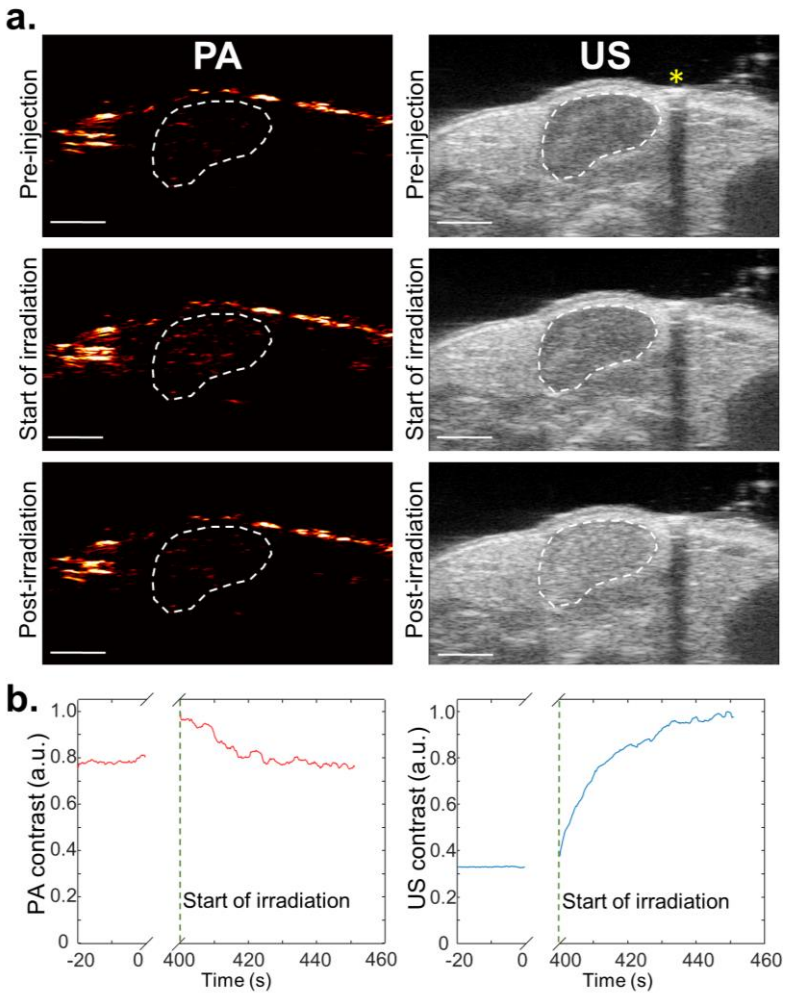


**Figure 9.** (a) Photoacoustic and ultrasound images of the lymph node before injection (top), after injection and upon starting laser irradiation (middle), and at the end of irradiation (bottom) show successful vaporization of CuS-PFCnDs and increased photoacoustic and ultrasound contrast throughout the lymph node. The yellow star denotes a bubble used as a marker for ensuring the same 2D imaging plane was maintained before and after injection. (b) Changes in photoacoustic and ultrasound contrast prior to CuS-PFCnD injection and then after injection at the start and end of the laser irradiation period. The photoacoustic and ultrasound contrast seen after irradiation are similar to observations in tissue models. Scale bars = 2 mm.

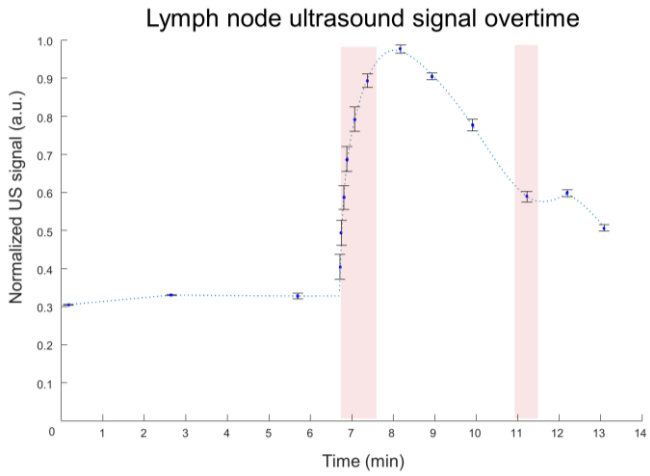


**Figure 10.** Ultrasound signal after period of lasing (red regions indicate when the laser is on). Ultrasound signal persists for several minutes and gradually falls as PFC diffuses out of PFCnDs or created MBs are washed out of plane.

The background-free image algorithm was applied to better understand CuS-PFCnD distribution within the lymph node. Interestingly, the photoacoustic analysis was unable to localize vaporized CuS-PFCnDs as clearly as in the spleen. This is likely due to the lower CuS-PFCnD concentration in the lymph node and the fact that a portion of the flowing CuS-PFCnDs are activated by scattered laser light outside of the ultrasound imaging plane. The combination of these factors results in a reduced amount of CuS-PFCnDs photoacoustic response within the imaging plane. Fortunately, as CuS-PFCnDs simultaneously provide sustained, enhanced ultrasound contrast, they could clearly be identified by applying the ultrasound-based image processing. CuS-PFCnDs were localized throughout the lymph node and surrounding vasculature (Figure 11a). Areas containing activated CuS-PFCnDs show an increase in ultrasound signal of up to 70%, whereas those without CuS-PFCnDs show negligible contrast change over time (Figure 11).

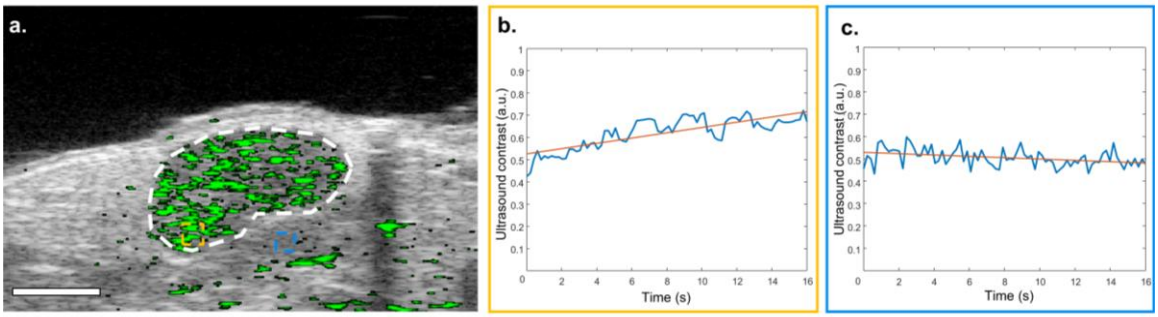


**Figure 11.** Ultrasound-based image processing, based on the pixel's positive slope (yellow versus blue ROIs), selectively identifies CuS-PFCnDs throughout the lymph node. Scale bar = 2 mm.

## 3.4 Discussion

Use of CuS NPs as photoabsorbers imparts several benefits for PFCnDs. CuS NPs exhibit photoacoustic contrast as deep as five centimeters due to their extended NIR absorbance.[83] This signifies that CuS-PFCnDs can be activated at increased depths over other laser-activated PFCnDs, which was verified with the comparison to 800nm AuNR-PFCnDs. Considering that depth penetration is one of the biggest limitations in USPA imaging, this presents a significant advancement.

Another benefit of CuS NPs as the photoabsorber, is that they have shown biodegradability *in vivo*, overcoming concerns of long-term toxicity and biocompatibility that other inorganic particles face. One study directly compared long-term bioeffects of CuS NPs and Au NPs and showed that one month after systemic injection 90% of CuS NPs were excreted versus only 4% of Au NPs.[76] Alternatively, CuS NPs can be synthesized at sizes that pass through the renal system for rapid clearance, and still possess absorbance in the extended NIR.[84-85]

The ability of systemically injected CuS-PFCnDs to dramatically enhance USPA contrast presents several opportunities. In regards to clinical applications, CuS-PFCnDs were able to provide contrast throughout the entirety of an inflamed lymph node. Ultrasound images show that phase-changed CuS-PFCnDs accumulate in the lymph node and persist for several minutes afterwards. The sustained contrast suggests that a portion of the produced MBs get stuck in small capillaries or in the lymph tissue, a result of PFCnDs extravasating the inflamed vasculature. Morphological changes experienced during inflammatory diseases, such as lymphangiogenesis and vasculature remodeling,

closely resemble changes seen in pre-metastatic lymph nodes.[86-90] Therefore, CuS-PFCnDs may be used to uncover diseased lymph nodes based on the extent of CuS-PFCnD signal seen throughout the vasculature. This method provides different information, relevant to vasculature changes, from the traditional subcutaneous injections used to study lymphatic transport. Additionally, intravenous injections overcome certain limitations associated with subcutaneous injection of larger particles (> 100 nm), where the majority remain entrapped at the injection site, struggling to directly enter the lymphatics and consequently, the lymph node.[91-93] Although, the ability of particles to enter the lymph node from the vasculature needs to be further examined, CuS-PFCnDs could still be able to highlight the vasculature changes associated with certain diseases. However, it is important to consider the model being utilized, as pre-metastatic vascular remodeling can vary.[90]

CuS-PFCnDs also have potential applications in areas outside of the lymph node. Their natural tendency to accumulate in the red pulp tissue of the spleen, where they are eventually endocytosed by resident red pulp macrophages (RPMs), could help elucidate RPM's response *in vivo*. Recently, RPMs have shown the ability to present antigens to T-cells *in vitro*, but studies regarding RPMs *in vivo* role are needed.[94]

# CHAPTER 4. AIM 2: MULTICOLORED PERFLUOROCARBON NANODROPLETS FOR MULTIPLEXED ULTRASOUND/PHOTOACOUSTIC IMAGING

## 4.1 Introduction

For several decades, diagnostic agents have been judged on their ability to differentiate diseased versus healthy tissue. As knowledge regarding tissue heterogeneity and its implications increased, [95-97] so too has the demand for *in vivo* diagnostic platforms capable of conveying more detailed information. Multiplexed imaging, the ability to simultaneously visualize functional parameters and/or molecular targets using one imaging modality, is well-suited to accomplish this task. To date optical based modalities have offered the most robust multiplexing abilities due to the availability of diverse imaging probes.[98] However, the limited depth penetration of optical modalities greatly restricts their clinical utility.[98-99] Hence, great attention has been placed on increasing the multiplexing abilities of clinical relevant imaging modalities. Thus far, nuclear medicine has shown that it can effectively differentiate various phenotypes by selective targeting with various radiometals.[98, 100] However, the acquisition time associated with multiplexed positron emission tomography (PET) or single-photon emission computed tomography (SPECT) can be lengthy, i.e., several minutes. Additionally, since PET or SPECT are typically combined with MRI or CT imaging,[98] there are concerns of high-costs and/or safety regarding repetitive imaging feasibility.[41] To address these limitations, I have engineered a platform for multiplexed ultrasound and photoacoustic (USPA) imaging based on laser-activated perfluorocarbon nanodroplets (PFCnD).

The innovative platform consists of multicolored, laser-activated PFCnDs and USPA imaging to noninvasively provide multiplexed and even, multimodal contrast. The platform relies on encapsulating unique photoabsorbers into distinct PFCnD subpopulations, where-upon user-specified laser irradiation can selectively activate PFCnD subgroups to induce USPA contrast. After successfully showing the platform's feasibility, I demonstrate its potential in a mouse model of a tumor-draining lymph node. The multiplexed imaging capabilities of multicolored PFCnDs helped elucidate distinct lymphatic trafficking mechanisms, i.e. intravascular versus intradermal, in a single imaging session. Additionally, multicolored PFCnDs's helped uncover *in vivo* PFCnD characteristics that significantly expand their potential uses. Future iterations of the presented platform will focus on targeting PFCnD subpopulations towards different receptors to provide comprehensive anatomical and molecular information of diseased tissue.

## 4.2 Materials and Methods

### *4.2.1 Synthesis of multicolored PFCnDs*

UV-Vis spectrophotometry (Evolution 220; Thermo Scientific) confirmed the selected hydrophobic dyes (Epolight 9151, Epolight 3832; Epolin, Inc.) had absorption spectra with minimal overlap. Perfluoropentane (FluoroMed, L.P.) was used for the PFCnD core and a mixture of phospholipids was used for the stabilizing shell. To synthesize the colored PFCnDs, 20 µl of 1,2- distearoyl-sn-glycero-3-phosphocholine (DSPC, 10 mg/mL; NanoCS Inc.) and 15 µl of 1,2-distearoyl-sn-glycero-3-phosphoethanolamine-N-[amino(polyethylene glycol)-2000] (DSPE-PEG(2000), 25 mg/ml; Avanti Polar Lipids, Inc.) lipids in chloroform, were added to a 50 ml pear shaped flask. Dye solutions were prepared in chloroform (1 mg/ml), and 100 µl of the desired dye was added to the lipid solution. Finally, 2 ml of chloroform were added to the flask to facilitate the production of a smooth lipid cake. The flask was placed under reduced pressure (Rotavapor; BÜCHI Labortechnik) to remove the chloroform, and the result was a thin, colored lipid cake. One ml of PBS was added to the flask and sonicated (VWR, 180 W) to resuspend the lipids and dye and create micelle structures. The solution was transferred to an 8 ml scintillation vial and 75 µl of perfluoropentane were added. The vial was vortexed and sonicated in ice-cold water (VWR, 180 W) until the solution became milky and there was no remaining perfluoropentane bolus visible. The resulting PFCnDs were washed to remove excess dye by placing the solution in a 1.5 ml microcentrifuge tube and centrifuging them at 100 rcf for one minute. The supernatant was pulled off, leaving any aggregated dye behind. The same synthesis process was repeated with the other dye, and the two synthesized droplet sets were kept separately for characterization.

In studies requiring fluorescently labeled particles, PFCnDs were synthesized according to the same protocol, but an additional 1.6 µl of fluorescent dye (DiI, 3mg/ml; Thermofisher) was added to the lipid-dye-chloroform mixture. Being highly lipophilic, DiI integrates itself within the lipid shell. Synthesized DiI-PFCnDs were tested after synthesis to ensure PFCnD vaporization was not affected.

### *4.2.2 Characterization of multicolored PFCnDs*

A dynamic light scattering instrument (Zetasizer Nano ZS; Malvern Instruments Ltd.) was used to characterize the PFCnDs. For size measurements, 1 ml of a 1:100 stock dilution of PFCnDs in PBS was placed in a plastic cuvette. To study surface charge, 500 µl of a 1:100 PFCnD stock solution in nanopure water (Barnstead Smart2Pure, Thermo Scientific) was placed in a folded capillary zeta cell.

### *4.2.3 USPA image acquisition*

All imaging experiments were conducted using a 40-MHz ultrasound and photoacoustic imaging probe (LZ-550; FUJIFILM VisualSonics Inc.) coupled to a combined ultrasound and photoacoustic (USPA) imaging system (Vevo LAZR; VisualSonics Inc). The tunable Nd:YAG laser operated at either a 680 nm or 1064 nm wavelength producing 5-7 ns laser pulses at a 20-Hz pulse repetition rate. The fluences were measured to be between 12-15 $mJ \cdot cm^{-2}$ at 680 nm and 6-9 $mJ \cdot cm^{-2}$ at 1064 nm, well below the ANSI limits.[79] Ultrasound and photoacoustic images were captured at 5 frames per second.

### *4.2.4 Phantom studies*

#### 4.2.4.1 Assessing selective photoacoustic/ultrasound signal of multicolored PFCnDs

A flow phantom was used to demonstrate that each PFCnD subset provides selective photoacoustic and ultrasound contrast at their respective absorption wavelengths. Considering the PFCnD vaporization is a dynamic event, a dynamic phantom, i.e. flow, helps to easily differentiate between vaporized and unvaporized PFCnDs. To construct the phantom, the face of a clear plastic box was drilled with three equally spaced holes. This process was repeated on the opposite face of the box, and optically and ultrasonically inert silicone tubing (HelixMark; Freudenberg Medical, ID 0.250" OD 0.374") was threaded from one side to the other. The spacing of the tubes ensured all three samples could be irradiated and imaged at the same time, for fair comparison. Solutions (1:100 stock dilution) of 1064 nm-PFCnDs, 680 nm-PFCnDs, and blank PFCnDs (i.e., no dye) were prepared and loaded into separate 10 milliliter syringes. An 18-guage needle and an accompanying 10 milliliter sample-filled syringe were attached to one side of the tubing, enabling flow through the phantom box. A syringe pump (Fusion 400; Chemyx Inc.) controlled the flow rate of samples through the tubes at either 0 $ml \cdot min^{-1}$ (i.e. stationary) or at 2 $ml \cdot min^{-1}$, a velocity which ensured continuously unvaporized sample for each laser pulse. The phantom box was filled with degassed water and the imaging probe was placed perpendicular to the tubes such that the optical focus of the integrated laser fibers was aligned with the cross-sectional area of the tubes. Photoacoustic and ultrasound data were collected for approximately 30 seconds at 680 nm and 1064 nm laser irradiation.

#### 4.2.4.2 Mixture of PFCnDs

Different ratios of 1:100 dilutions of 680 nm-PFCnDs to 1064 nm-PFCnDs (1:3, 2:2, and 3:1) were mixed together and placed in three separate 10 mL syringes. Samples were monitored to ensure settling of PFCnDs did not occur during the imaging process. Using the flow phantom previously described, the samples were irradiated at 680 nm or at 1064 nm while flowing through the tubes at 2 $ml \cdot min^{-1}$ or stationary. For both wavelengths, a region of interest within the center of each tube was selected, and the vaporization-associated photoacoustic signal from each wavelength was determined (n = 10 photoacoustic frames). A period (n = 10 photoacoustic frames) from the stationary baseline photoacoustic signal (i.e., photoabsorber-associated photoacoustic signal) was averaged and subtracted from the averaged vaporization-associated photoacoustic signal. The result allowed for comparison of vaporization-associated photoacoustic signal of each excitation wavelengths across the differing ratios.

### *4.2.5 In vivo imaging*

The subsequently described small animal studies adhered to protocols approved by the Institutional Animal Care and Use Committee at the Georgia Institute of Technology. Mice (nu/nu) were anesthetized with a combination of isoflurane (2.5%) and $O_2$ (1.0 $L \cdot min^{-1}$) and placed on an animal heating pad, regulated at 37°C, during imaging. After acquiring ultrasound and photoacoustic data, the algorithm described in **Appendix A** was performed to produce background-free images.

### *4.2.6 Spleen imaging*

To ensure *in vivo* efficacy of the multicolored PFCnDs, a nu/nu mouse model was utilized. A 1:1 cocktail from stock solutions of the two PFCnD subpopulations was prepared and 150 µl were intravenously injected via the jugular vein. The particles were allowed to circulate for 30 minutes, and then the spleen was imaged at 680 nm and again at 1064 nm. After imaging sessions, mice were either kept for observation or euthanized via $CO_2$ asphyxiation followed by cervical dislocation.

### *4.2.7 In vivo breast cancer model*

4T1 murine breast cancer cells were cultured in Dulbecco's Modified Eagle Medium: Nutrient Mixture F-12 (Invitrogen) supplemented with 10% fetal bovine serum and 1% penicillin/streptomycin. Nu/nu mice were injected with 50 µls of 4T1 cells ($1x10^7$ cells/mL) into the mammary fat pad. Tumor sizes were monitored for several days, and ultrasound imaging was conducted to observe any changes in the draining inguinal lymph node. To study different lymphatic trafficking capabilities of PFCnD, intradermal and intravascular injections were conducted as follows. At 5-6 days after inoculation, 100 µl of 1064 nm-PFCnDs were injected intradermally at the tumor site, while mice were under the aforementioned anesthesia. The particles were slowly injected to prevent drastic pressure changes at the injection site for reducing the risk of premature droplet vaporization or altering particle drainage. At the respective time points (24 or 72 hours), mice were anesthetized again, and the inguinal lymph node was located with ultrasound imaging. A second injection of 100 µl of 680 nm-PFCnDs were injected intravenously through the jugular vein. After 1 minute, USPA images of lymph nodes were obtained by first

irradiating at 1064 nm and then at 680 nm. After imaging was complete, the animals were sacrificed via a sodium pentobarbital based veterinary euthanasia drug (150 mg/kg IP) and cervical dislocation. Lymph nodes were resected and fixed for histology.

### *4.2.8 Intradermally injected PFCnDs trafficking mechanisms*

#### 4.2.8.1 USPA and IVIS imaging

After realizing that intradermal PFCnDs successfully trafficked to lymph nodes, additional studied were conducted to better understand how they are transported. Healthy mice (n = 9) were injected with 100 µl of only 680 nm-PFCnDs in the breast tissue area. At 1.5 (n = 2), 24 (n =4) and 72 (n =3) hours after injection, USPA imaging was conducted and the intensity of photoacoustic signal within the lymph node analysed. The baseline (i.e. endogenous plus photoabsorber signal) was subtracted from the peak photoacoustic signal (i.e. vaporization-associated photoacoustic signal) to compare the difference in vaporization-associated photoacoustic intensity at the different time points. In addition to USPA, IVIS imaging was performed at 24 hours post injection of fluorescently labelled PFCnDs to monitor their spatial distribution (n =2).

### *4.2.9 Functionalization of PFCnDs*

To demonstrate the feasibility of multicolored PFCnDs for use as eventual molecular diagnostic tools, the efficacy of functionalized PFCnDs was studied. A protocol for directional conjugation of antibodies to gold nanoparticles[101] was adapted for PFCnDs (please refer to **Appendix B**) to produce HER2 targeted PFCnDs.

### *4.2.10 Functionalized PFCnDs binding assay*

SKBR3 cells, a HER2 expressing breast cancer cell line, was used for studying HER2 targeted PFCnDs. Cells were cultured in 2-chamber well chamber slides (ThermoFisher). After cells had reached 50-70% confluence, they were stained with CellTracker Green dye (ThermoFisher). Then, 15 µl of either HER2 functionalized or PEGylated PFCnDs (both DiI labelled) were incubated with the cells (1.5 ml media per well). After two hours, cells were washed with PBS several times. Cells were then fixed with 10% formalin for 10 minutes, washed with PBS and coverslips mounted. A Zeiss LSM 700 confocal microscope was used to image the samples.

## 4.3 **Results**

### *4.3.1 Synthesis of Multicolored PFCnDs*

Multicolored PFCnD were synthesized by encapsulating two photoabsorbing dyes with minimally overlapping absorption spectra within distinct lipid-shelled PFCnD subpopulations (Figure 12b). Both PFCnD subsets, which will subsequently be referred to as 680 nm-PFCnDs and 1064 nm-PFCnDs given the wavelength at which they phase-change, were characterized using dynamic light scattering. For multiplexing purposes, it is essential that the PFCnD subpopulations have nearly identical characteristics, excluding the encapsulated photoabsorber, to ensure a fair comparison regarding image contrast, pharmacokinetics and stability for downstream *in vivo* experiments. Accordingly, characterization studies indicated that the subpopulations had a similar hydrodynamic size, 350 nm, and zeta potential, -34.7mV +/- 1.6 (Figure 12b).

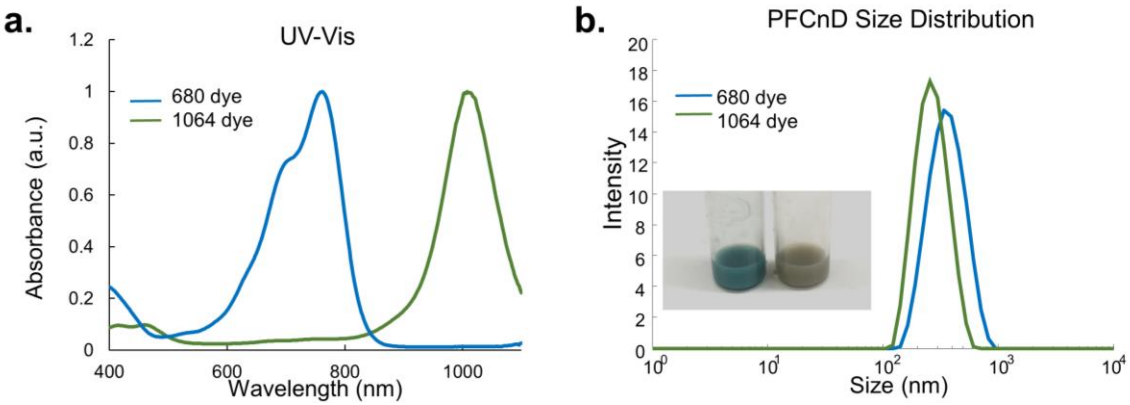


**Figure 12.** (a) UV-Vis of selected dyes showed minimal overlap. (b) The subpopulations had very similar size distributions. Insert shows synthesized multicolored PFCnDs.

### *4.3.2 Selective activation in tissue-mimicking phantom studies*

PFCnD subpopulations selectively responded to tuned pulsed-laser irradiation wavelengths (i.e. 680 nm and 1064 nm). The flow phantom ensured that unactivated PFCnDs could enter the imaging plane at each photoacoustic frame for comprehensively studying the spatiotemporal USPA contrast of the disparate PFCnDs groups (Figure 13a).

At 680 nm laser irradiation, the 680 nm-PFCnD sample vaporized, resulting in the expected intense photoacoustic signal. There was no observable photoacoustic signal from either the blank or 1064 nm-PFCnDs. During flow conditions, the photoacoustic signal of vaporized PFCnDs is increased, but relatively stable, because unactivated PFCnDs are constantly flowing through the laser irradiation plane and being immediately vaporized. Thus, giving off a steady level of vaporization associated photoacoustic signal (Figure 13b,d). Ultrasound signal, on the other hand, is not enhanced because the phase-changed PFCnDs will not exhibit ultrasound enhancement until the produced microbubble reaches a certain size and stability. This occurs out of the imaging plane due to the flow rate utilized. When the flow is stopped, i.e. from 12 to 22 seconds, there are no unactivated PFCnDs to vaporize and thus no new phase-change events occur, resulting in a rapid decrease in 680 nm photoacoustic signal down to a baseline. Ultrasound signal, in contrast, rapidly increases under stationary conditions, because the vaporized PFCnDs have time to accumulate as microbubbles in the imaging plane (Figure 13c,f). Upon irradiation at 1064 nm, an analogous trend in USPA signal was observed for the 1064 nm-PFCnDs sample (Figure 13e,g).

Due to the high energy at 680 nm and slight absorbance of the 1064 nm dye at this wavelength, there was a slight ultrasound enhancement from 1064 nm-PFCnDs (Figure 13f). However, the ultrasound crosstalk was minimal and not accompanied by any observable photoacoustic signal increase. Nonetheless, for later lymph node studies, imaging was first done at 1064 nm then at 680 nm to mitigate this effect.

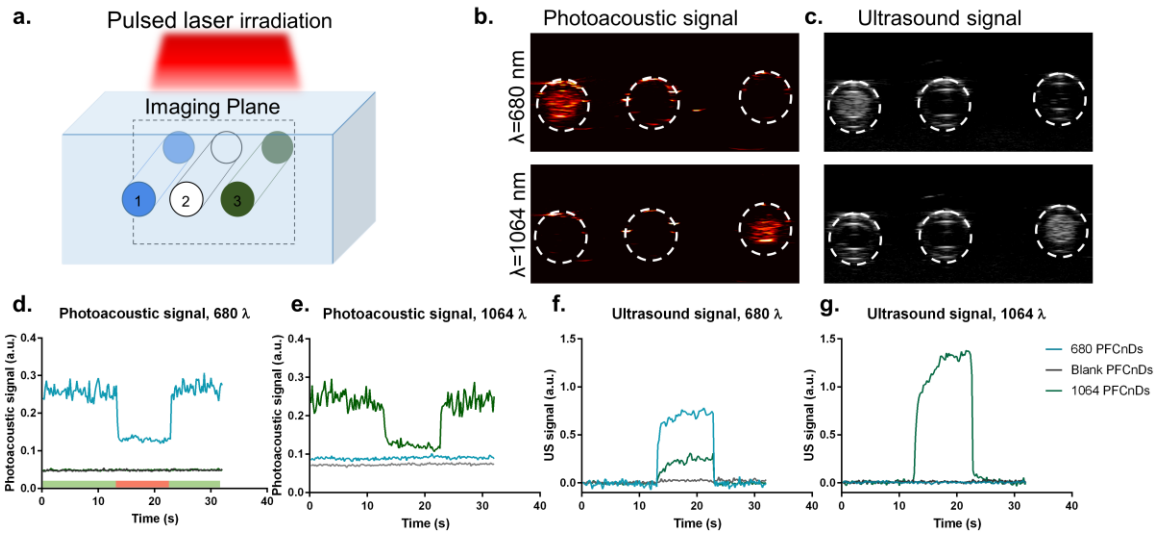


**Figure 13.** (a) Designed flow phantom that allowed for simultaneous imaging of different PFCnD subpopulations. (b) Photoacoustic signal at either 680 nm or 1064 nm only elicits signal from the appropriate PFCnD subpopulation (flow is 2 ml·min$^{-1}$). (c) Ultrasound signal, during 0 ml·min$^{-}$1 flow, shows accumulation of produced MBs. (d-g) Photoacoustic signal and ultrasound signal during the 30 seconds of laser irradiation. Flow starts at 0 seconds and is stopped from 12 to 22 seconds, indicated on graph d by the green (flow on) and red (flow off) regions. During this time photoacoustic signal drops and ultrasound signal increases in the activated subpopulations.

### *4.3.3 Quantitative photoacoustic imaging*

PFCnDs can convey information regarding quantities of subpopulations by comparing relative photoacoustic signals. Different mixtures of varying 680 nm-PFCnDs to1064 nm-PFCnD ratios exhibited photoacoustic intensity from each wavelength (680 and 1064 nm) that corresponded to the relative proportion of phase-changed PFCnDs (Figure 14). At increasing ratios of 680 nm-PFCnD to 1064 nm-PFCnD, the photoacoustic signal at 680 nm laser irradiation increased, while the photoacoustic signal at 1064 nm decreased (Figure 14b). Analogously, higher relative concentrations of 1064 nm-PFCnD corresponded to increased 1064 nm photoacoustic signal and decreased 680 nm signal.

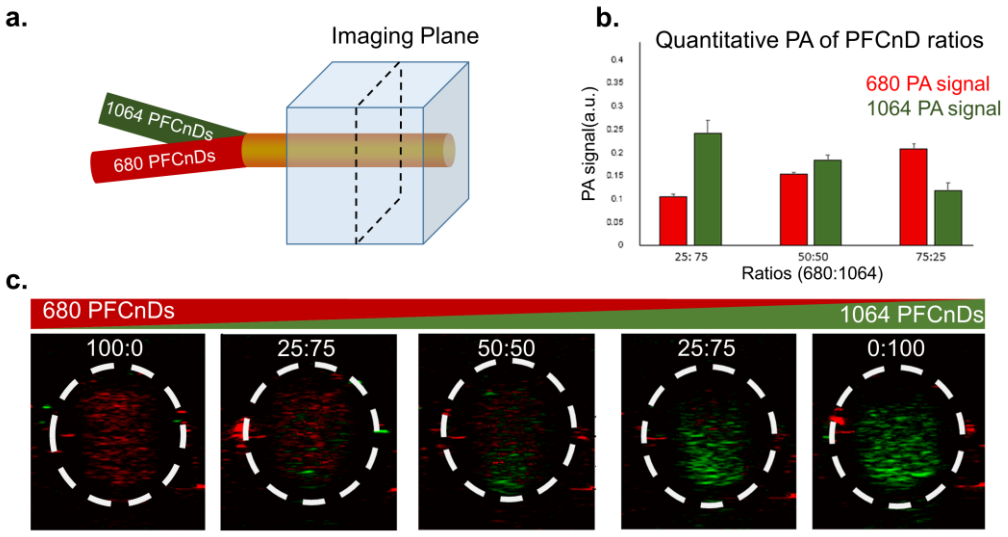


**Figure 14**. (a) Different mixtures of 680 nm-PFCnDs to 1064 nm-PFCnDs were imaged in a flow phantom. (b) Photoacoustic signal at either 680 nm or 1064 nm was correlated to the amount of PFCnD subpopulation present. (c) Images of the first photoacoustic frame show how the signal changes as PFCnD subpopulations concentrations are changed (red: 680 nm photoacoustic signal, green: 1064 photoacoustic signal).

### *4.3.4 Image-processing techniques with multicolored PFCnDs*

The dual contrast of laser-activated PFCnDs allows versatile image processing techniques that enhances the robustness of the platform. Please refer to **Appendix A** for a detailed explanation on background-free image construction.

Laser-activated PFCnDs have unique spatiotemporal photoacoustic and ultrasound signals; therefore, either, or both, data set can be processed to form background-free images. Often, either photoacoustic or ultrasound signal is superior due to factors such as PFCnD location, concentration and endogenous contrast. To demonstrate this phenomenon in relation to multicolored PFCnDs, a mouse spleen was studied and the USPA contrast following 680 and 1064 nm light irradiation examined. Following pulsed 680 nm laser irradiation, the 680 nm-PFCnD group exhibited USPA contrast. Since the PFCnDs have a fixed location, their photoacoustic signal is at a maximum following the first laser pulse, i.e. vaporization-associated signal, and then rapidly decreases to a baseline. However, there was a lot of endogenous photoacoustic contrast as well (Figure 15a). Ultrasound signal exhibited the inverse effect; rapidly increasing over time as more microbubbles were formed. Processing the ultrasound data led to a background-free image of the 680 nm-PFCnDs, that is much cleaner than the original photoacoustic image (Figure 15b).

Next, irradiation at 1064 nm activated the 1064 nm-PFCnD group. Due to the high baseline ultrasound signal from the previously produced microbubbles, PFCnD phase-change based on ultrasound signal alone was not possible; however, the PFCnD vaporization-associated photoacoustic signal remains largely unaffected and after using the developed algorithm to distinguish it from endogenous signal/noise, a similar background-

free image is produced (Figure 15d). Thus, multiple sets of colored PFCnDs can be readily distinguished from one another based on user-controlled inputs and processed with the best-suited modality.

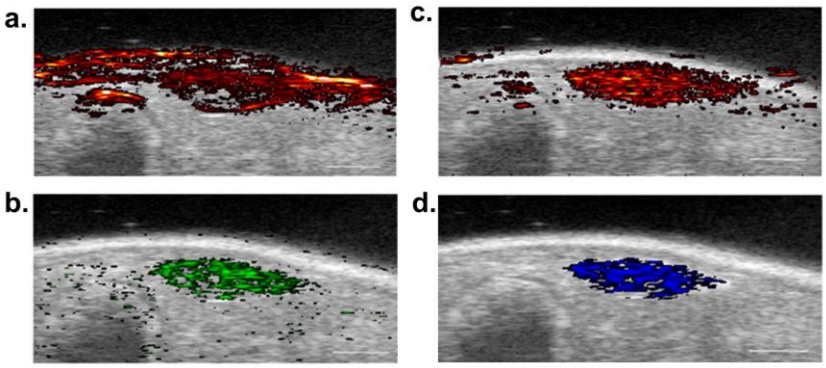


**Figure 15.** (a) Photoacoustic imaging of the spleen at 680 nm overlaid on an ultrasound image. (b) Upon processing the ultrasound data, a background-free image is produced that more clearly conveys the location of vaporized PFCnDs. (c) Photoacoustic imaging of the spleen at 1064 nm overlaid on an ultrasound image. (d) Photoacoustic-based image processing of the 1064 nm irradiated sample reduces endogenous signal and noise. Scale bars = 2 mm.

### *4.3.5 Lymph node imaging with multicolored PFCnDs*

To highlight a more clinically relevant application, distinct lymph node trafficking mechanisms were studied using multicolored PFCnDs. For both the 24-hour and 72-hour time-points, both PFCnD subpopulations were successfully activated after irradiation at their corresponding wavelengths; however, they were distinctly localized in the lymph node (Figure 16). The intravenously injected PFCnDs (680 nm-PFCnDs), introduced moments before imaging, were located throughout the majority of the lymph node, given its extensive vascular bed.[102] Photoacoustic-based background free-imaging was performed to localize the 680 nm-PFCnDs (Figure 16-middle column), although they also exhibited ultrasound contrast. Interestingly, the intradermal injected PFCnDs (1064 nm-PFCnDs), injected either 24 or 72 hours before imaging, only exhibited photoacoustic signal and were confined to one area of the lymph node, specifically on the side proximal to their injection site (Figure 16, first column). For the 24-hour time-point, there was also PFCnD-associated signal in what appeared to be a lymphatic vessel.

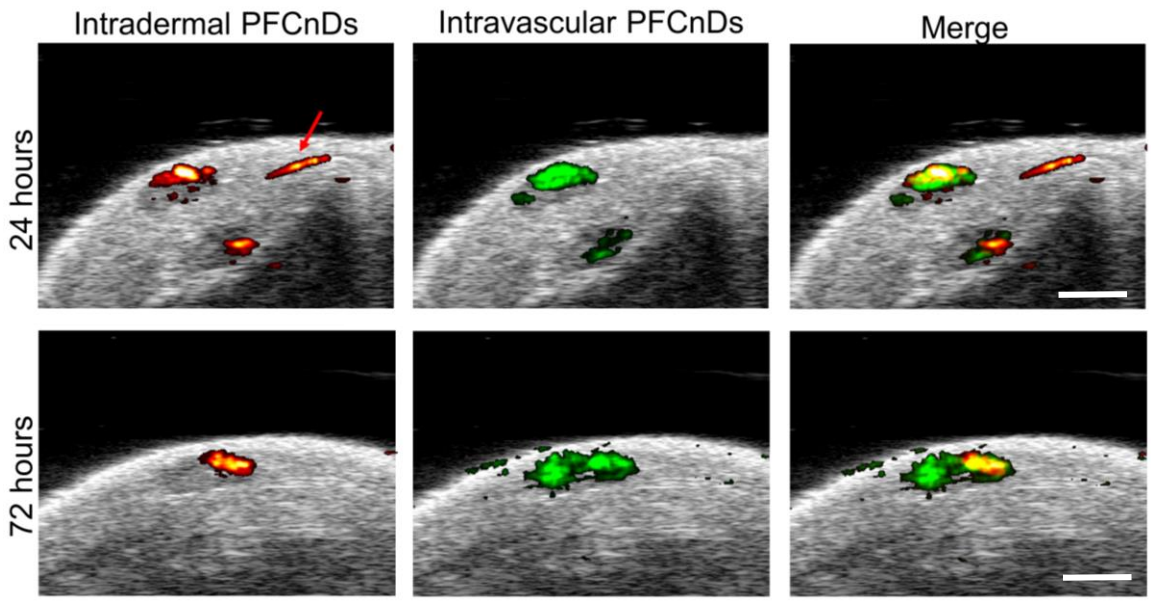


**Figure 16**. Photoacoustic-based processed images showing the different locations of intradermal versus intravenously injected PFCnDs. Red arrow indicates a lymph vessel. The 24 or 72-hour time point refers to the intradermally injected PFCnDs. In both cases, intravascular PFCnDs were injected moments before imaging sessions. Scale bars = 2 mm.

### *4.3.6 Lymphatic trafficking of intradermal injected PFCnDs*

After observing intradermal PFCnD signal much longer than anticipated (days after injections), additional studies were executed to help elucidate their trafficking mechanisms. At 1.5 hours after intradermal injection, USPA imaging showed no accumulation of PFCnDs in the lymph node. However, at 24 and 72 hours, there was the distinct photoacoustic signal arising from vaporization, indicating PFCnD accumulation occurs over these time points. The observed lymph node photoacoustic signal was higher at 24 hours compared to 72 hours (Figure 17a). IVIS imaging at 24 hours confirmed PFCnD presence in the lymph node, but also demonstrated a lot of PFCnDs remain at the injection site (Figure 17b).

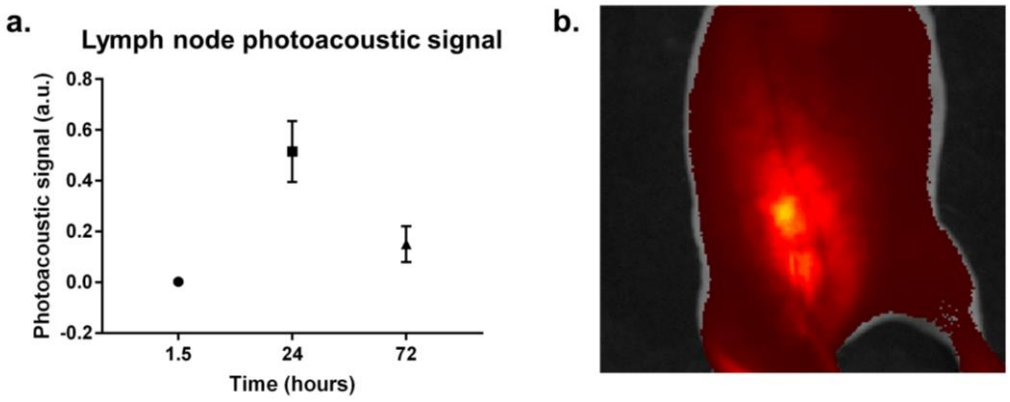


**Figure 17.** (a) Photoacoustic signal of the lymph node at various time points after intradermal PFCnD injection. (b) IVIS image after 24 hours showing the PFCnDs have accumulated in the inguinal lymph node.

### *4.3.7 PFCnD Functionalization*

Successful molecular imaging with targeted PFCnDs was demonstrated. Confocal images showed that HER2 functionalized PFCnDs successfully targeted the HER2 expressing SKBR3 cell line. The control, PEGylated PFCnDs did not attach to SKBR3 cells (Figure 18). These preliminary results show the potential of molecular imaging with functionalized PFCnDs.

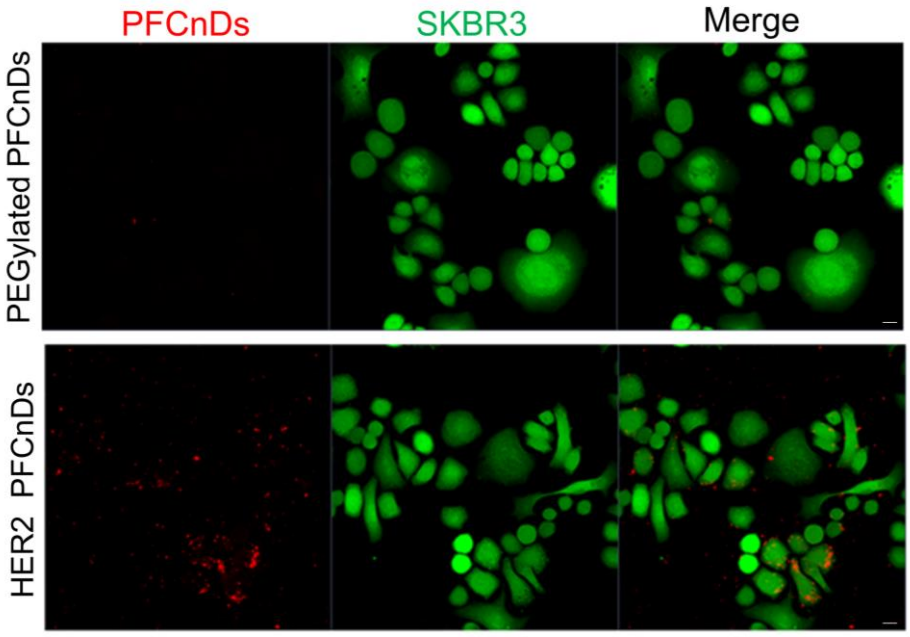


**Figure 18**. HER2 functionalized PFCnDs target SKBR2 cells more effectively. Scale bars = 10 µm.

## 4.5 Discussion

Multicolored PFCnDs bring the diagnostic advantages associated with multiplexed imaging to a clinically relevant imaging modality. Distinct subgroups selectively provide USPA contrast based on laser irradiation wavelength, and the photoacoustic signal is a directly correlated to the concentrations of different subpopulations. Thus far, the platform's utility was demonstrated with two PFCnD subpopulations, but as the development of photoabsorbers with narrow absorption spectra continues, more subpopulations can be added. The advantages of using laser-activated PFCnDs for multiplexed imaging over simple photoacoustic probes are that PFCnDs also provide ultrasound contrast, the ability to deliver increased therapeutic cargos in an image-guided fashion, and their unique contrast allows them to be easily distinguished from endogenous signal to form background-free images.

The developed multicolor PFCnD platform presents an effective method for studying particle dynamics, as experiments can be performed in a single model and imaging session. This allows for a higher throughput, more uniform comparison, and facilitates discoveries. Up until now, many PFCnD studies have focused on synthesis and improving imaging performance, with the majority of these studies conducted in tissue phantoms, *in vitro* or in preliminary *in vivo* models.[48, 57, 78, 103] Additionally, most of the *in vivo* studies focused on short-term applications, on the order of minutes to few hours.[53, 64-65] Given the reported potential of PFCnDs, it is necessary to more thoroughly explore their *in vivo* capabilities. Therefore, multicolored PFCnDs were employed *in vivo* to study murine tumor-draining lymph nodes (TDLNs) and elucidate PFCnD trafficking mechanisms.

As expected, intravenously and intradermally injected PFCnDs reached the TDLN via different mechanisms. Both provide sufficient photoacoustic contrast, at the tested time-points, but only the intravascular exhibits a change in ultrasound contrast. By using the multicolored PFCnD platform, the discrepancies in PFCnD characteristics related to different biological interactions is easily discernable. It was surprising that intradermally injected PFCnDs could remain stable and provide their characteristic photoacoustic signal for up to 72 hours, significantly longer than time frames of previous studies, i.e. typically a few hours. The fact that intradermal PFCnDs no longer provide ultrasound contrast remains to be further studied. However, based on their increased presence in nanodroplet form and the fact they provide photoacoustic but not ultrasound contrast suggests that PFCnDs were taken up by cells.

Further confirming this hypothesis is the location of intradermally injected PFCnDs compared to intravenously injected PFCnDs, while the latter group is present throughout the lymph node, the former is only located in one region of the lymph node. Based on the time scale in which intradermal PFCnDs traffic to the lymph node (Figure 17) and their location within the lymph node, it is likely they are trafficked to TDLNs via cellular-mediated transport.[104-105] Antigen presenting cells (APCs), specifically dendritic cells, have been shown to transport various nanoparticles via afferent lymphatic vessels with similar time-frames to what PFCnDs's exhibit.[91, 105-106] Dendritic cell uptake would also explain why there is no ultrasound contrast. Dendritic cells preferentially uptake smaller particles, and a smaller PFCnD that is vaporized would not provide enhanced ultrasound contrast in MB form.[107 108] Alternatively and/or complimentarily, PFC could diffuse out of PFCnDs

during the 24-72 hour time frame, further reducing the particles size and ability to provide discernable ultrasound contrast. This hypothesis will be confirmed by histology studies.

If confirmed, the fact that intradermally injected PFCnDs traffic to the lymph node via APCs presents advantageous therapeutic opportunities. TDLNs are an important site for immune system regulation, and thus in disease treatment.[109-111] Additionally, dendritic cells are known to have an instrumental role in inducing the adaptive immune system.[112-114] Multicolored PFCnDs could increase therapy delivery by facilitating endosomal escape via the vaporization event. They could also facilitate combination therapies. Different therapeutics could be encapsulated within distinct PFCnD subpopulations, and delivered in a sequential, image-guided manner.

Altogether, multicolored PFCnDs will allow for important *in vivo* diagnostic, monitoring and treatment capabilities. Molecular targeting of PFCnDs was successfully shown *in vitro*. Next steps will involve functionalizing multicolored PFCnDs subpopulations toward various cancer receptors to gain a better understanding of tumor heterogeneity. Compared to the current clinical standard, biopsies followed by pathology, multicolored PFCnDs will increase patient comfort while reducing sampling error, providing a more holistic view of the diseased tissue and any metastatic sites.

# CHAPTER 5. AIM 3: ENHANCING STEM CELL ANGIOGENIC THERAPIES WITH LASER-ACTIVATED PERFLUOROCARBON NANODROPLETS

## 5.1 Introduction

Peripheral arterial disease (PAD) is an ischemic cardiovascular disease that affects around 20% of the elderly population.[115-116] Patients with PAD have a reduced quality of life and increased occurrence of severe cardiac complications.[117-119] If left untreated, PAD can develop into critical limb ischemia, a condition with grimmer prognosis.[116] For patients that have progressed to this stage the most common treatment is surgical intervention; however, due to the inherent risk of the procedures, about 30% of patients are unsuitable for invasive surgery and will face limb amputation or possible death.[120] Thus, it is imperative to develop treatments that are beneficial to even the most refractory patient. One such option is stem cell angiogenic therapy. Stem cells can differentiate into relevant cell types and possess tissue healing paracrine and immunomodulatory effects.[121-122] However, while stem cell angiogenic therapy has shown promise in *in vitro* and pre-clinical models, its progress has been hindered by inefficacy in the clinical setting.[123-124] Until stem cell angiogenic therapy can demonstrate real clinical improvements, it will remain an unrealistic therapeutic option and leave many patients without an appropriate remedy.

There are several reasons for stem cell angiogenic therapy inefficacy.[125-127] One major reason, and the focus of this work, is the high amount of stem cell death following implantation.[125, 128-129] Given the diseased state of the implantation site, it is unsurprising

that the conditions faced by injected stem cells are incredibly hostile. The ischemic tissue is severely hypoxic, nutrient deprived, and has high levels of reactive oxygen species and inflammatory cytokines; factors culminating in the implanted cells quickly undergoing apoptosis.[127-131] It is hypothesized that increasing stem cell survival will result in improved clinical outcomes. As such, researchers have studied various methods to increase cell survival, ranging from pre-conditioning cells to improving the implantation technique and/or stem cell delivery vehicle.[132-135]

The following work focuses on mitigating the severely hypoxic conditions through a controlled oxygen delivery platform. Appropriate oxygen level is essential to stem cell survival as well as functionality.[136-138] Levels of oxygen must be high enough to prevent cell apoptosis, but low enough to initiate important angiogenic signaling pathways, such as the hypoxia-inducible factor (HIF) pathway.[139-141] Researchers have studied preconditioning cells with hypoxic conditions and observed that acclimating the cells to the harsh conditions before abruptly implanting them into ischemic tissue enhanced therapeutic results.[142-144] The goal of this work was to develop an *in vivo* platform that will ease the extent of hypoxia faced by implanted stem cells. Consequently, this will allow implanted cells to better adapt and survive the ischemic conditions and lead to improved therapeutic effects.

The developed platform consists of a hydrogel stem cell delivery vehicle doped with laser-activated PFCnDs. PFC compounds have been extensively used in the medical field as oxygen carriers because they are inert and can solubilize high amounts of gases.[51, 145-146] Due to the nature of PFC oxygen loading and delivery, PFCs do not possess any of the cytotoxic byproducts associated with peroxide-based oxygen delivering

biomaterials.[136, 147] The degree of gas solubility in PFCs follows Henry's law, with higher solubility at increased pressures.[53] Thus, PFCnDs can be synthesized with high oxygen payloads within their highly pressurized, perfluorocarbon liquid core.[8] Additionally, PFCnDs can be triggered to act as photoacoustic and ultrasound contrast agents, providing image-guided oxygen delivery. Encapsulation of a photoabsorber within PFCnDs, followed by pulsed laser irradiation, will cause PFCnDs to undergo a phase change that produces an intense photoacoustic signal and ultrasound enhancement.[4, 34] The platform takes advantage of PFCnDs's oxygen carrying and 'activatable' image contrast characteristics to deliver oxygen via two mechanisms: 1) passive diffusion or 2) activated release via laser irradiation of PFCnDs. The first, passive diffusion, is a function of the PFCnD shell and the surrounding medium's oxygenation.[148-149] Activated release occurs when laser irradiation initiates PFCnD phase-change which compromises the membrane and facilitates escape of encapsulated oxygen. The novelty of the system is the activated release component that allows for on-demand, image-guided release. This feature enables future development of personalized treatment options that can vary based on the patient's ischemic injury severity. To demonstrate the platform's utility, I first investigated the optimal PFCnD loading concentration and confirmed the system's ability to mitigate hypoxic conditions. I further examined the effects of oxygenated PFCnDs on cell viability and on a protein regulated by oxygen availability, intracellular HIF-1α. Lastly, I demonstrated the image-guided release of oxygen in solutions and in hydrogels. As PFCnD technology continues to advance, the designed platform will bring increased control over oxygen delivery; potentially making it a useful method of personalizing treatments and helping bring stem cell angiogenic therapies closer to clinical utility.

## 5.2 Materials and Methods

### *5.2.1 Synthesis and characterization of PFCnDs*

PFCnDs were synthesized with a bovine serum albumin (BSA) shell, similar to previously published work.[4] Briefly, a BSA saline solution (3 mg/ml) was prepared. 200 µl of perfluorocarbon (either perfluoropentane or perfluorohexane) were added to 1 mL of the BSA solution. To make laser-activated PFCnDs, a 1064 nm absorbing dye (Epolight 3072, Epolight Inc.) was added as the photoabsorber. The mixture was briefly vortexed and then sonicated in an ice-cold water bath sonicator (VWR, 180 W) until the solution became milky and no remaining perfluorocarbon bolus was observed. To fabricate oxygenated PFCnDs, the solution of PFCnDs was purged with oxygen (flow rate 2 L/min) for 2 minutes. Following synthesis, a 1:100 dilution of PFCnDs in DI $H_2O$ was prepared and the hydrodynamic size and zeta potential were studied in a Zetasizer Nano ZS (Malvern). A 1:1000 dilution of PFCnDs in DI $H_2O$ was prepared and a Nanosight NS300 (Malvern) used to determine PFCnD concentration.

In studies requiring fluorescently labeled PFCnDs, particles were formed with a lipid shell and lipophilic dye, DiI. Briefly, 3 µl of DiI (3 mg/ml; ThermoFisher) in chloroform was mixed with, 100 µl of the photoabsorber (1 mg/ml, Epolight 3072; Epolight Inc) and 20 µl of 1,2- distearoyl-sn-glycero-3-phosphocholine (DSPC, 10 mg/mL; NanoCS Inc.) lipid in chloroform, and placed in a 50 mL pear shaped flask. A rotovap (Bunchii) was used to evaporate off the chloroform and then 1 mL of PBS was added to rehydrate the lipid cake. 75 µl of perfluorohexane was added and sonicated to produce the droplets.

### *5.2.2 Stem cell culture*

Human adipose stem cells (hASCs) were purchased from Lonza (Walkersville, MD). Cells were cultures in Dulbercco's Modified Eagle Medium (DMEM) (Invitrogen, Carlsbad, CA) supplemented with 10% fetal bovine serum (FBS), 1% glutamax, and 1% penicillin-streptomycin. All cells utilized in subsequent studies were passages 3-7.

### *5.2.3 Fabrication of PFCnD hydrogel scaffolds*

Human fibrinogen was dissolved in PBS (without calcium, pH 7.8) at a concentration of 80 mg/ml. Succinimidyl glutarate-modified polyethylene glycol (PEG; NOF America) was similarly dissolved in DPBS at 8 mg/ml. The two solutions were mixed in a 1:1 volume ratio for 10 minutes to allow for PEGylation of fibrinogen. A specific concentration of PFCnDs in PBS (without calcium, pH 7.8) was prepared (either no nDs, $10^6$ nD/ml, $10^8$ nD/ml, $10^9$ nD/ml, $10^{10}$ nD/ml, or $10^{12}$ nD/ml) and added to the PEG-fibrinogen solution at a 1:1 volume ratio. In cases where hASCs were incorporated into the hydrogel, hASCs were added into the PFCnD-PBS component to have a final concentration of $1\times10^5$ cells/ml. Then, an equal volume of human thrombin (25 U/ml in 40 mM $CaCl_2$) was added for enzymatic crosslinking. The solution was placed in a 5% $CO_2$ incubator at 37°C to complete gelation. After gelation, DMEM media was added. For assays involving hydrogels removal, samples were prepared in well-plate inserts (BD Biosciences) for easy retrieval.

### *5.2.4 PFCnD concentration effect*

Different concentrations of PFCnDs were incorporated into hydrogels to determine their effect on cells. The hydrogels, with incorporated hASCs, were placed in a cell incubator for 48 hours. Cell viability and phenotype were assessed using an MTS proliferation assay and LIVE/DEAD staining, respectively. The MTS assay was performed by incubating phenol-free DMEM media containing 20% MTS solution at 37°C. After three hours, the supernatant was collected and a plate reader (Synergy HT, Biotek) was used to measure the absorbance at 490 nm (n =3). A blank sample's, i.e. no cells, reading was subtracted from all measurements. For LIVE/DEAD staining, an equal volume of the prepared staining solution was added to the hydrogels for one hour. The hydrogels were washed with PBS several times, fixed with 10% formalin, and imaged using a Zeiss LSM 700 confocal microscope.

To study the effect of PFCnD concentration on hydrogel integrity, hydrogels were synthesized with differing PFCnD concentrations (no hASCs incorporated) and placed in a cell incubator. After 48 hours, the hydrogels were removed and individually weighed (n = 3).

### *5.2.5 HIF-1α study*

HIF-1α studies were conducted in 2-D samples to study the influence of oxygenated PFCnDs and minimize the distortion of the additional hypoxia caused by the 3-D hydrogel.[150] HIF-1α levels were compared between normoxic samples and ischemic samples supplemented with or without oxygenated PFCnDs. A cell incubator (Heracell VIOS 160i, ThermoFisher) set at 1% $O_2$, 5% $CO_2$ and DMEM supplemented with 1% FBS

were used to mimic ischemic tissue conditions. A concentration of $1x10^8$ oxygenated PFCnDs/ml was added to the media for the test group. For the normoxic group, cells were placed in an incubator set at 20% $O_2$, 5% $CO_2$ and given DMEM with 10% FBS. hASCs were plated in 6-well plates and placed in the appropriate incubator for six hours. One hour before study completion, a proteasome inhibitor (MG132, Cayman Chemical) was added to minimize HIF-1α degradation. Cells were taken out and placed on ice and were lysed with a RIPA lysis buffer (RIPA, Santa Cruz) to extract HIF-1α. The samples were centrifuged and supernatant collected and used to run a HIF-1α ELISA (Lot#: KQE0414071; R&D Systems). The HIF-1α concentration was normalized to total DNA concentration measured by absorbance at 260 nm (Synergy HT, Biotek).

### *5.2.6 Hypoxia cell viability study*

hASCs were incorporated in PEG-fibrin hydrogels and their corresponding test groups (no PFCnDs, oxygenated-PFCnDs). Groups were placed in normoxic (20% $O_2$, regular media) or ischemic (1% $O_2$, low serum media) conditions for 48 and 72 hours. At the specified time-point, hydrogels were taken out and the cell viability assessed using a LIVE/DEAD stain. Five random areas were imaged from each gel (n = 3) and the ratio of live to dead cells quantified using ImageJ.

### *5.2.7 Oxygenation-lasing and imaging study*

A sealed chamber was used for simultaneously measuring a solution's oxygen levels and obtaining photoacoustic data. The front face of the chamber had an optical window to allow for laser irradiation of the samples. The chamber had one inlet on the side to allow for nitrogen purging of the solution. Two additional inlets on the top, with rubber stoppers in

them, were designed to tightly introduce the oxygen probe or the sample. The oxygen probe (NeoFox; Ocean Optics) was pierced through the rubber stopper and its tip placed in the headspace of the container. The other rubber stopper allowed for sample introduction. On one side of the chamber, a space was machined out and a 20 MHz transducer was placed in and sealed with silicone. This allowed for photoacoustic imaging with the Vevo imaging system (VisualSonics). 30 mls of DI $H_2O$ were added into the chamber and purged with $N_2$. A stir bar was placed in the chamber for mixing throughout the experiment. After several minutes, oxygen measurements verified that $O_2$ was sufficiently low and the $N_2$ supply was stopped and the chamber sealed shut. Before starting the experiment, oxygen levels were allowed to reach a stable reading. 900 µl of oxygenated-PFCnDs were introduced into the chamber and the recording of oxygen partial pressure ($ppO_2$) levels and photoacoustic data started. At one minute, the sample was irradiated with a 10 Hz pulsed laser at 1064 nm and a fluence of 50 $mJ/cm^2$ (Vibrant, Opotek). After 15 seconds the laser was turned off. Recording of $ppO_2$ and photoacoustic data was stopped after a total time of two minutes. The same parameters were used for the control group, DI $H_2O$.

### *5.2.8 Imaging of activation event within hydrogel*

In addition to imaging the release of oxygen from PFCnDs in solutions, the ability to activate and image PFCnDs (perfluorohexane core) within a hydrogel was studied. The hydrogel was synthesized with one region containing PFCnDs with a photoabsorber and the other section had PFCnDs with no photoabsorber. A hydrogel region with both sample types was irradiated with 1064 nm, 10 Hz pulsed laser light at 40 $mJ/cm^2$ (Vibrant, Opotek) and imaged with a 20 MHz transducer and VEVO imaging system. The collected data was

processed to identify and highlight the locations of activated PFCnDs according to a previously described algorithm.[47]

### *5.2.9 Activation event on gel structure and ASC viability and gel structure*

The effect of activating PFCnDs on stem cells and hydrogel properties was studied with lipid shelled PFCnDs and an incorporated lipophilic fluorescent dye. The fluorophore, DiI, allowed for studying the PFCnD dynamics post-irradiation. Three µLs of DiI (3 mg/mL; ThermoFisher) in chloroform was mixed with, 100 µLs of the photoabsorber (1 mg/mL, Epolight 3072; Epolin Inc.) and 20 µLs of 1,2- distearoyl-sn-glycero-3-phosphocholine (DSPC, 10 mg/mL; NanoCS Inc.) lipid in chloroform, and placed in a 50 mL pear shaped flask. A rotovap (Bunchii) was used to evaporate off the chloroform and then 1 mL of PBS was added to rehydrate the lipid cake. A volume of 75 µLs of perfluorohexane was added and sonicated to produce the droplets. Hydrogels were synthesized with incorporated cells and PFCnDs and then placed in a cell incubator. After 24 hours, samples were taken out and irradiated with 1064 nm pulsed laser at an energy of 40 mJ/cm2 (Opotek Vibrant) for 30 seconds. Samples were replaced with new media and put in a cell incubator. For qualitative analysis, LIVE/DEAD staining was performed at 24 and 48 hours post-lasing. Samples were taken out and stained with LIVE/DEAD stain. The gels were fixed with 10% formalin and then imaged on a Zeiss 700 confocal microscope. For quantitative comparison, MTS assays (n=4) were conducted at 24 and 48 hours after lasing as previously described.

### *5.2.10 Statistical Analysis*

All data is presented as mean +/- standard deviation. Statistical significance was calculated by performing a one-way ANOVA analysis, followed by Tukey's multiple comparison in GraphPad Prism 7.

## 5.3 **Results**

### *5.3.1 PFCnD characterization*

A PFCnD emulsion were formed after sonication of the PFC, BSA and PBS mixture. The zeta potential of PFCnDs was -30.3 mV, indicating the colloidal stability. The hydrodynamic size of PFCnDs was measured to be approximately 400 nm (Figure 19a).

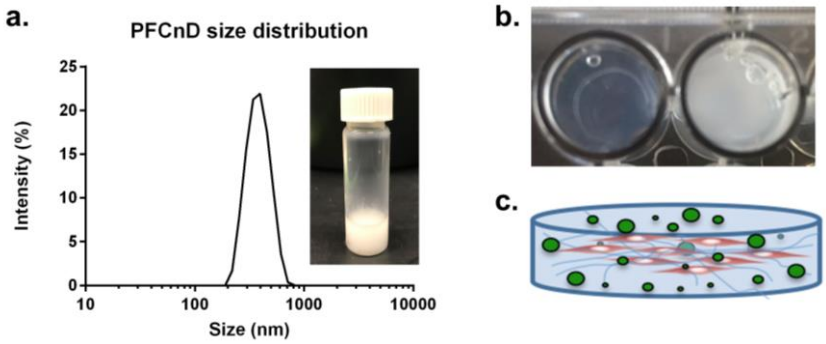


**Figure 19.** (a) PFCnD size distribution was measured by DLS and found to be 400 nm. The insert shows the PFCnD emulsion following sonication. (b) A PEGylated fibrin hydrogel with and without incorporated PFCnDs. Incorporation of PFCnDs makes the gels less transparent but at the appropriate concentration does not affect hydrogel properties. (c) Schematic of the hydrogel with PFCnDs (green) and stem cells incorporated.

### *5.3.2 Optimal PFCnD concentration*

Incorporation of PFCnDs into the typically transparent PEGylated fibrin hydrogel turned it more opaque (Figure 19b). Increasing PFCnD concentration past $10^9$ nDs/mL began led to faster hydrogel degradation (Figure 20a). Interestingly, the increased PFCnD concentration did not negatively impact cell viability. Instead, MTS results indicated that as the gel degraded, cells proliferated at an increased rate (Figure 20b). Increased cell proliferation was a result of cells falling out of the degrading gel and growing on the preferred 2-D surface. Cells located within the gels exhibited similar phenotypes across all

concentrations (Figure 20c-h). It should be noted that the cells imaged at the $1x10^{12}$ nD/mL were located within a part of the hydrogel that remained structurally intact. A concentration of $1x10^{9}$ nDs/mls was used for subsequent studies as it did not impact gel integrity or cell phenotype or viability.

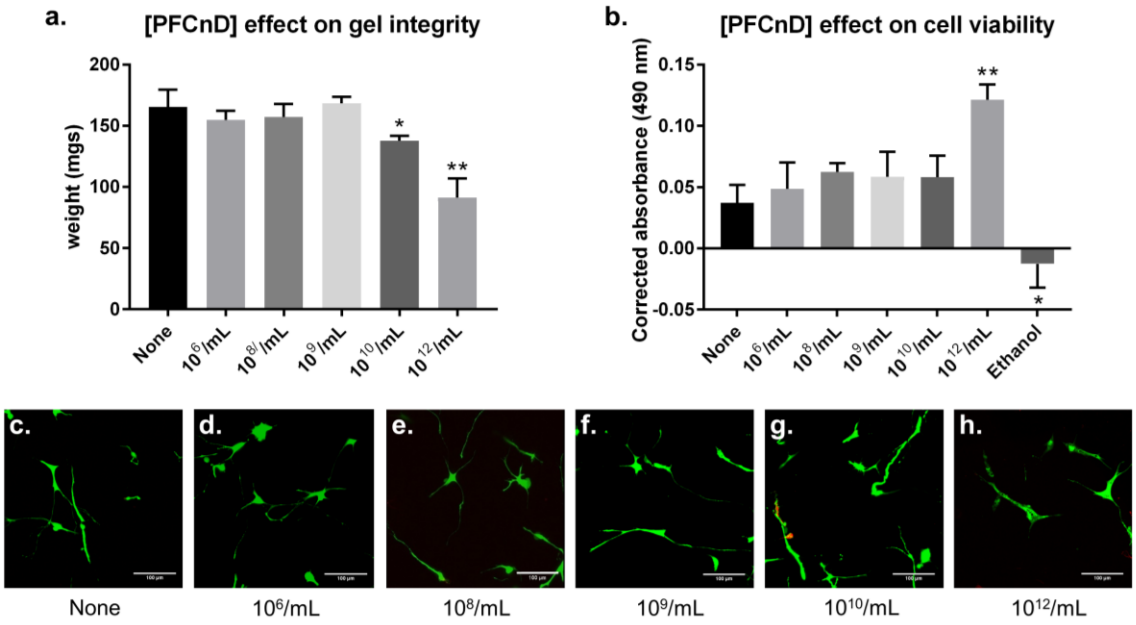


**Figure 20.** Effect of PFCnD concentration on gel integrity and cells. (a) At PFCnD concentrations above $10^9$nDs/mL the gel began to significantly degrade. (b) There is no negative effect of increasing PFCnD concentration on cell viability and proliferation. However, at the highest concentration many cells are growing on the 2-D surface instead of within the hydrogel, leading to the increased proliferation. (c-h) Cells imaged within the hydrogel are able to spread and exhibit the typical phenotype regardless of PFCnD concentration, minimal cell death was observed at all concentrations (LIVE/DEAD staining).

### *5.3.3 Oxygenated-PFCnD influence on stem cells under hypoxia*

Cells cultured in ischemic conditions had significantly elevated levels of HIF-1α. However, in the ischemic group containing oxygenated-PFCnDs, HIF-1α expression was comparable to cells cultured in normoxia (Figure 21a) and significantly lower than cells cultured without oxygenated-PFCnDs. This demonstrates that PFCnDs can deliver enough oxygen to regulate HIF-1α degradation, resulting in a reduced expression.

Oxygenated PFCnDs can influence cell viability for at least 3 days. At 48 hours there was no significant difference in cell viability amongst the three groups. However, at 72 hours the hypoxia group with no PFCnDs had significantly reduced cell viability, while the oxygenated-PFCnDs retained similar viability to cells in normoxic conditions (Figure 21b).

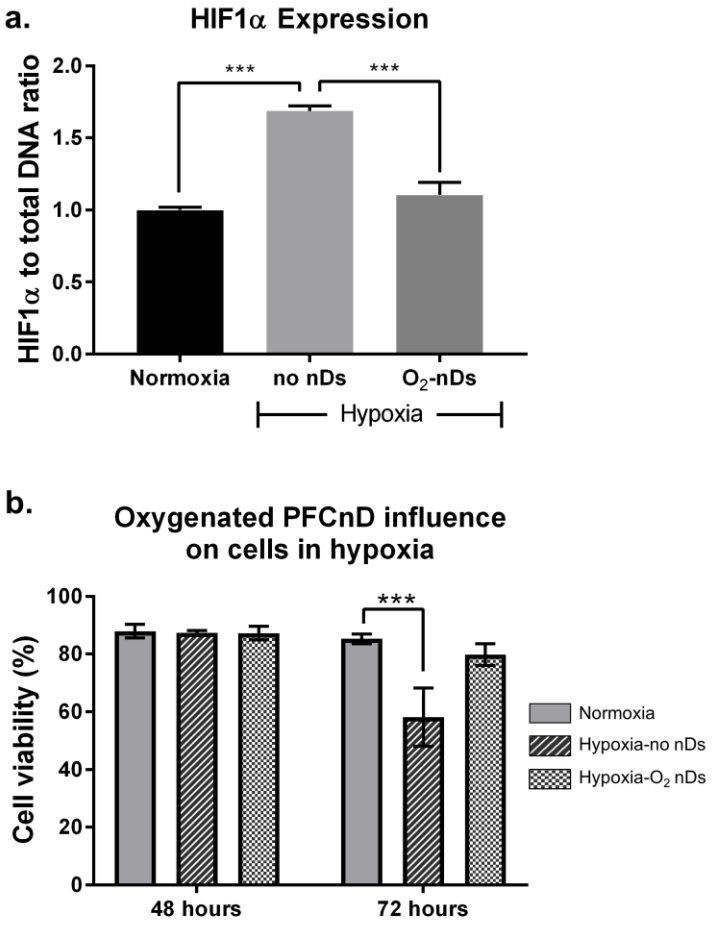


**Figure 21.** (a) Inclusion of oxygenated-PFCnDs ($O_2$-nDs) results in lower HIF-1α levels which are similar to expression seen in cells cultured in normoxic conditions. Cells cultured in hypoxia with no PFCnDs had significantly elevated levels of HIF-1α compared to both normoxia and the $O_2$-PFCnD group at 6 hours. (b) For cells are cultured in ischemic conditions, $O_2$-PFCnDs significantly improve viability over cells without PFCnDs for up to 72 hours.

### *5.3.4 Activated oxygen release*

In addition to passive oxygen diffusion, increased payloads of oxygen can be delivered via laser irradiation of PFCnDs. The inclusion of oxygenated PFCnDs increased $ppO_2$ immediately, indicating the occurrence of passive oxygen release (Figure 22b). Upon laser irradiation, there was an immediate increase in photoacoustic signal (Figure 22b,d). Shortly after, $ppO_2$ increased by 5% (Figure 22b). When lasing was stopped, oxygen levels fell to a level slightly higher than before lasing and continued to gradually rise as before. This could be a factor of the sealed chamber not being as gas-tight as originally thought.

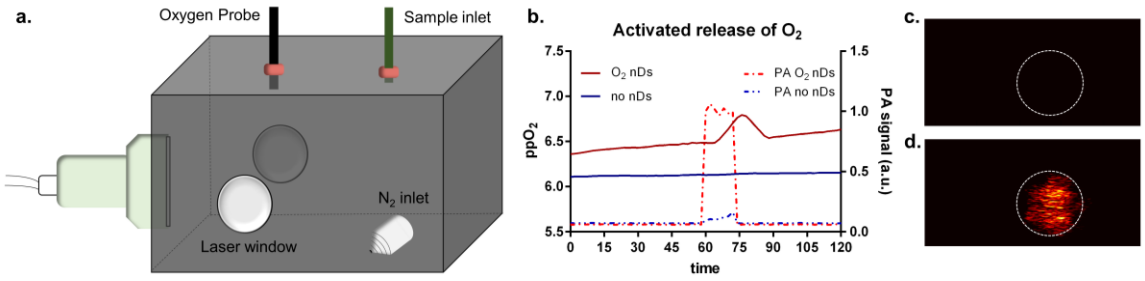


**Figure 22.** (a) Experimental set-up for measuring $ppO_2$ levels and capturing photoacoustic data. b. Upon lasing, oxygenated-PFCnDs oxygen levels increase, accompanied by a stark increase in photoacoustic signal. (c,d) The photoacoustic signal upon laser irradiation is clearly evident compared to no laser irradiation.

### *5.3.5 Image-guided activation effects*

Different subsets of PFCnDs can be selectively activated and imaged to show the locations of activation. Laser irradiation of a hydrogel, no cells, containing either blank or photoabsorber-loaded PFCnDs causes activation only in the region containing the photoabsorber-loaded PFCnDs. The collected data can be image processed to clearly indicate regions of PFCnD activation (Figure 23a).

When cells are included within the hydrogels, PFCnD activation and the subsequent expansion did not cause cell death in the short-term. Laser irradiation of PFCnD loaded hydrogels altered the gel's structure creating a spongy effect in regions that had been irradiated. However, at 24 hours, MTS results showed that all groups had similar numbers of viable cells. Additionally, LIVE/DEAD staining confirmed there were many viable cells that were growing around the expanding cavities of the hydrogel (Figure 23b). At 48 hours, confocal images showed that the created pore's size increased as more gas diffused into the cavities. MTS results indicated that the activated group had slightly lower, but insignificantly different cell viability and proliferation. The extent of PFCnD activation on cell viability is affected by the concentration of PFCnDs within the hydrogel. At higher concentrations, $1x10^{10}$ nD/mL, there are more created cavities which significantly hinders cell proliferation at 48 hours relative to the control (Figure 23e).

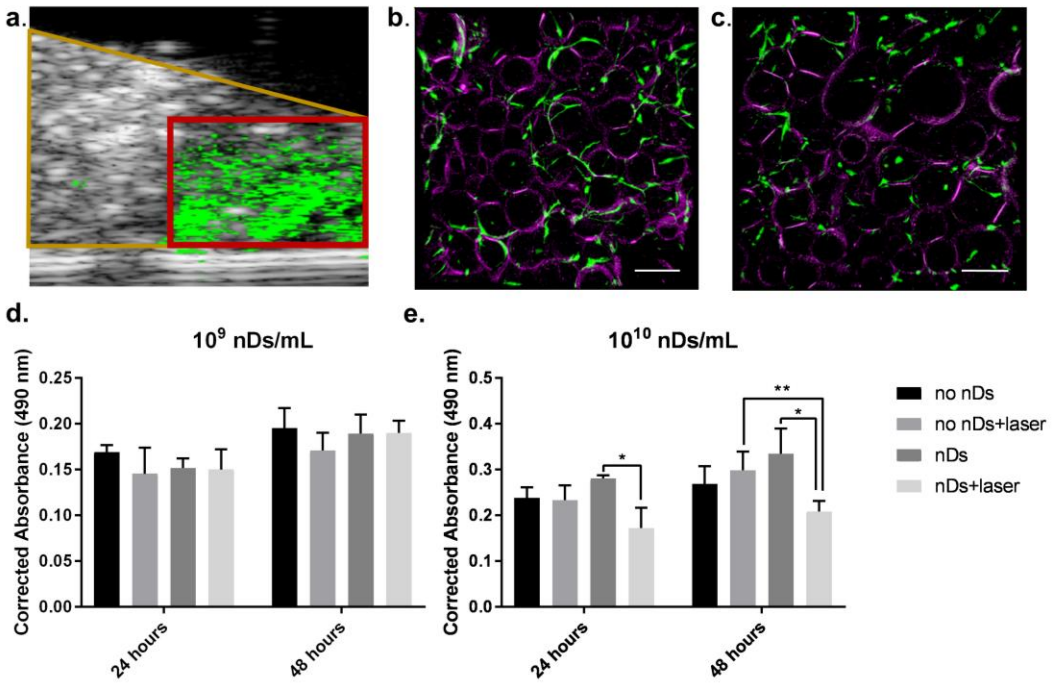


**Figure 23**. (a) Image-processed ultrasound data of a hydrogel depicting how PFCnD activation can be controlled to one region. Red outline indicated the gel region with PFCnDs containing a photoabsorber, while the area to the left contains PFCnDs with no photoabsorber. (b) 24 and (c) 48 hours after laser irradiation cavities are created (purple dye is DiI present in the PFCnD shell). The cells remain viable and continue to spread at 24 hours, but are more limited by 48 hours (LIVE/DEAD stain). (d,e) The concentration of PFCnDs effects cell proliferation after lasing due to the higher amount created cavities. Scale bar= 200 µm.

## 5.4 Discussion

Laser-activated PFCnDs present a unique method of improving stem cell angiogenic therapy efficacy. PFC-based particles have been studied in different biomaterial based applications to improve therapeutic outcomes because of their superior oxygen solubility and delivery.[139, 151] Here, I demonstrate that in addition to PFCnDs passively influencing oxygen levels, they can release oxygen in an on-demand, image-guided process. The innovative platform uses laser-activated PFCnDs to control and localize oxygen release.

At appropriate concentrations, PFCnD incorporation into the stem cell delivery vehicle did not affect cell viability. No cell toxicity was observed at any of the concentrations tested; likely in part a result of using a protein emulsifier versus another surfactant.[152] While high PFCnD concentrations did not impact cell viability, concentrations above $10^9$ nDs/mL did affect the hydrogel's mechanical properties. This is partly due to the high concentration of emulsifier associated with increased PFCnD incorporation, compromising the integrity of the hydrogel and leading to faster degradation.[153] Additionally, the high density of PFC, two times denser than water, combined with their high concentration could be too much weight for the hydrogel to bear, resulting in mechanical damage over time.[63] Hence, while higher concentrations of PFCnDs would be beneficial for carrying increased oxygen payloads, there is a threshold beyond which premature hydrogel degradation would occur and negatively impact cell engraftment.

PFCnDs are effective at delivering oxygen and reducing the extent of hypoxia experienced by newly implanted stem cells. Cells cultured in 1% oxygen, but supplemented with oxygenated PFCnDs, demonstrate comparable HIF-1α levels to cells cultured in normoxia. HIF-1α is an important transcription factor related to cell survival and angiogenic response. Its levels are inversely related to the amount of oxygen available, as it is degraded through a process dependent on oxygen.[154] Since HIF-1α levels peak at six hours following hypoxia exposure,[155] this represents an ideal time-point for studying PFCnDs's short-term influence. At this time point, oxygenated PFCnDs brought HIF-1α levels similar to cells cultured in normoxia. Additionally, oxygenated-PFCnDs have an impact on cell viability for up to 72 hours, which is in line with what others have observed.[153] While the ideal scenario would be to have sustained oxygen delivery until blood vessel in-growth occurs (typically around day 14), [63, 136] the fact that the designed system can mitigate the hypoxia experienced by newly implanted cells and give them time to adjust, could have drastic implications on overall angiogenic efficacy. Another aspect to consider is the delicate balance between too much oxygen, which prevents production of angiogenic factors, and too little oxygen, which leads to stem cell death and limits therapeutic outcome.[144, 156] To improve therapeutic outcome, stem cells must express some levels of HIF-1α in order to better survive, upregulate angiogenic factors, and exhibit their paracrine effects.[135, 140] Considering that PFCnDs influence HIF-1α short-term (6 hours) and increase viability for up to 72 hours suggests that they can minimize apoptosis, while still promoting their angiogenic response over time. Speculating, it is possible that oxygenated PFCnDs could help condition newly implanted stem cells *in situ*, in a manner

similar to how *in vitro* pre-hypoxia conditioning works.[142] In the future this must be tested with *in vivo* ischemic models.

The capability of PFCnDs to release increased amounts of oxygen upon laser irradiation, and to localize the oxygen's release with photoacoustic imaging augments the potential of previously studied perfluorocarbon-based oxygen delivery biomaterials (extensively reviewed in Farris *et al.*[136]). Additionally, the same photoacoustic and ultrasound imaging system needed to activate and visualize PFCnDs can be used to elucidate which tissues are severely hypoxic by studying deoxygenated and oxygenated hemoglobin levels.[26, 65] With this knowledge, PFCnDs located in more hypoxic regions can be irradiated and release oxygen in areas of greater need. Hence, the developed system can help provide patient-specific treatments for increased efficacy. Currently, this idea is limited by the extensive passive release of oxygen from PFCnDs. The development of shells that reduce permeability may help retain oxygen within the core and allow for better control of its release upon laser irradiation.[63]

Laser irradiation of PFCnDs within hydrogels does not result in cell apoptosis, but does alter the material properties over time. *Fabilli et al.* characterized a similar system and observed comparable phenomena.[11, 157-158] Their system involves PFCnD-doped hydrogels; however, instead of laser-activation of PFCnDs they employ acoustic-activation. This type of activation involves irradiating samples with peak rarefactional pressures (negative pressures) at a threshold that induces vaporization of PFCnDs.[5, 157] At large enough negative pressures, acoustic activation can cause inertial cavitation of the PFCnDs and result in cell apoptosis.[11] In contrast, the laser-activated PFCnD system did not result in any cell apoptosis (Figure 23d), suggesting that laser-activation successfully

induces phase change, but likely does not cause inertial cavitation. Similar to laser-activated PFCnD data, acoustic vaporization of PFCnD results in bubble formation in the hydrogel, and the created bubbles grow over time.[158] Given the results of the created cavities surrounded by the lipid used in PFCnD synthesis, it is possible that the repeated expansion of the PFCnDs during laser irradiation deforms the hydrogel and produces a negative pressure in the PFCnDs's vicinity. The resulting negative pressure alters the interfacial tension and stability of the PFCnDs causing them to transition into bubbles that gradually expand as dissolved gas diffuses into the PFC bubbles, because of their high gas solubility.[51, 159] Fortunately, this phenomenon does not impact cell viability at the time points tested and with the appropriate PFCnD concentration ($10^9$ nDs/mL). However, at higher concentrations ($10^{10}$ nDs/mL) cell proliferation was significantly reduced at 48 hours. Given the time point at which cells are impacted, it is likely the expansion of the bubbles, not the activation, is what causes reduced cell proliferation. However, this effect might be mitigated *in vivo* where immune cell infiltration and clearance of PFC are at play.[59, 160] Interestingly, previous studies showed creation of these bubbles enhanced blood vessel in-growth *in vivo*.[161]

# CHAPTER 6. CONCLUSIONS AND FUTURE DIRECTIONS

## 6.1 Laser-activated PFCnDs as diagnostics

### *6.1.1 Conclusion Aim 1: CuS-PFCnDs enhanced*

The unique combination of CuS NPs and PFCnDs helps to overcome current laser-activated PFCnD limitations. By using CuS NPs, which optically absorb in the second optical window, as the photoabsorber that initiates the phase-change, PFCnDs can be activated to provide contrast at increased penetration depths. Unlike other metallic particles that optically absorb in this region, CuS NPs have been shown to be biodegradable, and can be synthesized at small sizes for renal clearance, increasing their biocompatibility over comparable photoabsorbers.[76] Considering that the long-term biocompatibility is a significant issue in assessing clinical feasibility, CuS NPs could facilitate laser-activated PFCnDs's chances of overcoming this hurdle.

### *6.1.2 Future Directions: CuS-PFCnDs*

#### 6.1.2.1 Understanding laser-activated vaporization dynamics

Up until now, the exact dynamics of laser-activated PFCnD phase vaporization are not well characterized. In acoustically-activated PFCnDs there have been studies showing vaporized PFCnDs becoming a stable MB, and others showing that first they over-expand, oscillating towards a stable size.[39] Similarly, laser-activated PFCnDs might exhibit different behaviours based on the photoabsorber or PFC core. A better understanding of the particle dynamics can allow for improved image processing techniques.

Another area to investigate is the potential of laser-activated release to cause inertial cavitation. As of now, the majority of conducted studies result in a stable or transient microbubble, but do not cause microbubble collapse, i.e. inertial cavitation. In acoustically activated PFCnDs, acoustic parameters can be altered to cause stable or inertial cavitation.[11] As these each have different biological effects, understanding how to exploit both mechanisms would be helpful in future development of laser-activated PFCnDs as therapeutics.

#### 6.1.2.2 Increasing extravasation

The first area CuS-PFCnDs could have an impact on is as diagnostic agents. CuS-PFCnDs's increased imaging depth over comparable laser-activated PFCnDs expands their diagnostic abilities to deeper tissues. Upon appropriate functionalization, CuS-PFCnDs could act as effective diagnostic agents for vascular markers. However, if they are to be effective extravascular diagnostic agents, then they must be able to extravasate to the needed degree, a challenge facing all NPs. NP extravasation studies have shown that a very small amount (~1% of injected dose) is able to enter into solid tumors.[45] Reducing the size and stealth (i.e. ability to evade RES system) of CuS-PFCnDs could improve extravasation. Using *in vivo* cancer models will help elucidate if meaningful amounts of CuS-PFCnDs can extravasate.

#### 6.1.2.3 Development of CuS-PFCnDs as therapeutic agents

CuS NPs photothermal stability makes them well suited for photothermal therapy (PTT).[75] PTT works by elevating the temperature of cancerous cells to levels that induce apoptosis. To accomplish this, a continuous wave laser tuned to the photoabsorber's

absorption wavelength irradiates a tissue of interest and creates a localized temperature increase. The benefit of PTT is that it is very selective, only occurring at the irradiated tissue, and much more concentrated in areas containing photoabsorbers. Additionally, cancer cells have a reduced heat tolerance, making them more susceptible to PTT.[162] In order for PTT to be effective, there needs to be increased concentrations of CuS NPs in the lesion combined with adequate laser exposure.[75] Hence the previously mentioned extravasation limitation will be a limiting factor in achieving effective PTT. However, conversion of CuS-PFCnDs into microbubbles, followed by high intensity ultrasound to cause inertial cavitation, could aid in increasing levels of CuS NPs delivery into the tumor. Previous work using CuS-MB have looked at achieving a similar effect, but have not yet demonstrated success *in vivo*.[163]

### *6.1.3 Conclusion Aim 2: Multiplexed imaging with multicolored PFCnDs*

The developed multicolored laser-activated PFCnD platform has potential in both diagnostic and therapeutic applications. In diagnostics, multiplexing capabilities are increasingly being investigated, particularly in cancer applications.[98] Considering that biological specimens are often multifaceted, the ability for a diagnostic agent to convey the intricacies over a single modality will greatly impact diagnosis efficacy and efficiency. For instance, in breast cancers there are several subtypes, each with differing prognosis and treatment options. One of the most influential factors in deciding the course of treatment is that type or receptors present, i.e. hormone-positive/-negative and/or HER2-positive/-negative.[164] Additionally complicating the situation is that there are intratumor and intertumor (if metastasis has occurred) heterogeneities, and the fact that cell populations may change over the course of treatment.[40] Currently, biopsies followed by an *in vitro* assay (ex: Immunohistochemistry or *in situ* hybridization) are used to guide treatment.[164] If multicolored PFCnDs can successfully reach their target, they would present a non-invasive manner of conveying the necessary comprehensive pathological information, and because there is no ionizing radiation, they could also monitor therapeutic progress as repetitive imaging is not a concern.

Studies using multicolored PFCnDs helped uncover that intradermal PFCnDs can successfully traffic to the lymph nodes and persist for several days, greatly increasing their potential therapeutic applications. Previous studies have only investigated short-term applications of PFCnDs. A better understanding of their stability and lifetime *in vivo* will lead to improved therapies. For instance, exhaustive and targeted treatments can be administered with a single dose of multicolored PFCnD, where each subpopulation carries

distinct therapeutics and releases them in a sequential, image-guided manner. One area that could benefit from this is next generation immunotherapies that are looking at combinations of therapeutics.[165-166] One PFCnD subpopulation could be loaded with a targeted drug and another with an inhibitor, then laser-irradiation of the respective groups would allow for localized release.

Overall, the described work advances PFCnD technology and establishes these particles as comprehensive diagnostic and therapeutic agents, but future work is crucial in demonstrating them as next generation diagnostic and therapeutic agents.

### *6.1.4 Future Directions: Multiplexed PFCnDs*

#### 6.1.4.1 Increase subpopulations of PFCnDs

With the development of narrower absorption peak photoabsorbers, increased numbers of PFCnDs subpopulations can be synthesized for improved multiplexing capabilities. This will be of particular importance in cancers with various subtypes, i.e. breast cancer, where subtype dictates the needed treatment.[167] Appropriate phantom studies should be conducted to demonstrate selective PFCnD activation and USPA response.

#### 6.1.4.2 Show ability to differentiate between different cell populations *in vitro*

The ability of multicolored PFCnDs to detect different cancer subtypes should be demonstrated *in vitro*. This can be done by culturing different breast cancer cell lines at varying ratios, and adding equal amounts of differently functionalized PFCnDs (anti-HER2, anti-ER, anti-EGFR, etc.) to the cells. After allowing for PFCnD-cell receptor interaction, the cells would be detached and fixed. Cell inclusion phantoms would be able

to demonstrate if photoacoustic signal at subpopulation wavelengths correlate to cultured cell ratios.

#### 6.1.4.3 Diagnosis of solid tumors

As with CuS-PFCnDs, multicolored PFCnDs must be able to enter into solid tumors to successfully diagnose cancer subtype. Systemic and intratumor injections should both be studied and their diagnostic potential assessed. In the case of intratumor injections, multicolored PFCnDs would be beneficial because one of the subpopulations can be used as a baseline indicator to normalize signal for other subpopulations. This would help reduce any off-target associated signals that arise due to PFCnD retention at the injection site. For systemic injections, improving extravasation will be key.

#### 6.1.4.4 Increasing extravasation of PFCnDs

Multicolored nanodroplets could help overcome the hurdles associated with extravasation and penetration of NPs into solid tumors. One subpopulation of multicolored PFCnDs could be targeted to tumor endothelium (e.g. VEGFR-2). Upon phase-change, the pressure waves created by the vaporization event could increase vascular permeability. If needed, ultrasound could be applied to the produced microbubbles to further increase acoustic radiation forces and vascular permeability.[163, 168] This would allow the other subpopulations to more readily enter into the tumor. Upon entry, laser-triggering of another PFCnD subpopulation in conjunction with ultrasound could be used to cause stable cavitation that increases tumor ECM permeability to facilitate penetration of the remaining PFCnDs. This pattern could be continued based on the amount of PFCnD subpopulations

available. The result would be more extensive tumor infiltration, which would improve current diagnostic and therapeutic outcomes.

#### 6.1.4.5 Sentinel lymph node detection

The conducted lymph node studies indicated that PFCnDs traffic to tumor draining lymph nodes via cell-mediated trafficking. This is both advantageous and problematic. It could be problematic if PFCnDs are expected to diagnose metastatic sites, since they will not be able to interact with cancer cells from inside APCs. Studies with reduced PFCnD size, and increased stealth properties should be studied to determine their lymphatic trafficking mechanisms and ability to directly interact with cancerous cells at these sites.

#### 6.1.4.6 Multicolored PFCnDs as companion diagnostics

If the aforementioned diagnostic hurdles are overcome, multicolored PFCnDs could serve as a companion diagnostic to predict a patient's response to therapy and/or monitor their response overtime. The Food and Drug Administration (FDA) defines companion diagnostics as a "device or imaging tool that provides information that is essential for the safe and effective use of a corresponding therapeutic product."[169] Currently, there are over 30 companion diagnostics, but only one of them is an imaging tool (MRI based); the rest are *in vitro* tests.[169-170] Given the low-cost, and safety (non-ionizing radiation) of USPA, multicolored PFCnDs would be an attractive imaging tool for use as a companion diagnostic. Functionalized multicolored PFCnDs could noninvasively convey information regarding cancer receptor presence to dictate the appropriate treatment. Multicolored PFCnDs could also be used to monitor a patient's response and adjust

treatment as needed.[171] This is particularly useful given that tumor cell populations can evolve overtime as some cells become resistant to therapies[172]

## 6.2 Laser-activated PFCnDs as image-guided oxygen therapeutics

### *6.2.1 Conclusion Aim 3*

Laser-activated PFCnDs advance the use of perfluorocarbon-doped hydrogels through image-guided oxygen release. Upon laser irradiation the PFCnDs undergo a phase-change, which compromises the shell membrane and causes increased oxygen release. This event can be localized with ultrasound and/or photoacoustic imaging techniques to show where higher payloads of oxygen were delivered. In addition, laser-activated PFCnDs, like its predecessors, can passively deliver sufficient levels of oxygen to alleviate the hypoxic implantation site and mitigate cell apoptosis. *In vitro* studies demonstrate that oxygenated PFCnDs reduce hypoxic protein expression and increase cell viability short-term, demonstrating their potential to mitigate the sudden hypoxia experienced by cells post-implantation. As PFC-based technologies continue to advance, the presented platform could be used for tailoring stem cell angiogenic therapies for increased efficacy.

### *6.2.2 Future Work*

#### 6.2.2.1 Increase control of oxygen delivery

One significant limitation of PFCnDs for oxygen delivery is the lack of control due to extensive passive release. Oxygen release out of oxygen-permeable PFCnD shells is dictated by Henry's law, i.e. dependent on partial pressure of oxygen. Therefore, when oxygenated PFCnDs are introduced to a hypoxic environment, the carried oxygen will immediately begin to be diffuse out of the PFCnDs core.[149] Groups have engineered shells with increased rigidity and stability to limit oxygen diffusion, but still observed rapid

release of oxygen when PFCps are placed in hypoxic conditions.[173] Although the diffusion rate is reduced in the hydrogel environment, compared to liquid, it still occurs faster than preferred.[174]

One clear benefit of externally-triggering oxygen release is there is no dependence on shells to exhibit any degree of oxygen permeability. This is in contrast to many groups who try to minimize passive diffusion, but must still rely on it to increase oxygen levels overtime.[63] Thus, thicker, denser shells that significantly impede oxygen release can be employed for laser-triggered PFCnDs. The only requirement is that laser-activated vaporization must still be able to occur. Studies focused on the aforementioned shell parameters would greatly impact laser-activated PFCnDs's role in controlling oxygen delivery.

#### 6.2.2.2 Show efficacy in *in vitro* ischemic models

PFCnDs have shown the ability to alleviate hypoxic conditions short-term, i.e. up to 3 days. The extent of current PFCnD-based oxygen delivery may be enough to act analogously to pre-conditioning cells with hypoxia, particularly considering when cells pre-conditioned with hypoxia for only 24 hours exhibited beneficial tissue healing effects *in vivo*.[132] One advantage of using PFCnDs to alleviate hypoxia for cells *in situ*, is the reduction in time needed prior to cell implantation, i.e. no reliance on cell treatments beforehand. The impact of the described short-term benefits could be further complemented *in vivo*, where other cells, such as macrophages, contribute to tissue regeneration and remodelling.[175] An *in vivo* hind limb ischemia model will help verify the suspected impact oxygenated PFCnDs can have in stem cell angiogenic therapies.

#### 6.2.2.3 Post-PFCnD activation events on tissue in growth and stem cell fate

Activation of PFCnDs within the hydrogel resulted in bubble formation which grew overtime, creating a sponge-like hydrogel. *Fabilli et. al.* demonstrated that acoustically activated PFCnD doped gels underwent the same hydrogel deformations seen with our model. Interestingly, in *in vivo* models they observed higher vessel in-growth in hydrogels that exhibited the sponge-like effect compared to controls. It is hypothesized that inclusion of PFCnDs increases oxygen, and the ability of cells to invade the hydrogel, which subsequently led to increased vessel in-growth.[161] Considering that these studies did not include highly oxygenated-PFCnDs, further beneficial effects on blood vessel in-growth could be seen by incorporating this type of PFCnD. Once again, *in vivo* studies will help confirm this hypothesis.

In addition to a passive influence, the creation of bubbles within the hydrogel can be externally manipulated to alter stem cell fate. It is well established that stem cells respond to environmental cues in the form of both chemical and physical stimuli.[176] After laser-triggered activation has produced bubbles within the hydrogel, ultrasound can be administered to oscillate the created bubbles, thereby exerting forces (tensile and compressive) onto surrounding cells. The impact of these forces in directing stem cell differentiation should be studied in controlled, *in vitro* models.

#### 6.2.2.4 Oxygen delivery in cancer applications

Apart from stem cell angiogenic therapies, the developed technology could not only be relevant for other stem cell therapies, but also for cancer applications. Increased tumor hypoxia is correlated with tumor progression, malignancy and resistance to therapy.[177]

Reducing hypoxia, through oxygen delivery to tumor sites, can increase susceptibility of cancer cells to radiation-based therapy.[65] Light-triggered PFCnDs would be particularly advantageous for these applications due to the platform's use of photoacoustic imaging which can simultaneously assess tissue hypoxia and localize oxygen release of PFCnDs.

## 6.3 Overall Conclusion and Future Outlook

The accomplished work successfully bridged some of the current gaps associated with laser-activated PFCnDs, better positioning them as attractive diagnostic and therapeutic agents. In terms of their utility as diagnostic agents, I developed PFCnDs that exhibit increased imaging depth, stability and biocompatibility characteristics. Additionally, the created multiplexed platform established laser-activated PFCnDs as next generation diagnostic agents. It also helped uncover valuable functional information that will be of importance for future uses of PFCnDs as both diagnostics and therapeutic agents. Furthermore, I demonstrated that laser-activated PFCnDs can be used for image-guided therapy delivery, specifically of oxygen. However, limitations regarding excessive passive release from oxygenated-PFCnDs must be addressed for higher controllability and effectiveness. As is, PFCnDs can alleviate hypoxic conditions faced by stem cells short-term, and alter hydrogels in a manner that should allow for enhanced *in vivo* integration.

Future work will continue to build upon these advancements and hope to establish laser-activated PFCnDs for clinical use. The advances achieved in this dissertation will become increasingly important as photoacoustic imaging becomes more commonplace in clinic.

# APPENDIX A. SPATIOTEMPORAL BACKGROUND-FREE IMAGING WITH PFCNDS

## A.1 Introduction

Chapters 3 and 4 focus on enhancing PFCnDs's diagnostic agent abilities. One topic discussed in both chapters is the background-free imaging ability of PFCnDs. This is accomplished using a developed algorithm that distinguishes PFCnDs's distinct ultrasound and photoacoustic temporal signal from intrinsic tissue signal. The following section provides a thorough explanation of the photoacoustic/ultrasound response of PFCnDs and the developed image processing techniques.

The temporal photoacoustic and ultrasound signal signatures of PFCnDs depend on the perfluorocarbon core utilized, i.e. whether the PFCnD exhibits a single or repeatable vaporization. The conducted diagnostic agent studies of PFCnDs all use perfluoropentane (boiling point: 29ºC) as a core, resulting in a one-time vaporization event. By observing the trends in photoacoustic or ultrasound signal overtime, it is possible to discriminate laser-triggered PFCnDs from endogenous signal.

## A.2 Methods

### *A.2.1 Synthesis of PFCnDs*

PFCnDs were synthesized with a lipid shell and encapsulated 1064 nm photoabsorber via water bath sonication (see 4.2.1 for complete description).

### *A.2.2 USPA Imaging*

All imaging experiments were conducted using a 40-MHz ultrasound and photoacoustic imaging probe (LZ-550, Visualsonics Inc.) coupled to a combined ultrasound and photoacoustic imaging system (Vevo LAZR, Visualsonics Inc). The laser operated at 1064 nm wavelength producing 5-7 ns laser pulses at 20-Hz pulse repetition rate. The fluence was measured to be between 6-9 $mJ \cdot cm^{-2}$.

### *A.2.3 In vivo imaging*

Studies conducted adhered to approved protocols by the Institutional Animal Care and Use Committee at Georgia Institute of Technology. Mice (nu/nu) were anesthetized using a combination of isoflurane (1.5-2.5%) and $O_2$ (0.8 $L \cdot min^{-1}$) and placed on an animal heating pad, regulated at 37°C, during imaging. Mice were intravenously injected with 150 µl of stock PFCnDs through the jugular vein. After sufficient time, the spleen was localized and imaged at 1064 nm. Ultrasound B-mode and photoacoustic images were collected simultaneously for 140 frames at a rate of 5 frames per second.

## A.3 Results

### *A.3.1 Photoacoustic-based background-free images*

Upon laser induced PFCnD vaporization, there is an intense photoacoustic signal. In stationary samples, the signal is at a maximum immediately after the laser pulse that causes vaporization, which is typically the first laser pulse, and then decreases overtime (Figure 24). The rate at which it decreases is dependent on the PFCnD portion that is vaporized compared to the total that are vaporized throughout the imaging period. If the entire PFCnD population in the region of interest is vaporized after the first laser pulse, then the maximum photoacoustic is large and the drop in photoacoustic signal is drastic. If some unvaporized PFCnDs remain, or subsequently enter the image plane, and are vaporized on ensuing laser pulses, then the peak photoacoustic signal is reduced, and the decay is more gradual. When all vaporization events have occurred, the photoacoustic signal drops to a baseline level representative of the thermoelastic expansion of the photoabsorber utilized (Figure 24b). The difference between the maximum photoacoustic signal and the baseline photoacoustic signal is referred to as vaporization-associated photoacoustic signal. The larger the difference, the more effective the photoabsorber is at initiating PFCnD vaporization.

Background-free imaging through localization of PFCnDs is extremely advantageous because of the endogenous photoacoustic signal seen at many wavelengths. Even at 1064 nm, which is within the optical window, there is still endogenous signal (Figure 24a). To localize vaporized PFCnDs, pixels with a rapidly decreasing photoacoustic signal were identified via image processing using MATLAB. For the technique to effectively work, it is important to image for a significant time frame in order

to capture both the decay and baseline PFCnD temporal pattern. Then, frames that capture the decay, but avoid frames depicting photoabsorber baseline signal, are selected (Figure 24b, yellow dashed square) and pixel-wise linear regression is performed. Prior to the linear fit, undesired sample motion can be accounted for by applying a spatial averaging window in spatial (X-Y plane) and time (Z) dimension. Once the linear fit is determined, the slopes from each pixel are extracted. The slopes indicate the change in photoacoustic signal over the studied time, therefore higher value slopes correlate to vaporized PFCnDs, while those with a slope closer to 0 indicate endogenous photoacoustic signal or noise (Figure 24b). A threshold value is selected to only display pixels that exhibit a large variation rate, i.e. indicative of vaporized PFCnDs. The identified pixels are then displayed over an ultrasound image for anatomical reference, resulting in a photoacoustic-based background-free image (Figure 24c).

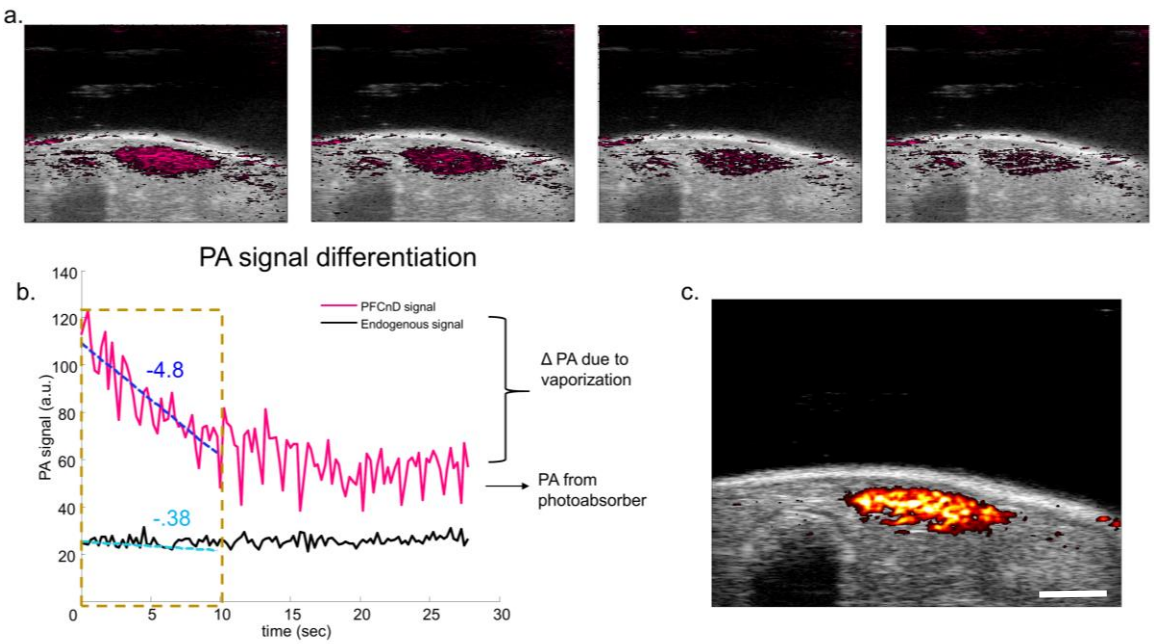


**Figure 24.** (a) Unprocessed photoacoustic signal at several different time points during the irradiation sequence. (b) Temporal photoacoustic signals of pixels with PFCnD and endogenous signal. Linear regression is performed on frames that capture the decay. Slopes (-4.8 vs -0.38) with rates above a certain threshold are identified. (c) The result is a much cleaner image, depicting only pixels where PFCnDs vaporization occurred. Scale bar = 2 mm.

*A.3.2 Ultrasound-based background-free images*

The vaporization-related ultrasound signal of PFCnDs's mirrors the photoacoustic signal, i.e. increases over time. After the vaporization initiating laser pulse, activated PFCnDs begin to transition into microbubbles. However, in order to provide effective ultrasound contrast enhancement, the created MB must first reach a minimum size. This is typically achieved at around 1 μm, depending on the imaging setup and processing available.[2, 108] Consequently, the ultrasound enhancement is less immediate compared to the photoacoustic signal. Similar to photoacoustic signal, for stationary samples the rate of increase is associated with the portion of phase-changed PFCnDs at each laser pulse. Faster rates indicate efficient vaporization, whereas slower rates indicate more laser triggers were needed. After some time, the ultrasound signal reaches a maximum and plateaus (Figure 25).

Background-free ultrasound images are extremely useful for diagnostic applications as they provide a clear special map of PFCnD location. In an analogous method to photoacoustic signal processing, pixels with rapidly increasing ultrasound signal are identified. Frames that capture the ultrasound increase are selected for processing (Figure 25b-yellow dashed square), and pixel-wise linear regression is performed.

Pixels which exhibit a slope above a certain threshold are identified as locations where microbubbles were created, i.e. PFCnD phase-change occurred (Figure 25). The selected pixels are displayed over an ultrasound image for anatomical reference, resulting in an ultrasound-based background-free image (Figure 25c).

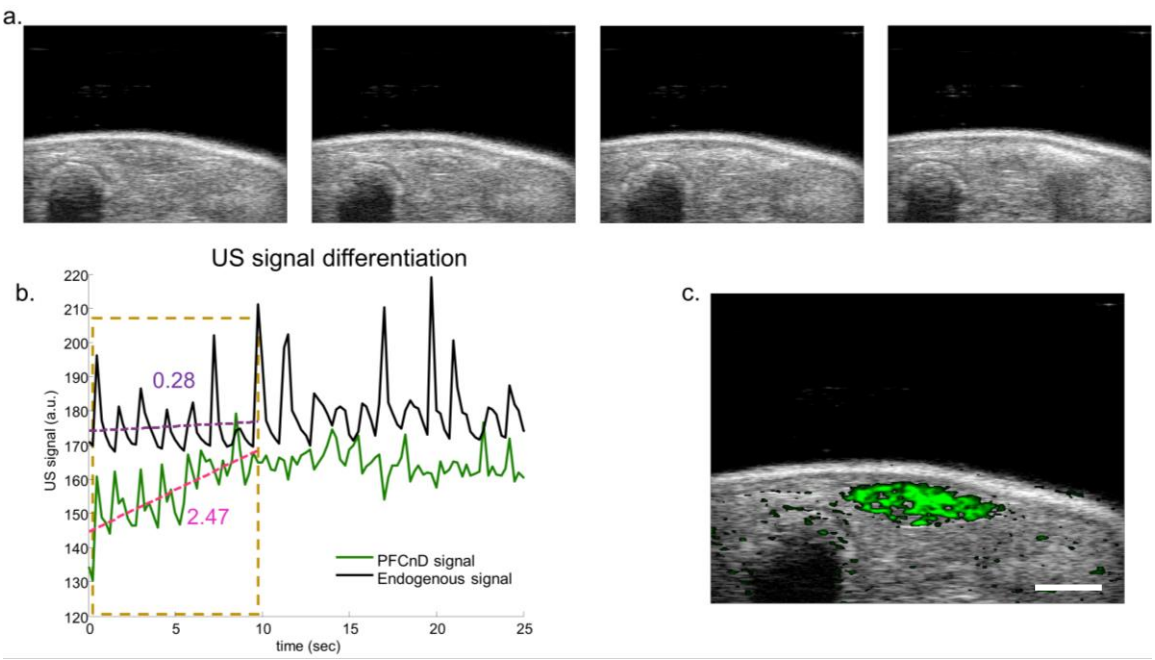


**Figure 25**. (a) Ultrasound signal at several different time points during the irradiation sequence. (b) Temporal ultrasound signals of pixels with PFCnD and endogenous signal. Linear regression is performed on frames that capture the decay. Slopes (2.47 vs 0.28) with rates above a certain threshold are identified. (c) The processed image depicts location of PFCnDs so they are more easily discernable. Scale bar = 2 mm.

## A.4 Discussion

One tremendous advantage of laser-activated PFCnDs is that they provide unique photoacoustic and ultrasound temporal contrast. This is significant because *in vivo* imaging will introduce endogenous signal and biological interaction that might affect PFCnD photoacoustic and/or ultrasound contrast. However, as along as one form of signal can be effectively processed, then background-free images can be formed. An additional benefit is that baseline imaging is not needed, as identifying vaporized PFCnDs can eliminate endogenous signal.

In order to better understand the developed algorithms, and when one form of image contrast is better-suited compared to the other, certain *in vivo* scenarios are described below.

### *A.4.1 Situations that result in reduced photoacoustic signal*

In cases of low concentration and slow flowing PFCnDs (see Chapter 3 Lymph Node example), the vaporization-associated photoacoustic signal is too weak to differentiate it from other endogenous signal. Additionally, due to optical scattering in tissue, PFCnDs outside the imaging plane may vaporize, effectively reducing the amount of PFCnDs providing photoacoustic signal in plane. This renders photoacoustic-based background-free imaging unsuitable.

The type of photoabsorber will also dictate how well photoacoustic-based signal processing will be. In instances where the vaporization event is not significantly more than its photoabsorber baseline (at least two times higher) then the processing algorithm will

struggle as the slopes between vaporizing pixels and endogenous signal will not be as different.

*A.4.2 Situations that result in reduced ultrasound signal*

In some situations, the phase-changed PFCnDs do not provide any or enough ultrasound signal to process. This can occur when the size of PFCnDs has greatly decreased, which can happen as PFC diffuses out of the PFCnDs. Since PFCnDs will expand 5 times their size upon vaporization, PFCnDs significantly smaller than 200 nm will produce bubbles of less than 1μm in size, which do not provide significant ultrasound enhancement. However, harmonic imaging and other imaging techniques may still be able to localize these smaller sub-micron bubbles.

Another instance of reduced ultrasound signal can occur when PFCnDs are taken up by cells. Cells may selectively uptake PFCnDs of reduced size, which would inhibit their provided ultrasound contrast. Alternatively, cell uptake could affect the ability of created MBs to reach their full-size potential, once again diminishing their ultrasound contrast.

# APPENDIX B. FUNCTIONALIZED PFCND PROTOCOL

Adapted from: Directional conjugation of antibodies to nanoparticles for synthesis of multiplexed optical contrast agents with both delivery and targeting moieties. Nature Protocols (2008).[101]

**PFCnD preparation**

1) Add the following into a pear shaped rotovap flask (~50 ml size preferred):

- 9.4 µl of DPPC (10mg/ml)
- 7.4 µl of DSPE-PEG2kDa (25 mg/ml)
- 2.4 µl of –MAL (10 mg/mL)
- 100 µl of Epolight dye (1mg/ml) if making laser-activated nDs
- 2.0 ml of chloroform

2) Using a Rotovap, slowly evaporate off the chloroform (i.e. slowly reduce P from its starting point) and spin at 200 RPM. Result should be a thin cake spread along the rotovap flask, if it does not look like a good lipid cake, you can add 2 more mls of chloroform and retry.

3) Once lipid cake is dry (confirm dry with N2 purge if necessary), add 1 ml of PBS. Vortex and sonicate to resuspend all the lipid in PBS.

4) Transfer solution to an 9 ml vial and add 75 µl of PFC

5) Vortex and sonicate in COLD water (add ice to water bath)

6) Wash off excess aggregated dye by spinning at 100 rcf for 1 min and retaining supernatant

**Antibody conjugation:**

*Reagents*

1) Antibody or antibodies (100ul at 1 mg/ml in PBS).
2) Linker solution (46.5 mM): Prepared by dissolving 33 mg of dithiolaromatic $PEG_6$-$CONHNH_2$ in 1 ml DIUF H2O). *Can be approximated as long as it is in excess of the antibody concentration*
3) Purpald solution: 10 mg/ml Purpald dissolved in 1N NaOH (freshly prepared).
4) 100 mM $Na_2HPO_4$
5) 100mM $NaIO_4$ [21.3 mg in 1 ml of DIUF $H_20$]
6) 1x PBS
7) 40 mM HEPES

*Procedure*

*Attaching linker to antibody*

1) Attach linker to antibody. Large batches of antibody-linker complex can be prepared and stored before nanoparticle conjugation. Dilute or resuspend antibody solution to 1 mg/ml in 1 ml of 100mM $Na_2HPO_4$, pH 7.5. If antibody solution is more dilute than 1 mg/ml, the solution will need to be concentrated and exchanged for 100mM $Na_2HPO_4$, pH 7.5.

   Our antibodies are 100 µg solutions. Therefore, for 1 mg/ml, or 1000 µg/ml it needs to be in 100 µl of $Na_2HPO_4$.

2) Add 10 µl of 100 mM $NaIO_4$ to 100 µl of 1 mg/ml antibody solution in 100 mM $Na_2HPO_4$. Incubate in the dark for 30 min at RT, 125 RPM agitation.

3) Quench the reaction with 500 µl of 1x PBS.
4) *Quality control*: To verify the oxidation of the carbohydrate, add 15 µl drop of Purpald solution [freezer] onto parafilm. Add 5µl of antibody solution and mix. The solution should turn purple in a few minutes to indicate aldehyde presence.
5) Add 2 µl of 46.5 mM linker solution, in ethanol, to the antibody solution and incubate for 1 hr. at RT while shaking, 125 RPM.
6) Add 1 ml of 40 mM HEPES and filter w/ 10k filter at 2000 g at 4C until 75% through (~10 minutes)
7) Resuspend in 40 mM HEPES to final volume of 1 ml and AB con centration at 100 ug/ml.

**FINAL PRODUCT:** Functionalized antibody with the thiol-terminated linker off the $F_C$ segment.

**PAUSE POINT:** Antibody-linker solution can be kept at 4C for the recommended storage time for the specific antibody. Linker does not affect stability of the antibody.

*Conjugation to perfluorocarbon nanodroplets (adapted from Thermo Sci protocol "Attach an antibody onto glass, silica or quartz surface)*

**Attaching antibodies to PFCnDs**

1) Combine 20 µl of antibody-linker solution with 100 µl of PFCnDs in 900 µl PBS. Incubate for 1 hour at room temperature in the dark. Use rotator for mixing 125 RPM.

   *Note: For cell studies [PFCnD] is $10^6$, stock is $10^{10}$*

2) Quality control: Use Plate reader to see if antibodies are present.
3) A 100 µl of 10-5M 5 kDa mPEG-SH is used to backfill unreacted maleimide groups and left to incubate for 1 hour, room temperature
4) Centrifuge at 900 rpm for 2 minutes to get rid of excess PEG and Abs

**In vitro cell studies**

Cells should be cultured on glass chamber slides for best results. Cell can be stained with Cell Tracker before PFCnD incubation.

1) Add targeted PFCnDs (1:10000 dilution from stock, final should be ~$10^6$ nDs/ml
2) Incubate for 1 to 2 hours in serum free media
3) Aspirate particles and wash 5 times with PBS, being careful not to detach cells
4) Fix cells with 10% Formalin for 10 minutes
5) Wash with two times with PBS, ensure slide is sufficiently dry before proceeding.
6) Add mounting media, cover glass and seal with nail polish

# REFERENCES


1. Riess, J. G., Oxygen Carriers ("Blood Substitutes") Raison d'Etre, Chemistry, and Some Physiology Blut ist ein ganz besondrer Saft 1. *Chem. Rev.* **2001,** *101* (9), 2797-2920.

2. Schutt, E. G.; Klein, D. H.; Mattrey, R. M.; Riess, J. G., Injectable microbubbles as contrast agents for diagnostic ultrasound imaging: the key role of perfluorochemicals. *Angew. Chem. Int. Ed.* **2003,** *42* (28), 3218-3235.

3. Santiesteban, D. Y.; Kubelick, K.; Dhada, K. S.; Dumani, D.; Suggs, L.; Emelianov, S., Monitoring/Imaging and Regenerative Agents for Enhancing Tissue Engineering Characterization and Therapies. *Ann. Biomed. Eng.* **2016,** *44* (3), 750-772.

4. Wilson, K.; Homan, K.; Emelianov, S., Biomedical photoacoustics beyond thermal expansion using triggered nanodroplet vaporization for contrast-enhanced imaging. *Nat. Commun.* **2012,** *3*, 618.

5. Sheeran, P. S.; Luois, S.; Dayton, P. A.; Matsunaga, T. O., Formulation and acoustic studies of a new phase-shift agent for diagnostic and therapeutic ultrasound. *Langmuir* **2011,** *27* (17), 10412-10420.

6. Kripfgans, O. D.; Fowlkes, J. B.; Miller, D. L.; Eldevik, O. P.; Carson, P. L., Acoustic droplet vaporization for therapeutic and diagnostic applications. *Ultrasound Biol. Med,* **2000,** *26* (7), 1177-1189.

7. Partlow, K. C.; Chen, J.; Brant, J. A.; Neubauer, A. M.; Meyerrose, T. E.; Creer, M. H.; Nolta, J. A.; Caruthers, S. D.; Lanza, G. M.; Wickline, S. A., 19F magnetic resonance imaging for stem/progenitor cell tracking with multiple unique perfluorocarbon nanobeacons. *FASEB J.* **2007,** *21* (8), 1647-1654.

8. Rapoport, N., Phase-shift, stimuli-responsive perfluorocarbon nanodroplets for drug delivery to cancer. *Wiley Interdiscip. Rev.: Nanomed. Nanobiotechnol.* **2012,** *4* (5), 492-510.

9. Rapoport, N., Drug-Loaded Perfluorocarbon Nanodroplets for Ultrasound-Mediated Drug Delivery. In *Therapeutic Ultrasound*, 2016; pp 221-241.

10. Apfel, R. E., Activatable infusable dispersions containing drops of a superheated liquid for methods of therapy and diagnosis. Google Patents: 1998.

11. Moncion, A.; Arlotta, K. J.; Kripfgans, O. D.; Fowlkes, J. B.; Carson, P. L.; Putnam, A. J.; Franceschi, R. T.; Fabiilli, M. L., Design and characterization of fibrin-based acoustically responsive scaffolds for tissue engineering applications. *Ultrasound Biol. Med,* **2016,** *42* (1), 257-271.

12. Dayton, P. A.; Zhao, S.; Bloch, S. H.; Schumann, P.; Penrose, K.; Matsunaga, T. O.; Zutshi, R.; Doinikov, A.; Ferrara, K. W., Application of ultrasound to selectively localize nanodroplets for targeted imaging and therapy. *Molecular imaging* **2006,** *5* (3), 7290.2006. 00019.

13. Reznik, N.; Williams, R.; Burns, P. N., Investigation of vaporized submicron perfluorocarbon droplets as an ultrasound contrast agent. *Ultrasound Biol. Med,* **2011,** *37* (8), 1271-1279.

14. Wang, S.; Hossack, J. A.; Klibanov, A. L., Targeting of microbubbles-contrast agents for ultrasound molecular imaging. *Journal of drug targeting* **2017,** (just-accepted), 1-45.

15. Sippel, S.; Muruganandan, K.; Levine, A.; Shah, S., Use of ultrasound in the developing world. *International journal of emergency medicine* **2011,** *4* (1), 72.

16. Kim, G.-W.; Kang, C.; Oh, Y.-B.; Ko, M.-H.; Seo, J.-H.; Lee, D., Ultrasonographic Imaging and Anti-inflammatory Therapy of Muscle and Tendon Injuries Using Polymer Nanoparticles. *Theranostics* **2017,** *7* (9), 2463.

17. Bell, A. G., ART. XXXIV.--On the Production and Reproduction of Sound by Light. *American Journal of Science (1880-1910)* **1880,** *20* (118), 305.

18. Beard, P., Biomedical photoacoustic imaging. *Interface focus* **2011**, rsfs20110028.

19. Gambhir, S. S., Molecular imaging of cancer with positron emission tomography. *Nature Reviews Cancer* **2002,** *2* (9), 683-693.

20. Ntziachristos, V.; Ripoll, J.; Wang, L. V.; Weissleder, R., Looking and listening to light: the evolution of whole-body photonic imaging. *Nat. Biotechnol.* **2005,** *23* (3), 313-320.

21. Xu, M.; Wang, L. V., Photoacoustic imaging in biomedicine. *Rev. Sci. Instrum.* **2006,** *77* (4), 041101.

22. de la Zerda, A., Photoacoustic Imaging: Development of Imaging Systems and Molecular Agents. In *Engineering in Translational Medicine*, Cai, W., Ed. Springer London: London, 2014; pp 799-833.

23. Weissleder, R., A clearer vision for in vivo imaging. *Nat. Biotechnol.* **2001,** *19* (4), 316-316.

24. Smith, A. M.; Mancini, M. C.; Nie, S., Bioimaging: Second window for in vivo imaging. *Nat Nano* **2009,** *4* (11), 710-711.

25. Dana, N. P., Diego S. Dumani, Jason R. Cook, and Stanislav Emelianov, Overview of Photoacoustic Imaging. In *Advances in Medical Physics*, Devon J. Godfrey, J. V. D.,

Shiva K. Das, Bruce H. Curran and Anthony B. Wolbarst, Ed. Medical Physics Publishing: Madison, WI, 2016; pp 47-70.

26. Zhang, H. F.; Maslov, K.; Stoica, G.; Wang, L. V., Functional photoacoustic microscopy for high-resolution and noninvasive in vivo imaging. *Nat. Biotechnol.* **2006,** *24* (7), 848-851.

27. Wang, L. V.; Hu, S., Photoacoustic tomography: in vivo imaging from organelles to organs. *Science* **2012,** *335* (6075), 1458-1462.

28. Luke, G. P.; Yeager, D.; Emelianov, S. Y., Biomedical applications of photoacoustic imaging with exogenous contrast agents. *Ann. Biomed. Eng.* **2012,** *40* (2), 422-437.

29. Mehrmohammadi, M.; Joon Yoon, S.; Yeager, D.; Y Emelianov, S., Photoacoustic imaging for cancer detection and staging. *Current molecular imaging* **2013,** *2* (1), 89-105.

30. Mallidi, S.; Luke, G. P.; Emelianov, S., Photoacoustic imaging in cancer detection, diagnosis, and treatment guidance. *Trends Biotechnol.* **2011,** *29* (5), 213-221.

31. Bayer, C. L.; Chen, Y.-S.; Kim, S.; Mallidi, S.; Sokolov, K.; Emelianov, S., Multiplex photoacoustic molecular imaging using targeted silica-coated gold nanorods. *Biomed. Opt. Express* **2011,** *2* (7), 1828-1835.

32. Taruttis, A.; Ntziachristos, V., Advances in real-time multispectral optoacoustic imaging and its applications. *Nature Photonics* **2015,** *9* (4), 219-227.

33. Lu, H. D.; Wilson, B. K.; Lim, T. L.; Heinmiller, A.; Prud'homme, R. K., Real-time and multiplexed photoacoustic imaging of internally normalized mixed-targeted nanoparticles. *ACS Biomaterials Science & Engineering* **2017,** *3* (3), 443-451.

34. Santiesteban, D. Y.; Dumani, D. S.; Profili, D.; Emelianov, S. Y., Copper sulfide perfluorocarbon nanodroplets as clinically relevant photoacoustic/ultrasound imaging agents. *Nano Lett.* **2017**.

35. Niederhauser, J. J.; Jaeger, M.; Lemor, R.; Weber, P.; Frenz, M., Combined ultrasound and optoacoustic system for real-time high-contrast vascular imaging in vivo. *IEEE transactions on medical imaging* **2005,** *24* (4), 436-440.

36. Wang, B.; Karpiouk, A.; Yeager, D.; Amirian, J.; Litovsky, S.; Smalling, R.; Emelianov, S., In vivo intravascular ultrasound-guided photoacoustic imaging of lipid in plaques using an animal model of atherosclerosis. *Ultrasound Biol. Med,* **2012,** *38* (12), 2098-2103.

37. Emelianov, S. Y.; Li, P.-C.; O'Donnell, M., Photoacoustics for molecular imaging and therapy. *Physics today* **2009,** *62* (8), 34.

38. Xia, J.; Yao, J.; Wang, L. V., Photoacoustic tomography: principles and advances. *Electromagnetic waves (Cambridge, Mass.)* **2014,** *147*, 1.

39. Sheeran, P. S.; Matsunaga, T. O.; Dayton, P. A., Phase change events of volatile liquid perfluorocarbon contrast agents produce unique acoustic signatures. *Physics in medicine and biology* **2013,** *59* (2), 379.

40. Parakh, S.; Gan, H. K.; Parslow, A. C.; Burvenich, I. J.; Burgess, A. W.; Scott, A. M., Evolution of anti-HER2 therapies for cancer treatment. *Cancer treatment reviews* **2017,** *59*, 1-21.

41. James, M. L.; Gambhir, S. S., A molecular imaging primer: modalities, imaging agents, and applications. *Physiological reviews* **2012,** *92* (2), 897-965.

42. Deshpande, N.; Needles, A.; Willmann, J. K., Molecular ultrasound imaging: current status and future directions. *Clinical radiology* **2010,** *65* (7), 567-581.

43. Lanza, G. M.; Wallace, K. D.; Scott, M. J.; Cacheris, W. P.; Abendschein, D. R.; Christy, D. H.; Sharkey, A. M.; Miller, J. G.; Gaffney, P. J.; Wickline, S. A., A novel site-targeted ultrasonic contrast agent with broad biomedical application. *Circulation* **1996,** *94* (12), 3334-3340.

44. Rapoport, N.; Gupta, R.; Kim, Y.-S.; O'neill, B. E., Polymeric micelles and nanoemulsions as tumor-targeted drug carriers: insight through intravital imaging. *J. Controlled Release* **2015,** *206*, 153-160.

45. Wilhelm, S.; Tavares, A. J.; Dai, Q.; Ohta, S.; Audet, J.; Dvorak, H. F.; Chan, W. C., Analysis of nanoparticle delivery to tumours. *Nature Reviews Materials* **2016,** *1*, 16014.

46. Akers, W. J.; Kim, C.; Berezin, M.; Guo, K.; Fuhrhop, R.; Lanza, G. M.; Fischer, G. M.; Daltrozzo, E.; Zumbusch, A.; Cai, X., Noninvasive photoacoustic and fluorescence sentinel lymph node identification using dye-loaded perfluorocarbon nanoparticles. *ACS nano* **2010,** *5* (1), 173-182.

47. Hannah, A. S.; Luke, G. P.; Emelianov, S. Y., Blinking Phase-Change Nanocapsules Enable Background-Free Ultrasound Imaging. *Theranostics* **2016,** *6* (11), 1866.

48. Yoon, H.; Yarmoska, S. K.; Hannah, A. S.; Yoon, C.; Hallam, K. A.; Emelianov, S. Y., Contrast-enhanced ultrasound imaging in vivo with laser-activated nanodroplets. *Medical Physics* **2017**.

49. Unger, E. C.; Porter, T.; Culp, W.; Labell, R.; Matsunaga, T.; Zutshi, R., Therapeutic applications of lipid-coated microbubbles. *Adv. Drug Delivery Rev.* **2004,** *56* (9), 1291-1314.

50. Rapoport, N.; Marin, A.; Luo, Y.; Prestwich, G. D.; Muniruzzaman, M., Intracellular uptake and trafficking of Pluronic micelles in drug-sensitive and MDR cells: Effect on the intracellular drug localization. *J. Pharm. Sci.* **2002,** *91* (1), 157-170.

51. Riess, J. G., Understanding the fundamentals of perfluorocarbons and perfluorocarbon emulsions relevant to in vivo oxygen delivery. *Artificial cells, blood substitutes, and biotechnology* **2005,** *33* (1), 47-63.

52. Gao, Z.; Kennedy, A. M.; Christensen, D. A.; Rapoport, N. Y., Drug-loaded nano/microbubbles for combining ultrasonography and targeted chemotherapy. *Ultrasonics* **2008,** *48* (4), 260-270.

53. Rapoport, N.; Nam, K.-H.; Gupta, R.; Gao, Z.; Mohan, P.; Payne, A.; Todd, N.; Liu, X.; Kim, T.; Shea, J., Ultrasound-mediated tumor imaging and nanotherapy using drug loaded, block copolymer stabilized perfluorocarbon nanoemulsions. *J. Controlled Release* **2011,** *153* (1), 4-15.

54. Fabiilli, M. L.; Lee, J. A.; Kripfgans, O. D.; Carson, P. L.; Fowlkes, J. B., Delivery of water-soluble drugs using acoustically triggered perfluorocarbon double emulsions. *Pharm. Res.* **2010,** *27* (12), 2753-2765.

55. Duncanson, W. J.; Arriaga, L. R.; Ung, W. L.; Kopechek, J. A.; Porter, T. M.; Weitz, D. A., Microfluidic fabrication of perfluorohexane-shelled double emulsions for controlled loading and acoustic-triggered release of hydrophilic agents. *Langmuir* **2014,** *30* (46), 13765-13770.

56. Riess, J. G., Perfluorocarbon-based oxygen delivery. *Artificial cells, blood substitutes, and biotechnology* **2006,** *34* (6), 567-580.

57. Marshalek, J. P.; Sheeran, P. S.; Ingram, P.; Dayton, P. A.; Witte, R. S.; Matsunaga, T. O., Intracellular delivery and ultrasonic activation of folate receptor-targeted phase-change contrast agents in breast cancer cells in vitro. *J. Controlled Release* **2016,** *243*, 69-77.

58. Ishijima, A.; Minamihata, K.; Yamaguchi, S.; Yamahira, S.; Ichikawa, R.; Kobayashi, E.; Iijima, M.; Shibasaki, Y.; Azuma, T.; Nagamune, T., Selective intracellular vaporisation of antibody-conjugated phase-change nano-droplets in vitro. *Scientific Reports* **2017,** *7*, 44077.

59. Kaneda, M. M.; Caruthers, S.; Lanza, G. M.; Wickline, S. A., Perfluorocarbon nanoemulsions for quantitative molecular imaging and targeted therapeutics. *Ann. Biomed. Eng.* **2009,** *37* (10), 1922-1933.

60. Soman, N. R.; Baldwin, S. L.; Hu, G.; Marsh, J. N.; Lanza, G. M.; Heuser, J. E.; Arbeit, J. M.; Wickline, S. A.; Schlesinger, P. H., Molecularly targeted nanocarriers deliver the cytolytic peptide melittin specifically to tumor cells in mice, reducing tumor growth. *The Journal of clinical investigation* **2009,** *119* (9), 2830.

61. Soman, N. R.; Lanza, G. M.; Heuser, J. M.; Schlesinger, P. H.; Wickline, S. A., Synthesis and characterization of stable fluorocarbon nanostructures as drug delivery vehicles for cytolytic peptides. *Nano Lett.* **2008,** *8* (4), 1131-1136.

62. Subczynski, W. K.; Hyde, J. S.; Kusumi, A., Oxygen permeability of phosphatidylcholine--cholesterol membranes. *Proceedings of the National Academy of Sciences* **1989,** *86* (12), 4474-4478.

63. Lee, H.-Y.; Kim, H.-W.; Lee, J. H.; Oh, S. H., Controlling oxygen release from hollow microparticles for prolonged cell survival under hypoxic environment. *Biomaterials* **2015,** *53*, 583-591.

64. Song, G.; Ji, C.; Liang, C.; Song, X.; Yi, X.; Dong, Z.; Yang, K.; Liu, Z., TaOx decorated perfluorocarbon nanodroplets as oxygen reservoirs to overcome tumor hypoxia and enhance cancer radiotherapy. *Biomaterials* **2017,** *112*, 257-263.

65. Song, X.; Feng, L.; Liang, C.; Yang, K.; Liu, Z., Ultrasound Triggered Tumor Oxygenation with Oxygen-Shuttle Nanoperfluorocarbon to Overcome Hypoxia-Associated Resistance in Cancer Therapies. *Nano Lett.* **2016**.

66. Anselmo, A. C.; Mitragotri, S., A review of clinical translation of inorganic nanoparticles. *The AAPS journal* **2015,** *17* (5), 1041-1054.

67. Cheon, J.; Lee, J.-H., Synergistically integrated nanoparticles as multimodal probes for nanobiotechnology. *Acc. Chem. Res.* **2008,** *41* (12), 1630-1640.

68. Huynh, E.; Rajora, M. A.; Zheng, G., Multimodal micro, nano, and size conversion ultrasound agents for imaging and therapy. *Wiley Interdiscip. Rev.: Nanomed. Nanobiotechnol.* **2016**.

69. Wei, C.-w.; Lombardo, M.; Larson-Smith, K.; Pelivanov, I.; Perez, C.; Xia, J.; Matula, T.; Pozzo, D.; O'Donnell, M., Nonlinear contrast enhancement in photoacoustic molecular imaging with gold nanosphere encapsulated nanoemulsions. *Appl. Phys. Lett.* **2014,** *104* (3), 033701.

70. Hannah, A.; Luke, G.; Wilson, K.; Homan, K.; Emelianov, S., Indocyanine green-loaded photoacoustic nanodroplets: dual contrast nanoconstructs for enhanced photoacoustic and ultrasound imaging. *ACS nano* **2013,** *8* (1), 250-259.

71. Paproski, R. J.; Forbrich, A.; Huynh, E.; Chen, J.; Lewis, J. D.; Zheng, G.; Zemp, R. J., Porphyrin Nanodroplets: Sub-micrometer Ultrasound and Photoacoustic Contrast Imaging Agents. *Small* **2016,** *12* (3), 371-380.

72. Hannah, A. S.; VanderLaan, D.; Chen, Y.-S.; Emelianov, S. Y., Photoacoustic and ultrasound imaging using dual contrast perfluorocarbon nanodroplets triggered by laser pulses at 1064 nm. *Biomed. Opt. Express* **2014,** *5* (9), 3042-3052.

73. Chen, Y.-S.; Frey, W.; Kim, S.; Homan, K.; Kruizinga, P.; Sokolov, K.; Emelianov, S., Enhanced thermal stability of silica-coated gold nanorods for photoacoustic imaging and image-guided therapy. *Opt. Express* **2010,** *18* (9), 8867-8878.

74. Zhou, M.; Zhang, R.; Huang, M.; Lu, W.; Song, S.; Melancon, M. P.; Tian, M.; Liang, D.; Li, C., A chelator-free multifunctional [64Cu] CuS nanoparticle platform for simultaneous micro-PET/CT imaging and photothermal ablation therapy. *J. Am. Chem. Soc.* **2010,** *132* (43), 15351-15358.

75. Li, Y.; Lu, W.; Huang, Q.; Li, C.; Chen, W., Copper sulfide nanoparticles for photothermal ablation of tumor cells. *Nanomedicine* **2010,** *5* (8), 1161-1171.

76. Guo, L.; Panderi, I.; Yan, D. D.; Szulak, K.; Li, Y.; Chen, Y.-T.; Ma, H.; Niesen, D. B.; Seeram, N.; Ahmed, A., A comparative study of hollow copper sulfide nanoparticles and hollow gold nanospheres on degradability and toxicity. *ACS nano* **2013,** *7* (10), 8780-8793.

77. Goel, S.; Chen, F.; Cai, W., Synthesis and biomedical applications of copper sulfide nanoparticles: from sensors to theranostics. *Small* **2014,** *10* (4), 631-645.

78. Luke, G. P.; Hannah, A. S.; Emelianov, S. Y., Super-resolution ultrasound imaging in vivo with transient laser-activated nanodroplets. *Nano Lett.* **2016,** *16* (4), 2556-2559.

79. American National Standard for Safe Use of Lasers. In *ANSI Z136.1*, America, L. I. o., Ed. Laser Institute of America: 2007.

80. Chang, S.-S.; Shih, C.-W.; Chen, C.-D.; Lai, W.-C.; Wang, C. C., The shape transition of gold nanorods. *Langmuir* **1999,** *15* (3), 701-709.

81. Moghimi, S. M.; Hunter, A.; Andresen, T., Factors controlling nanoparticle pharmacokinetics: an integrated analysis and perspective. *Annu. Rev. Pharmacool. Toxicol.* **2012,** *52*, 481-503.

82. Cataldi, M.; Vigliotti, C.; Mosca, T.; Cammarota, M.; Capone, D., Emerging Role of the Spleen in the Pharmacokinetics of Monoclonal Antibodies, Nanoparticles and Exosomes. *Int. J. Mol. Sci.* **2017,** *18* (6), 1249.

83. Ku, G.; Zhou, M.; Song, S.; Huang, Q.; Hazle, J.; Li, C., Copper sulfide nanoparticles as a new class of photoacoustic contrast agent for deep tissue imaging at 1064 nm. *Acs Nano* **2012,** *6* (8), 7489-7496.

84. Zhou, M.; Li, J.; Liang, S.; Sood, A. K.; Liang, D.; Li, C., CuS nanodots with ultrahigh efficient renal clearance for positron emission tomography imaging and image-guided photothermal therapy. *ACS nano* **2015,** *9* (7), 7085-7096.

85. Cheng, Z.; Zhong, H.; Xu, J.; Chu, X.; Song, Y.; Xu, M.; Huang, H., Facile fabrication of ultrasmall and uniform copper nanoparticles. *Mater. Lett.* **2011,** *65* (19), 3005-3008.

86. Huggenberger, R.; Detmar, M. In *The cutaneous vascular system in chronic skin inflammation*, Journal of Investigative Dermatology Symposium Proceedings, Elsevier: 2011; pp 24-32.

87. Mumprecht, V.; Roudnicky, F.; Detmar, M., Inflammation-induced lymph node lymphangiogenesis is reversible. *Am. J. Pathol.* **2012,** *180* (3), 874-879.

88. Varricchi, G.; Granata, F.; Loffredo, S.; Genovese, A.; Marone, G., Angiogenesis and lymphangiogenesis in inflammatory skin disorders. *J. Am. Acad. Dermatol.* **2015,** *73* (1), 144-153.

89. Coussens, L. M.; Werb, Z., Inflammation and cancer. *Nature* **2002,** *420* (6917), 860-867.

90. Sleeman, J. P., The lymph node pre-metastatic niche. *Journal of Molecular Medicine* **2015,** *93* (11), 1173-1184.

91. Reddy, S. T.; Rehor, A.; Schmoekel, H. G.; Hubbell, J. A.; Swartz, M. A., In vivo targeting of dendritic cells in lymph nodes with poly (propylene sulfide) nanoparticles. *J. Controlled Release* **2006,** *112* (1), 26-34.

92. Oussoren, C.; Storm, G., Liposomes to target the lymphatics by subcutaneous administration. *Adv. Drug Delivery Rev.* **2001,** *50* (1), 143-156.

93. Zhang, F.; Niu, G.; Lu, G.; Chen, X., Preclinical lymphatic imaging. *Mol. Imaging Biol.* **2011,** *13* (4), 599-612.

94. Kurotaki, D.; Uede, T.; Tamura, T., Functions and development of red pulp macrophages. *Microbiol. Immunol.* **2015,** *59* (2), 55-62.

95. Bauer, K. R.; Brown, M.; Cress, R. D.; Parise, C. A.; Caggiano, V., Descriptive analysis of estrogen receptor (ER)-negative, progesterone receptor (PR)-negative, and HER2-negative invasive breast cancer, the so-called triple-negative phenotype. *Cancer* **2007,** *109* (9), 1721-1728.

96. Osborne, C. K.; Yochmowitz, M. G.; Knight, W. A.; McGuire, W. L., The value of estrogen and progesterone receptors in the treatment of breast cancer. *Cancer* **1980,** *46* (S12), 2884-2888.

97. La Thangue, N. B.; Kerr, D. J., Predictive biomarkers: a paradigm shift towards personalized cancer medicine. *Nature reviews Clinical oncology* **2011,** *8* (10), 587-596.

98. Heinzmann, K.; Carter, L. M.; Lewis, J. S.; Aboagye, E. O., Multiplexed imaging for diagnosis and therapy. *Nature Biomedical Engineering* **2017,** *1* (9), 697.

99. Vendrell, M.; Maiti, K. K.; Dhaliwal, K.; Chang, Y.-T., Surface-enhanced Raman scattering in cancer detection and imaging. *Trends Biotechnol.* **2013,** *31* (4), 249-257.

100. Ueda, S.; Saeki, T.; Osaki, A.; Yamane, T.; Kuji, I., Bevacizumab induces acute hypoxia and cancer progression in patients with refractory breast cancer: Multimodal functional imaging and multiplex cytokine analysis. *Clinical Cancer Research* **2017**.

101. Kumar, S.; Aaron, J.; Sokolov, K., Directional conjugation of antibodies to nanoparticles for synthesis of multiplexed optical contrast agents with both delivery and targeting moieties. *Nature protocols* **2008,** *3* (2), 314-320.

102. Kowala, M.; Schoefl, G., The popliteal lymph node of the mouse: internal architecture, vascular distribution and lymphatic supply. *Journal of anatomy* **1986,** *148*, 25.

103. Li, D. S.; Yoon, S. J.; Pelivanov, I.; Frenz, M.; O'Donnell, M.; Pozzo, L. D., Polypyrrole-Coated Perfluorocarbon Nanoemulsions as a Sono-Photoacoustic Contrast Agent. *Nano Lett.* **2017,** *17* (10), 6184-6194.

104. Rohner, N. A.; Thomas, S. N., Flexible Macromolecule versus Rigid Particle Retention in the Injected Skin and Accumulation in Draining Lymph Nodes Are Differentially Influenced by Hydrodynamic Size. *ACS Biomaterials Science & Engineering* **2016,** *3* (2), 153-159.

105. Manolova, V.; Flace, A.; Bauer, M.; Schwarz, K.; Saudan, P.; Bachmann, M. F., Nanoparticles target distinct dendritic cell populations according to their size. *European journal of immunology* **2008,** *38* (5), 1404-1413.

106. Dumani, D.; Sun, I.-C.; Emelianov, S. In *In vivo photoacoustic detection of lymph node metastasis using glycol-chitosan-coated gold nanoparticles*, Ultrasonics Symposium (IUS), 2017 IEEE International, IEEE: 2017; pp 1-4.

107. Gamvrellis, A.; Leong, D.; Hanley, J. C.; Xiang, S. D.; Mottram, P.; Plebanski, M., Vaccines that facilitate antigen entry into dendritic cells. *Immunology and cell biology* **2004,** *82* (5), 506-516.

108. Gorce, J.-M.; Arditi, M.; Schneider, M., Influence of bubble size distribution on the echogenicity of ultrasound contrast agents: A study of SonoVue™. *Investigative radiology* **2000,** *35* (11), 661-671.

109. Albertini, J. J.; Lyman, G. H.; Cox, C.; Yeatman, T.; Balducci, L.; Ku, N.; Shivers, S.; Berman, C.; Wells, K.; Rapaport, D., Lymphatic mapping and sentinel node biopsy in the patient with breast cancer. *Jama* **1996,** *276* (22), 1818-1822.

110. Krag, D.; Weaver, D.; Alex, J.; Fairbank, J.; et al., Surgical resection and radiolocalization of the sentinel lymph node in breast cancer using a gamma probe. *Surgical oncology* **1993,** *2* (6), 335-340.

111. Thomas, S. N.; Vokali, E.; Lund, A. W.; Hubbell, J. A.; Swartz, M. A., Targeting the tumor-draining lymph node with adjuvanted nanoparticles reshapes the anti-tumor immune response. *Biomaterials* **2014,** *35* (2), 814-824.

112. Leleux, J.; Atalis, A.; Roy, K., Engineering immunity: Modulating dendritic cell subsets and lymph node response to direct immune-polarization and vaccine efficacy. *J. Controlled Release* **2015,** *219*, 610-621.

113. Kushwah, R.; Hu, J., Complexity of dendritic cell subsets and their function in the host immune system. *Immunology* **2011,** *133* (4), 409-419.

114. Liang, R.; Xie, J.; Li, J.; Wang, K.; Liu, L.; Gao, Y.; Hussain, M.; Shen, G.; Zhu, J.; Tao, J., Liposomes-coated gold nanocages with antigens and adjuvants targeted delivery to dendritic cells for enhancing antitumor immune response. *Biomaterials* **2017,** *149*, 41-50.

115. Hankey, G. J.; Norman, P. E.; Eikelboom, J. W., Medical treatment of peripheral arterial disease. *Jama* **2006,** *295* (5), 547-553.

116. Dua, A.; Lee, C. J., Epidemiology of peripheral arterial disease and critical limb ischemia. *Techniques in vascular and interventional radiology* **2016,** *19* (2), 91-95.

117. Hirsch, A. T.; Criqui, M. H.; Treat-Jacobson, D.; Regensteiner, J. G.; Creager, M. A.; Olin, J. W.; Krook, S. H.; Hunninghake, D. B.; Comerota, A. J.; Walsh, M. E., Peripheral arterial disease detection, awareness, and treatment in primary care. *Jama* **2001,** *286* (11), 1317-1324.

118. Criqui, M. H.; Langer, R. D.; Fronek, A.; Feigelson, H. S.; Klauber, M. R.; McCann, T. J.; Browner, D., Mortality over a period of 10 years in patients with peripheral arterial disease. *New England Journal of Medicine* **1992,** *326* (6), 381-386.

119. Criqui, M. H.; Denenberg, J. O.; Langer, R. D.; Fronek, A., The epidemiology of peripheral arterial disease: importance of identifying the population at risk. *Vascular Medicine* **1997,** *2* (3), 221-226.

120. Botti, C.; Maione, C.; Coppola, A.; Sica, V.; Cobellis, G., Autologous bone marrow cell therapy for peripheral arterial disease. *Stem cells and cloning: advances and applications* **2012,** *5*, 5.

121. Gupta, N. K.; Armstrong, E. J.; Parikh, S. A., The Current State of Stem Cell Therapy for Peripheral Artery Disease. *Current Cardiology Reports* **2014,** *16* (2), 447.

122. Van Den Akker, F.; Deddens, J.; Doevendans, P.; Sluijter, J., Cardiac stem cell therapy to modulate inflammation upon myocardial infarction. *Biochimica et Biophysica Acta (BBA)-General Subjects* **2013,** *1830* (2), 2449-2458.

123. Shim, W.; Mehta, A.; Wong, P.; Chua, T.; Koh, T. H., Critical path in cardiac stem cell therapy: an update on cell delivery. *Cytotherapy* **2013,** *15* (4), 399-415.

124. Nigro, P.; Bassetti, B.; Cavallotti, L.; Catto, V.; Carbucicchio, C.; Pompilio, G., Cell therapy for heart disease after 15 years: Unmet expectations. *Pharmacol. Res.* **2017**.

125. Khan, A.; Menon, A.; Tongers, J., Cell-Based Therapy in Ischemic Heart Disease. In *Biochemical Basis and Therapeutic Implications of Angiogenesis*, Mehta, J. L.; Mathur, P.; Dhalla, N. S., Eds. Springer International Publishing: Cham, 2017; pp 343-359.

126. Jadczyk, T.; Faulkner, A.; Madeddu, P., Stem cell therapy for cardiovascular disease: the demise of alchemy and rise of pharmacology. *British journal of pharmacology* **2013,** *169* (2), 247-268.

127. Segers, V. F.; Lee, R. T., Stem-cell therapy for cardiac disease. *Nature* **2008,** *451* (7181), 937-942.

128. Abdelwahid, E.; Kalvelyte, A.; Stulpinas, A.; de Carvalho, K. A. T.; Guarita-Souza, L. C.; Foldes, G., Stem cell death and survival in heart regeneration and repair. *Apoptosis* **2016,** *21* (3), 252-268.

129. Laflamme, M. A.; Murry, C. E., Regenerating the heart. *Nat. Biotechnol.* **2005,** *23* (7), 845.

130. Loffredo, L.; Marcoccia, A.; Pignatelli, P.; Andreozzi, P.; Borgia, M.; Cangemi, R.; Chiarotti, F.; Violi, F., Oxidative-stress-mediated arterial dysfunction in patients with peripheral arterial disease. *European heart journal* **2007,** *28* (5), 608-612.

131. Zhang, H.; Chen, H.; Wang, W.; Wei, Y.; Hu, S., Cell survival and redistribution after transplantation into damaged myocardium. *Journal of cellular and molecular medicine* **2010,** *14* (5), 1078-1082.

132. Hu, X.; Yu, S. P.; Fraser, J. L.; Lu, Z.; Ogle, M. E.; Wang, J.-A.; Wei, L., Transplantation of hypoxia-preconditioned mesenchymal stem cells improves infarcted heart function via enhanced survival of implanted cells and angiogenesis. *The Journal of thoracic and cardiovascular surgery* **2008,** *135* (4), 799-808.

133. Golpanian, S.; Wolf, A.; Hatzistergos, K. E.; Hare, J. M., Rebuilding the damaged heart: mesenchymal stem cells, cell-based therapy, and engineered heart tissue. *Physiological Reviews* **2016,** *96* (3), 1127-1168.

134. Ungerleider, J. L.; Christman, K. L., Concise review: injectable biomaterials for the treatment of myocardial infarction and peripheral artery disease: translational challenges and progress. *Stem cells translational medicine* **2014,** *3* (9), 1090-1099.

135. Shin, J.-Y.; Yoon, J.-K.; Noh, M. K.; Bhang, S. H.; Kim, B.-S., Enhancing Therapeutic Efficacy and Reducing Cell Dosage in Stem Cell Transplantation Therapy for Ischemic Limb Diseases by Modifying the Cell Injection Site. *Tissue Engineering Part A* **2016,** *22* (3-4), 349-362.

136. Farris, A. L.; Rindone, A. N.; Grayson, W. L., Oxygen delivering biomaterials for tissue engineering. *Journal of Materials Chemistry B* **2016,** *4* (20), 3422-3432.

137. Mohyeldin, A.; Garzón-Muvdi, T.; Quiñones-Hinojosa, A., Oxygen in stem cell biology: a critical component of the stem cell niche. *Cell stem cell* **2010,** *7* (2), 150-161.

138. Yoshida, Y.; Takahashi, K.; Okita, K.; Ichisaka, T.; Yamanaka, S., Hypoxia enhances the generation of induced pluripotent stem cells. *Cell stem cell* **2009,** *5* (3), 237-241.

139. Benjamin, S.; Sheyn, D.; Ben-David, S.; Oh, A.; Kallai, I.; Li, N.; Gazit, D.; Gazit, Z., Oxygenated environment enhances both stem cell survival and osteogenic differentiation. *Tissue Engineering Part A* **2013,** *19* (5-6), 748-758.

140. Pugh, C. W.; Ratcliffe, P. J., Regulation of angiogenesis by hypoxia: role of the HIF system. *Nature medicine* **2003,** *9* (6), 677-684.

141. Semenza, G. L., Vascular responses to hypoxia and ischemia. *Arteriosclerosis, thrombosis, and vascular biology* **2010,** *30* (4), 648-652.

142. Naderi-Meshkin, H.; Bahrami, A. R.; Bidkhori, H. R.; Mirahmadi, M.; Ahmadiankia, N., Strategies to improve homing of mesenchymal stem cells for greater efficacy in stem cell therapy. *Cell biology international* **2015,** *39* (1).

143. Rosova, I.; Dao, M.; Capoccia, B.; Link, D.; Nolta, J. A., Hypoxic preconditioning results in increased motility and improved therapeutic potential of human mesenchymal stem cells. *Stem cells* **2008,** *26* (8), 2173-2182.

144. Das, R.; Jahr, H.; van Osch, G. J.; Farrell, E., The role of hypoxia in bone marrow–derived mesenchymal stem cells: considerations for regenerative medicine approaches. *Tissue Engineering Part B: Reviews* **2009,** *16* (2), 159-168.

145. Bauer, J.; Zähres, M.; Zellermann, A.; Kirsch, M.; Petrat, F.; de Groot, H.; Mayer, C., Perfluorocarbon-filled poly (lactide-co-gylcolide) nano-and microcapsules as artificial oxygen carriers for blood substitutes: a physico-chemical assessment. *J. Microencapsulation* **2010,** *27* (2), 122-132.

146. Scott, M. G.; Kucik, D. F.; Goodnough, L. T.; Monk, T. G., Blood substitutes: evolution and future applications. *Clin. Chem.* **1997,** *43* (9), 1724-1731.

147. Gholipourmalekabadi, M.; Zhao, S.; Harrison, B. S.; Mozafari, M.; Seifalian, A. M., Oxygen-Generating Biomaterials: A New, Viable Paradigm for Tissue Engineering? *Trends Biotechnol.* **2016,** *34* (12), 1010-1021.

148. Cohn, C. S.; Cushing, M. M., Oxygen therapeutics: perfluorocarbons and blood substitute safety. *Critical care clinics* **2009,** *25* (2), 399-414.

149. Cabrales, P.; Intaglietta, M., Blood substitutes: evolution from non-carrying to oxygen and gas carrying fluids. *ASAIO journal (American Society for Artificial Internal Organs: 1992)* **2013,** *59* (4), 337.

150. Rytlewski, J. A.; Aldon, M. A.; Lewis, E. W.; Suggs, L. J., Mechanisms of tubulogenesis and endothelial phenotype expression by MSCs. *Microvascular research* **2015,** *99*, 26-35.

151. Kimelman-Bleich, N.; Pelled, G.; Sheyn, D.; Kallai, I.; Zilberman, Y.; Mizrahi, O.; Tal, Y.; Tawackoli, W.; Gazit, Z.; Gazit, D., The use of a synthetic oxygen carrier-enriched hydrogel to enhance mesenchymal stem cell-based bone formation in vivo. *Biomaterials* **2009,** *30* (27), 4639-4648.

152. Müller, R. H.; Rühl, D.; Runge, S.; Schulze-Forster, K.; Mehnert, W., Cytotoxicity of solid lipid nanoparticles as a function of the lipid matrix and the surfactant. *Pharm. Res.* **1997,** *14* (4), 458-462.

153. Goh, F.; Gross, J. D.; Simpson, N. E.; Sambanis, A., Limited beneficial effects of perfluorocarbon emulsions on encapsulated cells in culture: experimental and modeling studies. *J. Biotechnol.* **2010,** *150* (2), 232-239.

154. Hon, W.-C.; Wilson, M. I.; Harlos, K.; Claridge, T. D.; Schofield, C. J.; Pugh, C. W.; Maxwell, P. H.; Ratcliffe, P. J.; Stuart, D. I.; Jones, E. Y., Structural basis for the recognition of hydroxyproline in HIF-1α by pVHL. *Nature* **2002,** *417* (6892), 975-978.

155. Anderson, T. M. R.; Peacock, D. L.; Daniel, A. R.; Hubbard, G. K.; Lofgren, K. A.; Girard, B. J.; Schörg, A.; Hoogewijs, D.; Wenger, R. H.; Seagroves, T. N., Breast tumor kinase (Brk/PTK6) is a mediator of hypoxia-associated breast cancer progression. *Cancer research* **2013,** *73* (18), 5810-5820.

156. Hill, E.; Boontheekul, T.; Mooney, D. J., Regulating activation of transplanted cells controls tissue regeneration. *Proceedings of the National Academy of Sciences of the United States of America* **2006,** *103* (8), 2494-2499.

157. Fabiilli, M. L.; Wilson, C. G.; Padilla, F.; Martín-Saavedra, F. M.; Fowlkes, J. B.; Franceschi, R. T., Acoustic droplet–hydrogel composites for spatial and temporal control of growth factor delivery and scaffold stiffness. *Acta biomaterialia* **2013,** *9* (7), 7399-7409.

158. Moncion, A.; Lin, M.; O'Neill, E. G.; Franceschi, R. T.; Kripfgans, O. D.; Putnam, A. J.; Fabiilli, M. L., Controlled release of basic fibroblast growth factor for angiogenesis using acoustically-responsive scaffolds. *Biomaterials* **2017**.

159. Yun, M. S.; Lee, W. I., Analysis of bubble nucleation and growth in the pultrusion process of phenolic foam composites. *Compos. Sci. Technol.* **2008,** *68* (1), 202-208.

160. Chan, G.; Mooney, D. J., New materials for tissue engineering: towards greater control over the biological response. *Trends Biotechnol.* **2008,** *26* (7), 382-392.

161. Moncion, A.; Arlotta, K. J.; O'Neill, E. G.; Lin, M.; Mohr, L. A.; Franceschi, R. T.; Kripfgans, O. D.; Putnam, A. J.; Fabiilli, M. L., In vitro and in vivo assessment of controlled release and degradation of acoustically responsive scaffolds. *Acta Biomaterialia* **2016**.

162. Huang, X.; Jain, P. K.; El-Sayed, I. H.; El-Sayed, M. A., Plasmonic photothermal therapy (PPTT) using gold nanoparticles. *Lasers in medical science* **2008,** *23* (3), 217-228.

163. Zha, Z.; Wang, S.; Zhang, S.; Qu, E.; Ke, H.; Wang, J.; Dai, Z., Targeted delivery of CuS nanoparticles through ultrasound image-guided microbubble destruction for efficient photothermal therapy. *Nanoscale* **2013,** *5* (8), 3216-3219.

164. Coates, A. S.; Winer, E. P.; Goldhirsch, A.; Gelber, R. D.; Gnant, M.; Piccart-Gebhart, M.; Thürlimann, B.; Senn, H.-J.; Members, P.; André, F., Tailoring therapies—improving the management of early breast cancer: St Gallen International Expert Consensus on the Primary Therapy of Early Breast Cancer 2015. *Annals of oncology* **2015,** *26* (8), 1533-1546.

165. Vanneman, M.; Dranoff, G., Combining immunotherapy and targeted therapies in cancer treatment. *Nature reviews cancer* **2012,** *12* (4), 237-251.

166. Ott, P. A.; Hodi, F. S.; Kaufman, H. L.; Wigginton, J. M.; Wolchok, J. D., Combination immunotherapy: a road map. *Journal for immunotherapy of cancer* **2017,** *5* (1), 16.

167. Nakai, K.; Hung, M.-C.; Yamaguchi, H., A perspective on anti-EGFR therapies targeting triple-negative breast cancer. *American journal of cancer research* **2016,** *6* (8), 1609.

168. Tung, Y.-S.; Vlachos, F.; Choi, J. J.; Deffieux, T.; Selert, K.; Konofagou, E. E., In vivo transcranial cavitation threshold detection during ultrasound-induced blood–brain barrier opening in mice. *Physics in medicine and biology* **2010,** *55* (20), 6141.

169. FDA List of Cleared or Approved Companion Diagnostic Devices (In Vitro and Imaging Tools). (accessed 01/16/2018).

170. Opacic, T.; Paefgen, V.; Lammers, T.; Kiessling, F., Status and trends in the development of clinical diagnostic agents. *Wiley Interdiscip. Rev.: Nanomed. Nanobiotechnol.* **2017,** *9* (4).

171. Chollet, P.; Amat, S.; Cure, H.; De Latour, M.; Le Bouedec, G.; Mouret-Reynier, M.; Ferriere, J.; Achard, J.; Dauplat, J.; Penault-Llorca, F., Prognostic significance of a complete pathological response after induction chemotherapy in operable breast cancer. *British journal of cancer* **2002,** *86* (7), 1041-1046.

172. Willyard, C., Cancer therapy: an evolved approach. *Nature* **2016**, 166-168.

173. Seekell, R. P.; Lock, A. T.; Peng, Y.; Cole, A. R.; Perry, D. A.; Kheir, J. N.; Polizzotti, B. D., Oxygen delivery using engineered microparticles. *Proceedings of the National Academy of Sciences* **2016**, 201608438.

174. Liu, L.; Chakma, A.; Feng, X., Gas permeation through water-swollen hydrogel membranes. *Journal of Membrane Science* **2008,** *310* (1), 66-75.

175. Chen, L.; Tredget, E. E.; Wu, P. Y.; Wu, Y., Paracrine factors of mesenchymal stem cells recruit macrophages and endothelial lineage cells and enhance wound healing. *PloS one* **2008,** *3* (4), e1886.

176. Guilak, F.; Cohen, D. M.; Estes, B. T.; Gimble, J. M.; Liedtke, W.; Chen, C. S., Control of stem cell fate by physical interactions with the extracellular matrix. *Cell stem cell* **2009,** *5* (1), 17-26.

177. Hockel, M.; Vaupel, P., Tumor hypoxia: definitions and current clinical, biologic, and molecular aspects. *Journal of the National Cancer Institute* **2001,** *93* (4), 266-276.

# VITA

Daniela Yvonne Santiesteban was born in July of 1990 in Princeton, New Jersey to Patricia and José Santiesteban. She grew up in several cities within eastern Pennsylvania and in Baton Rouge, Louisiana. Throughout her childhood she was very active, participating in several sports but ultimately fell in love with the game of tennis, which she played competitively. Daniela attended the University of Virginia in Charlottesville, where she received her B.S. in Biomedical Engineering. Daniela went on to earn her M.S. in Biomedical Engineering from the University of Texas at Austin. She conducted some of her PhD work at the University of Texas at Austin but ultimately transferred to the Georgia Institute of Technology, where she received her PhD in Biomedical Engineering. Daniela has presented her work at several national and international conferences, and published her research in *Nano Letters* and *Annals of Biomedical Engineering*. In 2015 Daniela received the Whitaker International Fellowship and studied at the Universitat de Duisburg-Essen. During her time as a PhD student Daniela was involved in several outreach organization and entrepreneurial endeavors. Following graduation, Daniela plans to continue in the life sciences space focused on commercializing biotechnologies.